Intercalibration of Spectral Vegetation Indices Based on Soil Isolines for Satellite Constellation Systems

by

Kenta Taniguchi

A dissertation submitted in partial fulfillment
of the requirements for the degree of
Doctor of Philosophy
(Information Science and Technology)
in Aichi Prefectural University
2016

Doctoral Committee:

Professor Hiroki Yoshioka, Chair
Professor Kazuhito Murakami
Professor Naohiro Toda

ACKNOWLEDGEMENTS

The author would like to express my sincere gratitude to my advisor Dr. Hiroki Yoshioka for guiding my work and preparing many opportunities through which my skills in learning, teaching and leading as well as researching are enhanced comprehensively. Appreciation on his efforts for my experiences and skill developments is absolutely beyond description. Special thanks are due to two co-chairmans, Dr. Kazuhito Murakami and Dr. Naohiro Toda for their enthusiastic efforts for reviewing my research. The author would like to thank Dr. Masayuki Matsuoka and Dr. Kenta Obata who contributed since beginning of this research. Finally, the author is deeply grateful to my family for their support and encouragement.

TABLE OF CONTENTS

LIST OF FIGURES

Figure

LIST OF TABLES

Table

ABSTRACT

The intercalibration of measurements collected from various sensors deployed onboard the satellites of constellation systems is crucial for ensuring reliability and consistency among the collected big data sets. One of the factors that introduces relative errors between the measurements collected from any pair of sensors is the sensor-specific spectral response function (SRF). Differences between the SRFs of distinct sensors introduce inconsistencies between two measurements, known as the wavelength effect. This study focused on the wavelength effect in the spectral vegetation indices (VIs) used in a wide range of interdisciplinary studies. The relationship between the VIs obtained from two different SRFs was derived using an analytical approach based on an expression for the relationship between red and near-infrared reflectances, called soil isolines. Soil isolines often contain a singular point on a dark soil background. A derivation technique was introduced to circumvent difficulties associated with singularities. The resultant soil isolines were represented by power series of a common parameter. The derived soil isoline was extended by employing a two-band linear mixture model, in which the fraction of vegetation cover was explicitly considered as a biophysical parameter. The differences between the soil isolines of the fully covered and partially covered cases were explored analytically. A set of numerical experiments was conducted using coupled leaf and canopy radiative transfer models. The numerical results revealed that the accuracy of the soil isoline increased with the truncation order, thereby confirming the validity of the derived expressions. Finally, this study introduced a technique for deriving the relationship between the VIs obtained from two sensors using soil isoline equations to describe the full canopy case. The derivation proceeded using a parametric form of the soil isoline equations. The derivation steps were explained conceptually, then the conceptual steps were cast in a practical derivation by assuming a general form of the two-band VI. Finally, the derived expressions were demonstrated numerically using a coupled leaf and canopy radiative transfer model. The derived expressions and numerical results suggested that the relationship between the VIs measured at different wavelengths varied with the soil reflectance spectrum beneath the vegetation canopy. These results indicated that caution is required when retrieving inter-sensor VI relationships over regions consisting of soil surfaces having distinct spectra.

CHAPTER I

Introduction

1.1 Satellite Constellation System

Developing solutions to global terrestrial environmental problems requires integrated knowledge gleaned from interdisciplinary fields as well as international cooperation. The fifth synthesis report of the Intergovernmental Panel on Climate Change (IPCC) stated that climate change is one of the most pressing challenges of our time[1]. This global problem can only be addressed through international cooperation on mitigation and adaptation[2]. Atmospheric greenhouse gas concentrations, which have steadily increased since the industrial revolution, are directly related to anthropogenic emissions and a decrease in the forested areas throughout the world. A reduction in anthropogenic CO_2 emissions should effectively mitigate climate change. The Paris agreement on reducing CO_2 emissions and Reducing Emissions from Deforestation and forest Degradation in developping countries (REDD)[3] for the preservation of the environment constitute significant steps toward international cooperation. In addition to the actions needed to mitigate climate change, the adaptation to risks arising from climate-related impacts plays an important role in ensuring safety in our future[1]. One of the most effective approaches to monitoring the Earth's environment involves satellite remote sensing activities. Landsat series at a medium spatial resolution have provided a long-term data record of the Earth over the past 40 years at a temporal resolution of 16 days[4, 5]. One approach to enhancing the frequency of the revisit cycle involves using spectral imaging radiometers with a low spatial resolution[6–8]. NASA's moderate resolution imaging spectroradiometer (MODIS) onboard the Terra and Aqua satellites exemplifies the data collected at a lower resolution than the Lansat series, which has a spatial resolution of 250 m. The MODIS data provide a daily data product[9].

There is a trade-off between the timing of a revisit cycle and the spatial resolution

of satellite remote sensing images, which is a problem that must be addressed in the field of environmental monitoring. Although frequent observations over the long term are needed to enact adaptive remedies on the global scale, earth observations collected using a single satellite do not meet the technical requirements for such observations. In fact, the data density with respect to the time series is important for data analysis and improving our understanding of the dynamic earth environment. Efforts directed toward visualizing the geophysical parameters of earth support advances in remote sensing technologies[10–12]. Formation-based multiple satellite remote sensing systems (satellite constellation systems)[13, 14] enhance the frequency and accuracy of observations and overcome problems associated with indistinct single satellite remote sensing images. Low-cost small satellite platforms that ease costs play an important role in generating constellation systems that dramatically increase observation opportunities[15].

Although constellation systems increase the observation frequency and are advantageous for data analysis, further problems related to data consistency exist: the data product depends on the sensor specifications. A variety of data product types from different instruments are available and yield a range of relative errors when compared. Intercalibration is a method for rectifying inconsistencies in the data products caused by various factors[16]. This study focused on wavelength effects in data products, as described in the following sections.

1.2 Spectral Vegetation Index (VI)

Optical remote sensing applications that use solar radiation can estimate the geographical distributions of several types of features on the Earth's surface[17]. The reflectance spectrum ρ_λ at a particular wavelength λ may be estimated as arising from a target feature[18, 19] expressed as

$$\rho_\lambda = \frac{\pi L_\lambda d^2}{L_{\mathrm{in},\lambda} \cos(\theta_s)}, \tag{1.1}$$

where L_λ and $L_{\mathrm{in},\lambda}$ are the detected radiance and mean exoatmospheric solar irradiance, d and θ_s are Earth-Sun distance in astronomical units and the solar zenith angle, respectively.

Spectral indices (SI)[20, 21] derived from two or more reflectance spectra are useful for analyzing remotely-sensed data because their use is simpler than solving the inversion problem of the radiative transfer model[22–24]. For example, spectral vegetation indices (VIs) are derived using knowledge curated in interdisciplinary environmen-

tal study fields[25–35]. In general, two-band VIs are designed as a function of two reflectances in the visible red and near-infrared (NIR) regions,

$$v = f(\rho_{\mathrm{red}}, \rho_{\mathrm{NIR}}), \tag{1.2}$$

where v, ρ_{red}, and ρ_{NIR} are the VIs, reflectances in the red, and reflectances at NIR wavelengths, respectively.

"Vegetation Indices (VI) are optical measures of the vegetation canopy ' greenness ', a direct measure of the photosynthetic potential resulting from the composite property of the total leaf chlorophyll, leaf area, canopy cover, and structure."[36]. Thus, VIs represent a composite function of various vegetation parameters, including the leaf area index (LAI)[37], fraction of vegetation coverage (FVC)[38], and fraction of absorbed photosynthetically active radiation (FAPAR)[39], in addition to parameters unrelated to vegetation, such as the soil background[29, 40] and atmosphere[41, 42], with which photons from the Sun interact prior to reaching a detector. Because VIs are affected by the soil and atmosphere, researchers have investigated these effects in detail[43–45] and have developed algorithms for applying the VI data products[46].

1.3 Wavelength Effect

The spectral response function (SRF), a specification parameter for each sensor, must be managed during integration of the VIs[47]. Target reflectance spectra ρ_λ are convoluted with the SRF,

$$\rho_\Lambda = \frac{\int \rho_\lambda L_{\mathrm{in},\lambda} \Lambda_\lambda d\lambda}{\int L_{\mathrm{in},\lambda} \Lambda_\lambda d\lambda}, \tag{1.3}$$

where ρ_Λ is the estimated reflectance spectrum obtained from a target reflectance spectrum ρ_λ when detected by a sensor with an SRF of Λ_λ. Figure 1.1 shows four types of SRFs characteristic of red and NIR bands. As shown in the figure, the SRFs of the red and NIR sensors were distinct. In real cases, sensor degradation in space post-launch[48] introduces further spectral effects.

The differences between two SRFs, Λ^a_λ and Λ^b_λ from sensors-a and -b, may cause those between the obtained reflectances ρ_{Λ^a} and ρ_{Λ^b} as follows. If $\Lambda^a_\lambda \neq \Lambda^b_\lambda$, then $\rho_{\Lambda^a} \neq \rho_{\Lambda^b}$. The inconsistencies obtained from a single data product are called the "wavelength effect"[49]. The wavelength effect in the reflectances is propagated in

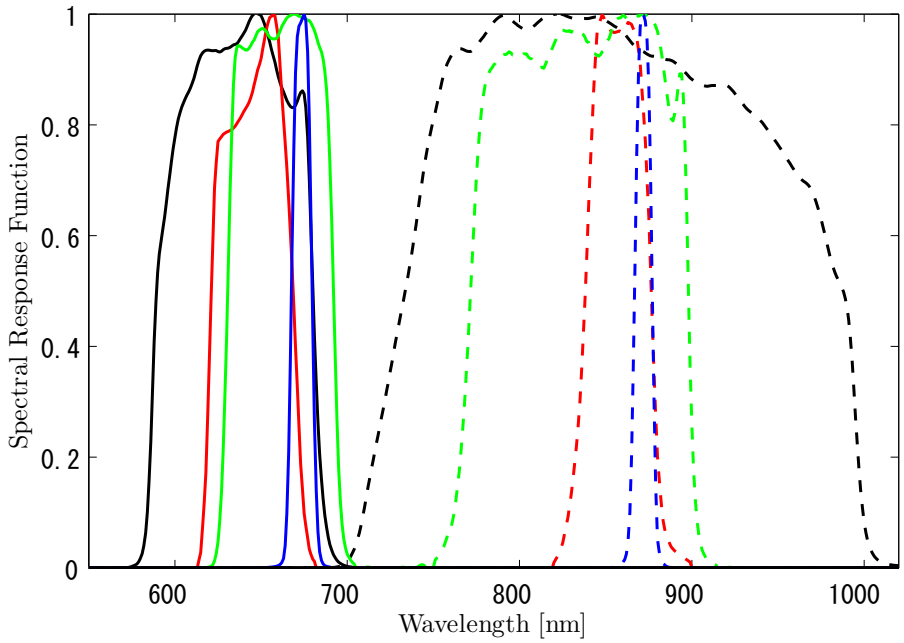

Figure 1.1: Four sensor spectral response functions (SRFs) associated with red and near-infrared (NIR) bands: Blue, black, red, and green lines correspond to the GOSAT-CAI, NOAA-AVHRR/3, TERRA-MODIS, and LANDSAT7-ETM+ SRFs, respectively. The solid line represents the red SRF, and the dashed line represent the NIR SRF.

the VIs due to the high intensities of the reflectance data products [50].

$$v_a \neq v_b \tag{1.4}$$

Here, v_a and v_b correspond to the VIs obtained from the SRFs of different sensors, $-a$ and $-b$, respectively. The relative error between the two VIs obtained from different SRFs could be reduced by applying intercalibration methods.

1.4 Intercalibration of Spectral Vegetation Indices

The primary purpose of an inter-calibration process is to minimize biases caused by differences in the sensor specifications, such as, but not limited to, the spectral response functions (wavelength effect)[47, 51–53], the spatial resolution[38, 54–56], the illumination geometry[57, 58], differences among the absolute calibrations of the systems[59], the algorithms used for parameter retrievals, and the atmospheric correction schemes[60]. Significant efforts have been devoted to understanding the mech-

anisms underlying such complex effects[61, 62].

The inter-calibration of radiances and/or reflectance spectra obtained from two similar instruments has been conducted[49, 50, 63], and several techniques have been proposed to minimize certain bias variations among the sensors[49, 51, 52]. The differences among reflectance spectra obtained from different sensors have been examined using images acquired nearly simultaneously[64–66]. The outputs from one sensor have been plotted against the corresponding outputs from other sensors to characterize the biases, to some extent[67, 68]. These studies often reach similar conclusions, for example, that the relationship (or, rigorously, the coefficients that describe the relationship) between two VIs varies from site to site[50, 66, 69]. Few theoretical explanations of this land cover dependence have been provided to explain the empirical evidence. This study attempts to address the need for an explanation.

The inter-calibration studies in the land characterization discipline have often selected the VI as an example of the satellite data products[70–75]. Because the VI has been used as a proxy measure for certain biophysical parameters, the impacts of systematic errors due to differences in the band configurations may be propagated into downstream models. Certain widely used indices, such as the Normalized Difference Vegetation Index (NDVI)[76], can contribute to such model biases[77–80]. Thus, a close examination of VI measures presents a meaningful step toward algorithmically reducing biases in data.

A satellite constellation system constructed from a collection of sensors must be analyzed to understand its system-specific wavelength effect. For example, the wavelength effect in a set of 20 small satellites in a constellation system is characterized by the intercalibration coefficients associated with the ${}_{20}C_2 = 190$ satellite pairs. Unchecked, the wavelength effect can undermine calculations based on the data product of these valuable constellation systems. This research focused on the independent wavelength effect by deriving the relationships among the VI values of different sensors.

Our discussion is limited to investigations of the relationships among the VI values of different sensors. One difficulty encountered in this investigation involved the selection (and often identification) of a model that could provide a set of reflectance spectra under any desirable conditions. In any investigation based on numerical models, this selection depends simply on the parameter range covered by the model. The availability of convenient analytical models is limited; therefore, we sought to explore the analytical relationships, expressed as isoline equations, between reflectances collected at two different wavelengths[29, 81–83].

An isoline equation can be defined as the relationship between the reflectances

measured at two wavelengths under certain conditions,

$$\rho_{\lambda 1} = f_{\text{iso}}(V, \rho_{\lambda 2}), \tag{1.5}$$

where $\rho_{\lambda 1}$ and $\rho_{\lambda 2}$ are the reflectances measured at different wavelengths, for example, the red and NIR reflectances, and f_{iso} is a function of $\rho_{\lambda 2}$ for some choice of parameter V. The inverse problem of the isoline equation may be related to the SI,

$$V = f_{\text{iso}}^{-1}(\rho_{\lambda 1}, \rho_{\lambda 2}). \tag{1.6}$$

Isolines encompass the wavelength effects in the reflectance spectral subspace detected by each sensor. Recalling that the wavelength effect of a VI results from the measured reflectances, an analytical expression for an isoline should link the structure of the wavelength effect in the VI. In fact, vegetation isolines introduce several advantages into investigations of the VI relationships, as discussed elsewhere[84, 85].

This paper focuses on soil isolines in the red and NIR reflectance subspace[86, 87]. Soil isolines are orthogonal to the vegetation isolines because the soil isoline is defined as a set of reflectance spectra attributed to a certain soil reflectance spectrum. The reflectance spectra on a given isoline result from a constant soil reflectance spectrum characterized by a unique set of soil optical properties. Note that the concept of a soil isoline differs from that of a vegetation isoline. Vegetation isoline equations are models developed mainly based on parameters related to vegetation, whereas soil isoline equations are modeled from soil variable inputs. The derivation of soil isoline equations permits a mathematical analysis of the data products, such as the VIs.

1.5 Objectives

The objective of this study was to derive the inter-sensor VI relationships using an analytical form of the soil isolines. Two subgoals were identified in this work: (1) the derivation of soil isoline equations, and (2) the derivation of inter-VI relationships based on the derived soil isoline equations.

I began by deriving the soil isoline equations in the red-NIR subspace by introducing an affine transformation and polynomial fit of the reflectance subspace. In Chapter 2, an algorithm describing the soil isoline is derived under a homogeneous fully-vegetated target pixel. Note that full canopy coverage conditions must be relaxed because satellite data include pixels constructed from a variety of land cover types, producing a mixel. I next introduced an extension of the spatial regularization by fusing the linear mixture model discussed in Chapter 3. The derived soil isoline

equations were extended to yield a representation applicable to mixel data in satellite images. Numerical experiments were conducted to validate the derived results.

Chapter 4 proposes a deductive derivation method for applying the derived soil isoline equations to VIs. The derived expression could be described using a polynomial form by truncating the equation and inter-VI relationship as an approximation. Numerical experiments were conducted to validate and analyze the derived inter-VI relationship. The uncertainties propagated by the sensor-specific signal-to-noise ratio (SNR) were compared to derive the translation error associated with the proposed inter-VI relationship. Finally in Chapter 5, conclusions drawn from the wavelength effect present in the VIs derived from the soil isoline-based intercalibration methods are summarized.

CHAPTER II

Theoretical Background for the Soil Isoline Equations in the Red–Near-infrared Reflectance Subspace

2.1 Introduction

Parameter retrieval algorithms based on remotely sensed land surface reflectance data often involve band algebraic manipulations and produce environmental data records such as vegetation biophysical parameters or soil optical properties. Some algorithms use an intermediate proximity measure, e.g., the spectral vegetation index (VI), either explicitly or implicitly[29, 88, 89]. The performances of the data records depend somewhat on the functional forms of VIs; hence, research in this field has extensively explored the development and improvement of functional forms over the last few decades[20, 29, 76, 81, 88, 90]. Numerous VI models have been developed through these efforts[25–35].

VI models may be categorized systematically according to the concept of the 'isoline' used to develop and analyze the VI[76, 81, 82, 84, 90–95]. By limiting our discussion to VI models of the red and NIR reflectance space, two main types of isoline have been recognized: the vegetation 'index' isoline (VI isoline) and the vegetation 'biophysical' isoline (the latter is denoted the 'vegetation isoline' in this study)[29, 81, 82, 84, 94, 95]. The VI isoline represents a set of red and NIR reflectance spectra that produce a single VI value, meaning that the VI isoline depends only on the VI model equation. This point is illustrated in Fig. 2.1(a) using the normalized difference VI (NDVI) as an example. The vegetation isoline (Fig. 2.1(b)), on the other hand, describes a group of reflectance spectra that belong to a fixed set of biophysical parameters and structural properties, such as the leaf area index (LAI), fraction of vegetation cover (FVC), and leaf angle distribution. The vegetation isoline can be

simulated numerically using a radiative transfer model of the vegetation canopy[96–99]. Note that these two isolines (VI isoline and vegetation isoline) have no physical relationship, meaning that the two are obtained mutually independently. Also note that the ultimate goal of the VI development effort may be understood as an effort to identify a VI model equation that yields VI isolines that agree perfectly with the vegetation isolines[29, 81, 82, 84, 94, 95]. Several studies suggest that the discrepancies between the VI isoline and the vegetation isoline indicate performance losses in the VI model as a result of internal and external sources of errors, including the influence of soil brightness changes beneath the vegetation canopy[31, 33, 40, 91, 100, 101].

Formulations of the vegetation isoline have been developed in several previous studies[29, 82, 84, 94] and have been used to develop VI models and analyze VI errors[25–35]. The isoline equations have been used directly to retrieve the LAI[102] and FVC[83] from a remote sensing data set. In recent years, the isoline equation, which describes the relationship between the red and NIR reflectances, has been used to cross-calibrate the VI products obtained from multiple sensors[47, 74, 84, 85, 103]. These activities clearly indicate that the concept of the isoline has provided rich information and useful tools for a variety of investigations while significantly advancing research in this field.

Isolines are not limited to descriptions of biophysical properties. An alternative to the vegetation isoline is the soil isoline, which represents a group of reflectance spectra produced from a constant soil surface. Note that a soil isoline is totally different from the concept of the 'soil line'[93], which is a zero vegetation isoline. In other words, the soil line is a vegetation isoline describing the particular case of zero vegetation, whereas the soil isoline is a set of spectra obtained under a constant set of soil reflectance spectra, in view of various biophysical parameters. This point is illustrated in Fig. 2.1(c).

Extensive efforts have been devoted toward studies of vegetation isolines; however, soil isolines have not been fully investigated. The present study aims to contribute to this area of research. Singularities at relatively dark soil surfaces present a significant barrier to modeling soil isolines using a simple polynomial form [104]. By limiting our discussion to the red-NIR reflectance space under low soil reflectances, the soil isoline may be approximated as parallel to the NIR axis. As a result, some of the polynomial coefficients are extremely large. Such singularities must be circumvented in any soil isoline model. A numerical example of this situation is discussed in the next section.

The concept of the soil isoline is not new. Soil isolines have been introduced and routinely used as a conceptual tool on various occasions to explain band manipulation

algorithms and their performances in the presence of external sources of errors[29, 81, 86, 87, 105–110]. These concepts have not been fully investigated, however, nor have they been developed analytically to date. Formal derivations of soil isoline estimation algorithms and the accuracy of such approaches when applied to truncated higher-order terms must be explored in anticipation of soil isoline applications. This study attempts to address these needs.

Three objectives have guided this study. First, a formal derivation of soil isoline equations with an arbitrary level of accuracy is introduced. Second, a technique for approximating the analytical representation is described. This approximation is more amenable to applications than the analytical expression. Finally, the validity of the derived relationship is explored from a fundamental physics point of view.

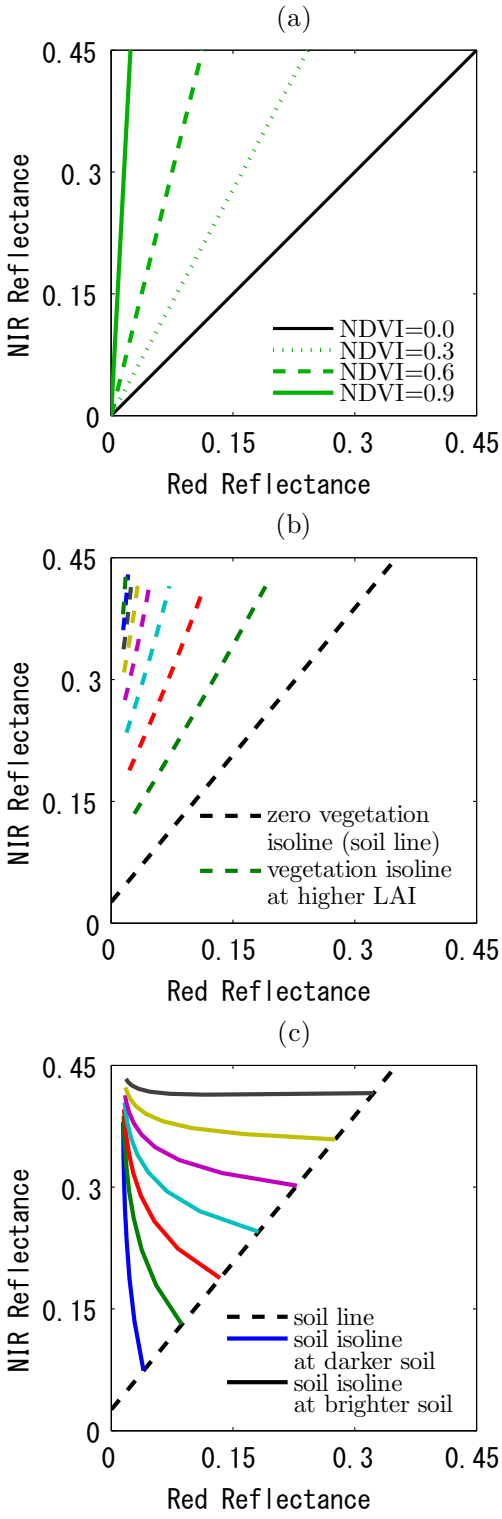

Figure 2.1: Illustration of the VI isolines (a), vegetation biophysical isolines (b), and soil isolines (c). The concept of the soil line is illustrated in (b), and (c) illustrates a zero vegetation isoline.

2.2 Difficulties Associated With Modeling Soil Isolines Using Polynomial Fitting Approaches

The difficulties associated with modeling soil isolines were briefly mentioned above. An illustrative numerical example of a soil isoline modeled using a second-order polynomial is described here. In this model, the soil isoline is expressed in terms of the relationship between the red (ρ_r) and NIR (ρ_n) reflectances according to

$$\rho_n \approx k_0(R_s) + k_1(R_s)\rho_r + k_2(R_s)\rho_r^2, \tag{2.1}$$

where k_0, k_1, and k_2 represent the polynomial coefficients.

A reflectance spectrum (ρ_r, ρ_n) may be numerically simulated using the radiative transfer model PROSAIL[99]. During the simulation, only two parameters are varied: LAI and the soil reflectance of the red band R_s. Because a soil line was assumed here, the soil reflectance of the NIR band was uniquely determined based on the soil line equation from the red reflectance R_s. For this reason, the NIR reflectance of the soil surface was not explicitly introduced in this study. An isoline was numerically simulated by setting the soil reflectance R_s to a fixed value, meaning that the LAI was the only variable parameter used to optimize each soil isoline in this example. After simulating each soil isoline (under a constant value of R_s), a set of three coefficients (k_0, k_1, and k_2) was obtained through polynomial fitting approaches. These steps were repeated for various values of R_s to obtain the coefficients k_i as a function of R_s. Figure 2.2 shows a plot of the coefficients k_i as a function of R_s. As shown in the figure, the coefficient k_2 assumed extremely high values at low values of R_s, which prevented the development of accurate polynomial models. These difficulties arose from the fact that some soil isolines in dark soils were almost parallel to the NIR axis. The reflectance axis may be rotated through an angle to circumvent these difficulties. The next section provides a stepwise derivation of a soil isoline equation designed to avoid these difficulties.

2.3 Parametric Representation of the Soil Isoline Equation

2.3.1 Assumptions and Transformation

The derivation begins with the assumption of a linear soil line, represented by

$$R_{sn} = s_1 R_{sr} + s_0, \tag{2.2}$$

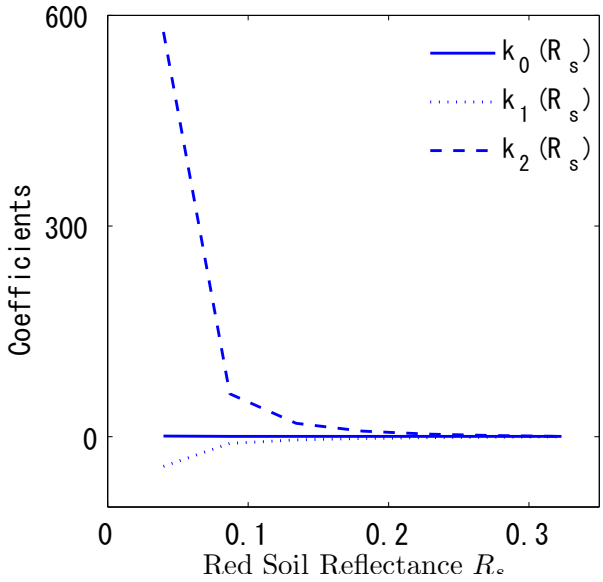

Figure 2.2: Variations of the polynomial coefficients k_0, k_1, and k_2 used to approximate soil isolines in the red and NIR reflectance space. Each soil isoline was simulated for a fixed soil reflectance R_s. The coefficients were then obtained numerically from a polynomial fit of the simulated soil isolines. The coefficients as a function of R_s are plotted in the figure. Note that the coefficients k_2 approached extremely high values, indicating the presence of a singularity at low values of R_s.

where s_1 and s_0 are the slope and offset, respectively.

In the derivation of the soil isoline equation, the original reflectance subspace was shifted and rotated through a certain angle to avoid the singularity shown in Fig. 2.2. The original coordinate was shifted to set the intersection between the Y-axis and the soil line to be the origin of the transformed subspace. The rotation angle was identical to the slope of the soil line (θ in radians). The transformation could be expressed as

$$\boldsymbol{\rho}' = T(-\theta)(\boldsymbol{\rho} - \boldsymbol{\mu}), \tag{2.3}$$

where T represents a rotation matrix, and $\boldsymbol{\rho}$ and $\boldsymbol{\rho}'$ are the reflectance spectra before and after the transformation, respectively, in the red and NIR reflectance space

$$\boldsymbol{\rho} = (\rho_r, \rho_n)^t, \tag{2.4}$$

$$\boldsymbol{\rho}' = (\rho'_r, \rho'_n)^t. \tag{2.5}$$

The vector $\boldsymbol{\mu}$ shifted the X-axis by an amount equal to the soil line offset,

$$\boldsymbol{\mu} = (0, s_0)^t. \tag{2.6}$$

Because the axis was rotated through an angle between the soil line and the X-axis, θ was defined by the soil line slope s_1 as

$$\theta \;=\; \arctan(s_1)\ (-\pi/2 < \theta < \pi/2). \tag{2.7}$$

Finally, the relationships between the reflectances before and after the transformation became

$$\rho'_r = \cos(\theta)\rho_r + \sin(\theta)(\rho_n - s_0), \tag{2.8a}$$
$$\rho'_n = -\sin(\theta)\rho_r + \cos(\theta)(\rho_n - s_0). \tag{2.8b}$$

The NIR reflectance in the transformed reflectance space, Eq. (2.8b), played an important role in this study. The NIR reflectance assumed a form similar to that of a vegetation index known as the weighted difference vegetation index (WDVI)[28]. This result could be understood by rearranging Eq. (2.8b) to give

$$\rho'_n = \cos(\theta)(\rho_n - s_1\rho_r - s_0). \tag{2.9}$$

This model and the WDVI model are distinguished by the factor $\cos(\theta)$ and the offset $-s_0$. Because both the factor and the offset are constant values, the functional behavior of ρ'_n is essentially identical to that of the WDVI (V), which is defined as

$$V = \rho_n - s_1\rho_r. \tag{2.10}$$

This study used ρ'_n as a common parameter during the derivation of the soil isoline equation. The common parameter yielded behavior indistinguishable from that of the WDVI, and the soil isoline equation was expected to be strongly correlated with biophysical parameters, such as the LAI. The validity of the choice of this parameter may be understood intuitively by recalling that a major source of variation in the soil isoline is the biophysical parameters. (A soil isoline is obtained under conditions of a fixed soil profile.)

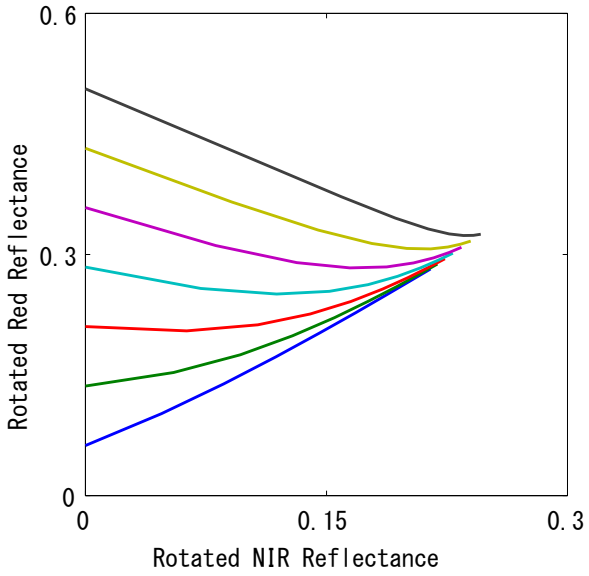

Figure 2.3: Illustration of the soil isolines obtained after applying a space transformation to fit the original red axis to the soil line. The x- and y-axes were identified with ρ'_n and ρ'_r, respectively.

2.3.2 Polynomial Model in the New Reflectance Space

The next step of the derivation involved modeling the relationship between ρ'_r and ρ'_n. A simple polynomial representation was used for this purpose. ρ'_r was modeled using a power series of ρ'_n,

$$\rho'_r = \sum_{i=0}^{m_p} p_i(R_s)\rho'^i_n + O(\rho'^{\,m_p+1}_n), \tag{2.11}$$

where m_p and p_i represent the order of the polynomial and the coefficients of the i-th order term. R_s indicates the soil reflectance. This relationship could be approximated to an arbitrary order of accuracy by selecting a polynomial based on an orthogonal set of functions, such as the Chebyshev polynomials. Therefore, this part of the modeling process did not reduce the accuracy of the model. The first term on the right-hand side of Eq. (2.11) is defined as the function $f_{m_p}(R_s, \rho'_n)$ and will be discussed further later in this study,

$$f_{m_p}(R_s, \rho'_n) = \sum_{i=0}^{m_p} p_i(R_s)\rho'^i_n. \tag{2.12}$$

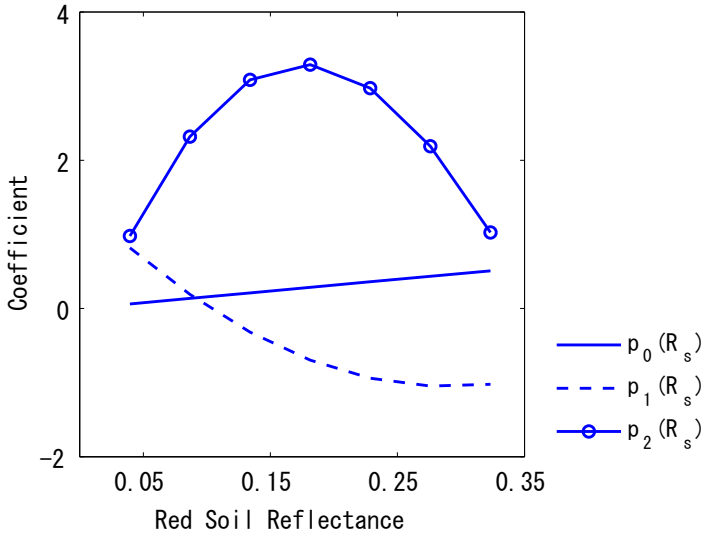

Figure 2.4: Illustration of the coefficients p_0, p_1, and p_2, used to approximate the soil isolines using second-order polynomials as a function of the soil reflectance R_s. The solid lines with circles, the dotted lines, and the solid lines indicate the coefficients p_0, p_1, and p_2, respectively.

I was interested in examining the variations in p_i as a function of the soil reflectance R_s. The parameter p_i varied smoothly over a small range of values, unlike the polynomial fit results obtained from the original reflectance space, as described in Fig. 2.2. The coefficients p_i were obtained numerically by assuming a second order polynomial,

$$\rho'_r \approx p_0(R_s) + p_1(R_s)\rho'_n + p_2(R_s)\rho'^2_n. \tag{2.13}$$

Figure 2.4 plots the the polynomial coefficients p_i. The figure indicates that the coefficients did not feature singularities, such those described in Fig. 2.2. Unlike the fitting results obtained on the original space (Fig. 2.2), all coefficients varied smoothly as a function of R_s and remained relatively stable with a small variance (Fig. 2.4).

2.3.3 Parametric Representation of the Soil Isoline

Equation (2.11) represents a soil isoline in the transformed reflectance space. A parametric representation of the soil isoline in the original reflectance space was ob-

tained simply by inverting the transformation

$$\boldsymbol{\rho} = T(\theta)\boldsymbol{\rho}' + \boldsymbol{\mu}. \tag{2.14}$$

Prior to solving this relationship, ρ'_r was replaced with the derived soil isoline equation

$$\boldsymbol{\rho}' = \left(f_{m_p}(R_s, \rho'_n) + O({\rho'_n}^{m_p+1}), \rho'_n\right)^t, \tag{2.15}$$

where $f_{m_p}(R_s, \rho'_n)$ corresponds to a soil isoline function in a rotated reflectance space, described by a polynomial of order m_p.

Equations (2.14) and (2.15) describe a system of soil isoline equations derived using the common parameter ρ'_n,

$$\rho_r = \cos(\theta) f_{m_p}(R_s, \rho'_n) - \sin(\theta)\rho'_n + \cos(\theta) O({\rho'_n}^{m_p+1}), \tag{2.16a}$$
$$\rho_n = \sin(\theta) f_{m_p}(R_s, \rho'_n) + \cos(\theta)\rho'_n + s_0 + \sin(\theta) O({\rho'_n}^{m_p+1}). \tag{2.16b}$$

Substituting Eq. (2.12) into the above equations yields the following form:

$$\rho_r = \sum_{i=0}^{m_p} a_i(R_s){\rho'_n}^i + \cos(\theta) O({\rho'_n}^{m_p+1}), \tag{2.17a}$$
$$\rho_n = \sum_{i=0}^{m_p} b_i(R_s){\rho'_n}^i + \sin(\theta) O({\rho'_n}^{m_p+1}), \tag{2.17b}$$

where $a_i(R_s)$ and $b_i(R_s)$ are the coefficients defined as follows, using the Kronecker Delta function δ,

$$a_i(R_s) = \cos(\theta) p_i(R_s) - \sin(\theta)\delta_{1i}, \tag{2.18a}$$
$$b_i(R_s) = \sin(\theta) p_i(R_s) + \cos(\theta)\delta_{1i} + s_0\delta_{0i}. \tag{2.18b}$$

2.3.4 Symbolic Form of the Soil Isoline Equation Without ρ'_n

The index-like parameter ρ'_n could be removed symbolically by solving one of the above equations for ρ'_n. I first defined two functions before proceeding with the

derivation:

$$g_r(\rho'_n) = \sum_{i=0}^{m_p} a_i(R_s)\rho'^i_n + \cos(\theta)O(\rho'^{\,m_p+1}_n), \tag{2.19a}$$

$$g_n(\rho'_n) = \sum_{i=0}^{m_p} b_i(R_s)\rho'^i_n + \sin(\theta)O(\rho'^{\,m_p+1}_n). \tag{2.19b}$$

Using these functions, a reflectance spectrum could be expressed as

$$\boldsymbol{\rho} = \left(g_r(\rho'_n), g_n(\rho'_n)\right)^t. \tag{2.20}$$

After solving Eq. (2.19a) for ρ'_n symbolically,

$$\rho'_n = g_r^{-1}(\rho_r), \tag{2.21}$$

the soil isoline equation without the parameter ρ'_n became

$$\rho_n = g_n(g_r^{-1}(\rho_r)), \tag{2.22}$$

or, reciprocally,

$$\rho_r = g_r(g_n^{-1}(\rho_n)). \tag{2.23}$$

Although I have described the derivation steps symbolically, the inversion process expressed in Eq. (2.19a) (or Eq. (2.19b)) is not practical when applied to higher-order terms. Practical applications of the representation require the truncation of certain higher-order terms in Eqs. (2.19a) and (2.19b). The consequences of the truncation order must be evaluated in view of the desired accuracy for an approximated soil isoline equation. The truncation orders in Eqs. (2.19a) and (2.19b) may be asymmetric; that is, the truncation order may be selected such that Eq. (2.19a) provides a first-order approximation whereas Eq. (2.19b) provides a third-order approximation. For the sake of practicality, this point will be discussed further in the following sections.

2.4 Approximations of the Soil Isoline Equation

This section introduces several soil isoline equations approximated using the higher-order truncated terms expressed in Eqs. (2.17a) and (2.17b). Although the polynomial orders in the red and NIR reflectances are indicated by a single integer m_p, they are not necessarily identical (the orders may be asymmetric). Because the value of

m_p may be independently selected in either band, m_r and m_n will be used to refer to the red and NIR reflectances, respectively. In the new notation, these equations became

$$\rho_r = \sum_{i=0}^{m_r} a_i(R_s)\rho_n'^i + \cos(\theta)O({\rho_n'}^{m_r+1}), \tag{2.24a}$$

$$\rho_n = \sum_{i=0}^{m_n} b_i(R_s)\rho_n'^i + \sin(\theta)O({\rho_n'}^{m_n+1}). \tag{2.24b}$$

The soil isoline equation could be approximated by selecting integers for m_r and m_n. Higher values of m_r and m_n increased the accuracy of the approximated soil isoline. The drawback to choosing highly accurate approximations was that solving these equations for ρ_n' was difficult. Such difficulties could prevent the development of a useful analytical formulation of the soil isoline. In the following subsections, I introduce several approximations and investigate the accuracy of the approximated soil isoline equations from a practical point of view. Each case is constructed using a combination of m_r and m_n.

2.4.1 Case-1 $(m_r, m_n) = (1, 1)$: First-order Approximation of the Soil Isoline Equation

The first case involves implementing a first-order approximation for both the red and NIR reflectances. Here, m_r and m_n were set to unity. In this case, Eqs. (3.31) and (3.32) were truncated at and beyond the second-order term.

$$\rho_r = a_0 + a_1\rho_n', \tag{2.25a}$$

$$\rho_n = b_0 + b_1\rho_n'. \tag{2.25b}$$

In the above equations, the coefficients a_i and b_i depended solely on the soil reflectance R_s (and were independent of the biophysical parameters). I explicitly avoided using the parameter R_s during the derivation, for brevity. Equation (2.25a) was solved for ρ_n' to give

$$\rho_n' = -\frac{a_0}{a_1} + \frac{1}{a_1}\rho_r. \tag{2.26}$$

Combining Eqs. (2.25b) and (2.26) yielded the first-oder approximated soil isoline equation:

$$\rho_n = \left(b_0 - \frac{a_0}{a_1}b_1\right) + \frac{b_1}{a_1}\rho_r. \tag{2.27}$$

2.4.2 Case-2 $(m_r, m_n) = (1, N)$: Asymmetric First-order-in-Red Approximation

The second case involves implementing asymmetric truncation orders: m_r and m_n. In this case, a first-order approximation was applied to the red reflectance, and N-th order terms were retained in the NIR reflectance. The corresponding system of equations could be expressed as:

$$\rho_r = a_0 + a_1\rho'_n, \tag{2.28a}$$

$$\rho_n = \sum_{i=0}^{N} b_i \rho'^i_n. \tag{2.28b}$$

Equation (2.28a) was solved for ρ'_n and substituted into Eq. (2.28b) to give the soil isoline equation:

$$\rho_n = \sum_{i=0}^{N} \frac{b_i}{a_1^i}(\rho_r - a_0)^i. \tag{2.29}$$

Equation (2.29) could also be expressed as:

$$\rho_n = \sum_{i=0}^{N} G_i \rho_r^i, \tag{2.30}$$

where the coefficients G_i are defined by

$$G_i = \sum_{\alpha=i}^{N} {}_{\alpha}C_i(-a_0)^{\alpha-i}\frac{b_\alpha}{a_1^\alpha}. \tag{2.31}$$

2.4.3 Case-3 $(m_r, m_n) = (N, 1)$: Asymmetric First-order-in-NIR Approximation

This case involves the same orders of approximation as Case-2, except that the bands assigned to the first and N-th order approximations were reversed. The red reflectance was approximated by a higher-order polynomial ($m_r = N$). The final

results were obtained by considering the reciprocal notation,

$$\rho_r = \sum_{i=0}^{N} H_i \rho_n^i, \tag{2.32}$$

where H_i represents a coefficient of the i-th order term of the NIR reflectance, defined by

$$H_i = \sum_{\alpha=i}^{N} {}_{\alpha}C_i (-b_0)^{\alpha-i} \frac{a_\alpha}{b_1^\alpha}. \tag{2.33}$$

2.4.4 Case-4 $(m_r, m_n) = (2, 2)$: Second-order Approximation

This work proceeded one step further to derive a different form of soil isoline equations that included higher-order terms (at most second-order terms in both reflectances). This case was represented by $(m_r, m_n) = (2, 2)$. The system of equations became

$$\rho_r = a_0 + a_1 \rho_n' + a_2 \rho_n'^2, \tag{2.34a}$$

$$\rho_n = b_0 + b_1 \rho_n' + b_2 \rho_n'^2. \tag{2.34b}$$

In this work, I solved Eq. (2.34a) for the index-like parameter ρ_n' to yield

$$\rho_n' = \frac{-a_1 \pm \sqrt{a_1^2 - 4a_2(a_0 - \rho_r)}}{2a_2}. \tag{2.35}$$

Note that Eq. (2.34b) could have been selected in place of Eq. (2.34a).

My numerical investigations indicated that the negative parts of the equations derived above always provided the correct solution, that is, the signature of the equations. Therefore, throughout the remainder of this study, the negative part of the equation was used in subsequent derivation steps. The origin of this result has not yet been clarified, and further investigations are needed. These investigations will be addressed in future studies. The derived expressions, based on the signature coefficients a_i and b_i, listed in Table 2.1, were further explored.

Substituting the values of ρ_n' in Eq. (2.35) into Eq. (2.34b) yielded a second-order approximation of the soil isoline equation,

$$\rho_n = b_0 - \frac{a_1 b_1 + 2a_0 b_2}{2a_2} + \frac{a_1^2}{2a_2^2} b_2 + \frac{1}{2a_2} \left(-b_1 + \frac{a_1}{a_2} b_2 \right) \sqrt{a_1^2 - 4a_2(a_0 - \rho_r)} + \frac{1}{a_2} b_2 \rho_r. \tag{2.36}$$

Table 2.1: Signature of the parameters a_i and b_i in Eqs. (2.17a) and (2.17b), based on numerical simulations.

Eq. (2.17a)			Eq. (2.17b)		
a_1	a_2	a_3	b_1	b_1	b_1
+	−	+	+	+/−	+

2.4.5 Case-5 $(m_r, m_n) = (N_r, N_n)$ Higher-order Approximation

The final case described in this study involved approximations using higher-order terms in both reflectances. It is difficult to solve higher-order polynomials analytically. These difficulties were avoided here simply by including the higher-order terms in the zeroth- order term. The analytical form derived in this study is only useful for symbolic manipulation; however, practical approximations may be inferred from this expression. The availability of a symbolic form enabled further analyses of problems in which soil isolines play an important role. For this reason, it is worthwhile discussing the derivation of the higher-order terms.

This derivation began with a parametric representation of the isoline equation,

$$\boldsymbol{\rho} = \left(\sum_{i=0}^{N_r} a_i \rho_n'^i, \sum_{i=0}^{N_n} b_i \rho_n'^i \right)^t . \tag{2.37}$$

I next included all terms of order greater than 2 in the zeroth-order term. The red reflectance could then be approximated by

$$\rho_r = a_0' + a_1 \rho_n', \tag{2.38}$$

where the zeroth-order term a_0' is a function of ρ_n', and the soil reflectance R_s through a_i is defined by

$$a_0' = a_0 + \sum_{i=2}^{N_r} a_2 \rho_n'^i. \tag{2.39}$$

The remainder of the derivation steps were similar to those introduced in subsection 3.4.2. The final form of the soil isoline equation became

$$\rho_n = \sum_{i=0}^{N_n} G_i' \rho_r^i, \tag{2.40}$$

where G_i' is a coefficient (similar to G) that includes the index-like parameter ρ_n' in

the red reflectance, up to the i-th order term,

$$G'_i = \sum_{\alpha=i}^{N_n} {}_{\alpha}C_i(-a'_0)^{\alpha-i}\frac{b_\alpha}{a_1^\alpha}. \tag{2.41}$$

Note that the value of a'_0 in Eq. (2.41) included the parameter ρ'_n (as well as the soil reflectance R_s), meaning that G'_i depended on both R_s and the biophysical parameter (LAI, in this study). This dependency distinguished this case from the case introduced in Subsection 3.4.2.

Equation (2.41) could not be used for numerical investigations in this study because a'_0 depended on ρ_n itself, and ρ_n could not be computed from Eq. (2.41); however, the availability of this formulation was beneficial in certain applications in which a good estimate for ρ_n was available. One such application is the cross-calibration of the VI. In such applications, the value of ρ_n for one sensor provided a good estimate for the corresponding band of the other sensor. More specifically, a'_0 of one sensor could be approximated by the reflectance of the other sensor. These applications will be investigated in future studies.

2.5 Validity of the Derived Relationship

The preceding sections introduced an approach to deriving the relationship between two reflectances given constant soil optical properties. Here, the soil isoline equations could be written simply as

$$\begin{bmatrix} \rho_r \\ \rho_n \end{bmatrix} = \begin{bmatrix} \sum_i a_i \rho_n'^i \\ \sum_i b_i \rho_n'^i \end{bmatrix}. \tag{2.42}$$

Although the derivation employed affine transformation and a polynomial fit, the fundamental physical basis for this relationship has not been fully explored. This study sought to address this issue by theoretically validating the derived soil isoline equation and numerically demonstrating its validity in the context of a radiative transfer model of a layered canopy-soil system. Specifically, the polynomial fits employed in the derivation were validated in an analysis based on the theory of radiative transfer.

During the derivation, the optimal polynomial approximation, represented by a set of p_i in the soil isoline equation, could not be distinguished. This section discusses the validity of the selected approach based on a representation of the TOC reflectance.

2.5.1 Derivation of the Soil Isoline Equations Using Additive Methods

The starting point was the following expression based on additive methods[111], used in the derivation of the vegetation isoline equation[82],

$$\rho_\lambda = \rho_{v\lambda} + T_{v\lambda}^2 R_{s\lambda} + O_\lambda^2, \tag{2.43}$$

where the last term represents the higher-order interaction terms between the canopy and soil surface, defined by

$$O_\lambda^2 = \frac{T_{v\lambda}^2 R_{s\lambda}^2 R_{v\lambda}}{1 - R_{v\lambda} R_{s\lambda}}. \tag{2.44}$$

In the above equations, $\rho_{v\lambda}$ is the vegetation canopy directional reflectance, $T_{v\lambda}^2$ represents two-way transmittance, and $R_{v\lambda}$ is the bi-hemispherical reflectance of the vegetation canopy for the background-reflected photons entering the bottom of the canopy layer and scattered back in the downward direction.

The derivation progressed by assuming that both the two-way transmittances $T_{v\lambda}^2$ and the pure vegetation reflectance $\rho_{v\lambda}$ could be approximated using a simple exponential function (Beer's law) of the LAI (L),

$$\rho_{v\lambda} \approx \rho_{v\lambda\max}(1 - \exp(-k_{1\lambda} L)), \tag{2.45}$$

$$T_{v_\lambda}^2 \approx \exp(-k_{2\lambda} L), \tag{2.46}$$

where $k_{1\lambda}$ and $k_{2\lambda}$ are the coefficients of exponential functions of $\rho_{v\lambda}$ and $T_{v\lambda}^2$, respectively, and $\rho_{v\lambda\max}$ represents the maximum value of $\rho_{v\lambda}$.

Substituting Eqs. (2.45) and (2.46) into Eq. (2.43) permitted the reflectance, expressed without the higher-order interaction term, to be expressed as

$$\rho_\lambda - O_\lambda^2 = \rho_{v\lambda\max}(1 - \exp(-k_{1\lambda} L)) + \exp(-k_{2\lambda} L) R_{s\lambda}. \tag{2.47}$$

I then expanded the above exponential functions in a Taylor series about some LAI value L_t to provide

$$\begin{bmatrix} \rho_r - O_r^2 \\ \rho_n - O_n^2 \end{bmatrix} = \begin{bmatrix} \sum_i c_i (L - L_t)^i \\ \sum_i d_i (L - L_t)^i \end{bmatrix}, \tag{2.48}$$

where

$$c_i = \begin{cases} R_{sr}\exp(-L_t k_{2r}) + \rho_{vR\max}(1-\exp(-L_t k_{1r})) \\ \qquad\qquad\qquad\qquad\qquad\qquad\qquad\qquad (i=0) \\ \frac{(-1)^i}{i!}(R_{sr}k_{2r}^i\exp(-L_t k_{2r}) - \rho_{vr\max}k_{1r}^i\exp(-L_t k_{1r})) \\ \qquad\qquad\qquad\qquad\qquad\qquad\qquad\qquad (i\neq 0) \end{cases} \tag{2.49}$$

$$d_i = \begin{cases} R_{sn}\exp(-L_t k_{2n}) + \rho_{vn\max}(1-\exp(-L_t k_{1n})) \\ \qquad\qquad\qquad\qquad\qquad\qquad\qquad\qquad (i=0) \\ \frac{(-1)^i}{i!}(R_{sn}k_{2n}^i\exp(-L_t k_{2n}) - \rho_{vn\max}k_{1n}^i\exp(-L_t k_{1n})) \\ \qquad\qquad\qquad\qquad\qquad\qquad\qquad\qquad (i\neq 0). \end{cases} \tag{2.50}$$

The above expression presents a theoretically derived soil isoline equation based on an analytical expression for the TOC reflectance.

Remarkably, the soil isoline equations derived through two different approaches (Eq. (2.42) and Eq. (2.48)) yielded the same polynomial form that differed only in terms of the common parameter and coefficients. Equation (2.42) indicates that the common parameter was ρ'_n, whereas the counterpart to Eq. (2.48) was expressed in terms of $(L - L_t)$. Recall that ρ'_n is equivalent to a distance-based VI, such as the WDVI. Because WDVI represents a biophysical parameter, the parameters ρ'_n and $(L - L_t)$ have the same physical import (a nearly one-to-one relationship, in some cases). For this reason, the two equations were considered to be physically equivalent, thereby validating Eq. (2.42).

2.5.2 Results and Discussion

A numerical experiment was conducted to support the theoretical model. The TOC reflectance was modeled using the radiative transfer code PROSAIL[99]. Wavelengths in the red and NIR bands were modeled based on the reflectances at 674 and 870 nm, respectively, which corresponded to the band center wavelengths of the GOSAT-CAI sensor.

The reflectance spectra determined using the model yielded the soil line parameters. The soil line slope and offset then became $s_1 = 1.20$ and $S_0 = 0.03$, respectively. The three sets of coefficients were determined such that $(\rho_{vr\max}, \rho_{vn\max}) = (0.0141, 0.4946)$, $(k_{1r}, k_{1n}) = (1.098, 0.349)$, and $(k_{2r}, k_{2n}) = (1.124, 0.514)$.

This work then investigated the errors in the theoretical soil isoline equation, Eq. (2.48), by comparing the right-hand side of Eq. (2.48) and the simulated reflectance

of the left-hand side of Eq. (2.48). Figure 2.5 shows the mean absolute differences (MAD) between the right-hand side and the left-hand side of Eq. (2.48) as an error in the derived soil isoline equation at various LAIs through an expansion of the 2nd Taylor series. The left figure represents the error in the red band, and the right figure represents the NIR band error. The MAD were obtained at four L_t values, namely, 0, 1, 2, and 4. The case of $L_t = 0$ corresponded to the Maclaurin series expansion.

The results revealed that the MAD became zero or nearly zero at or around the value of L_t in each case. These results indicated that the errors in Eq. (2.48) were reasonably small given the appropriate selection of L_t. Therefore, the soil isoline equation, Eq. (2.48), derived from an analytical representation of the TOC reflectance, Eq. (2.43), could approximate the simulated soil isoline reasonably well. Recall that the common parameter ρ'_n in Eq. (2.42) was equivalent to $L - L_t$ in Eq. (2.48). Also, recall that the two equations (Eqs. (2.42) and (2.48)) assumed the same form (power series). The above discussion (demonstrating the validity of Eq. (2.48) numerically), together with the equivalence of ρ'_n and $L - L_t$ and the form of the power series theoretically justified the expression of the soil isoline equation using Eq. (2.42) (its functional form), as long as the constants were appropriately selected.

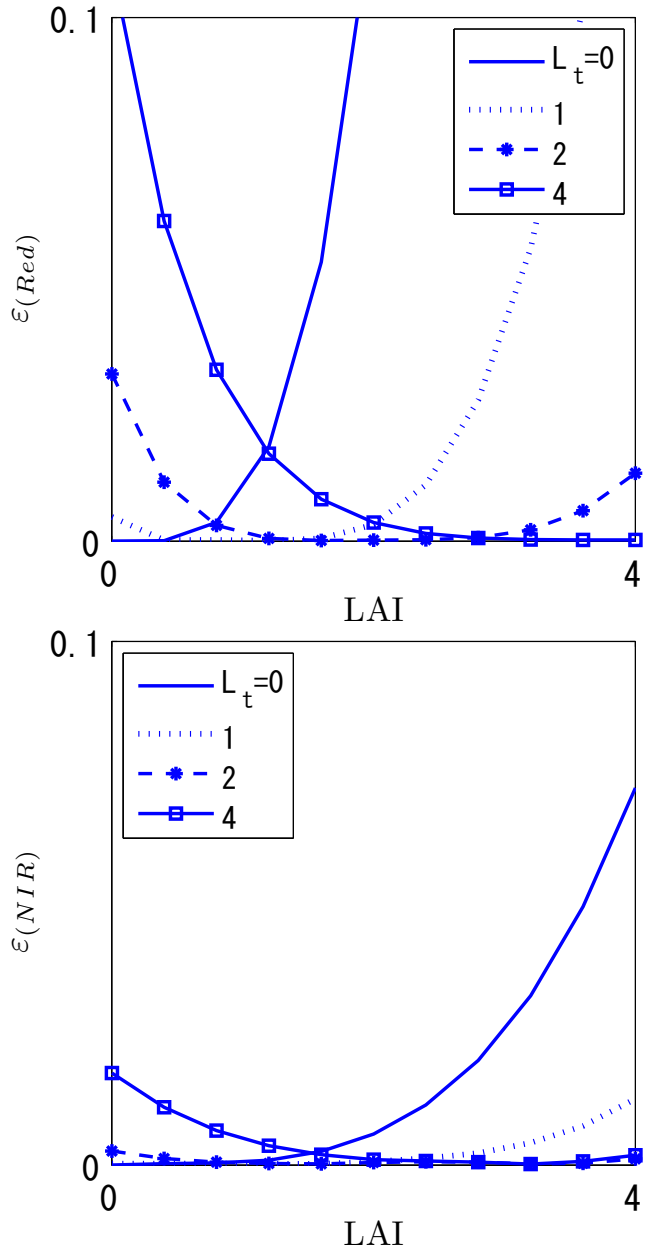

Figure 2.5: Plot of the mean absolute difference (MAD) between the red (top) and NIR reflectances (bottom). MAD was obtained as the difference between the theoretically derived soil isolines and the numerically simulated soil isolines, using PROSAIL as a function of the LAI.

2.6 Discussions

This study introduced a parametric form of the soil isoline equation, in which an index was used as a common parameter. Numerical difficulties associated with singularities in the original subspace were overcome by rotating the red and NIR axes through an angle equal to the soil line slope. Although the derived form included a common parameter, a polynomial of arbitrary order could be used to represent the soil isoline equation. The derived parametric form suffered from the drawback that the soil isoline equation implicitly (rather than explicitly) described the relationship between the red and NIR reflectances. An explicit form of the soil isoline was derived by considering a series of truncation cases.

The validity of the derived relationship was explored from a fundamental physics point of view. The theoretical validity of the derived soil isoline equation was numerically supported using a radiative transfer model of a layered canopy-soil system. The polynomial fits employed during the derivation were validated in an analysis based on the theory of radiative transfer. The resultant form was similar to the soil isoline equation derived previously based on the analytical form of the TOC reflectance.

The findings from this study may be summarized as follows: 1) The soil isoline equation based on a polynomial fit was functionally equivalent to the isoline derived from a radiative transfer model. 2) The previously derived isoline was more numerically stable and, hence, more suitable than the isoline derived using an RT model.

The major drawback of Eq. (2.42) was the use of a common parameter ρ'_n in the expression, because this expression did not guide the selection of optimal parameters. This point demands further investigation in the context of future studies. The spectral domains of the red and NIR subspaces should be relaxed to expand this anallysis to the wavelength range 400-2500nm for application to satellite data analysis, as summarized in Appendix A.

CHAPTER III

Soil Isoline Equations in the Red–Near-infrared Reflectance Subspace Describe a Heterogeneous Canopy

3.1 Introduction

The previous chapter derived the soil isoline under the assumption of full canopy coverage. In this case, the derived isoline equations were applicable only to regions in which a spatially homogeneous canopy covered the soil surface. These studies did not consider a heterogeneous target in which only a portion of the target region was covered by the canopy. Figure 3.1 shows a comparison of the soil isolines obtained from fully covered regions and partially covered regions in the red and NIR reflectance subspaces. The figure clearly reveals the differences between the two cases (black line and gray line). These differences could introduce errors into subsequent analyses of the isolines if one did not distinguish the two cases. These cases may be treated appropriately by introducing a parameter that represents the fractional area covered by the canopy into the soil isoline formulations. This study attempted to do this using a parameter called the fraction of vegetation cover (FVC)[38, 112–116].

This chapter describes the derivation of the soil isoline equations with consideration for the FVC. The objectives of this study were: (1) to derive the soil isoline equations without truncating the polynomials; (2) to approximate the derived isoline equations for the sake of practicality by truncating the higher-order terms to obtain an analytical form of the red and NIR reflectance relationships under conditions of a constant soil reflectance spectrum; and (3) to validate the derived results by conducting a set of numerical experiments using a radiative transfer model to describe the coupling between the leaf and canopy layer systems. The outline of the derivation is presented first with a summary of the key findings derived in Chapter 2. This

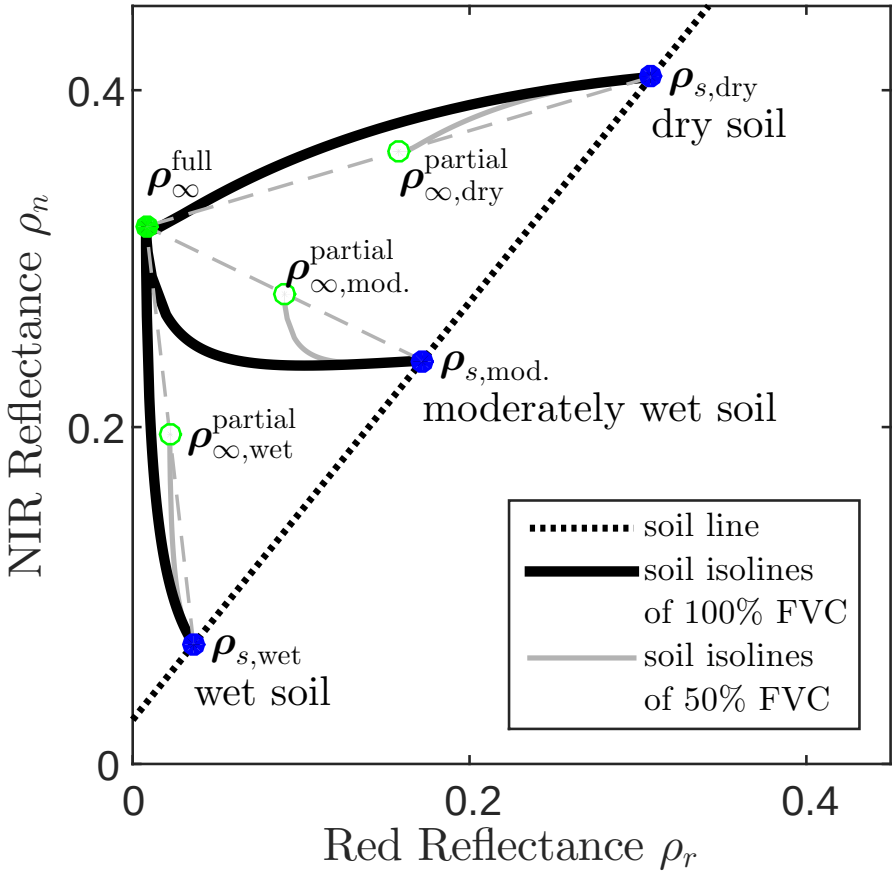

Figure 3.1: Comparison of (solid black lines) the soil isolines for full canopy coverage conditions, and (gray) soil isolines for partial (50%) canopy coverage conditions. The dotted line indicates the soil line in the red-NIR reflectance subspace. The green dot $\boldsymbol{\rho}_{\infty}^{\mathrm{full}}$ represents the convergent point for a fully covered dense canopy. Green circles $\boldsymbol{\rho}_{\infty,\mathrm{wet}}^{\mathrm{partial}}$, $\boldsymbol{\rho}_{\infty,\mathrm{mod.}}^{\mathrm{partial}}$, and $\boldsymbol{\rho}_{\infty,\mathrm{dry}}^{\mathrm{partial}}$ indicate partially covered canopies with different soil backgrounds, $\boldsymbol{\rho}_{s,\mathrm{wet}}$, $\boldsymbol{\rho}_{s,\mathrm{mod.}}$, and $\boldsymbol{\rho}_{s,\mathrm{dry}}$, which denote the reflectance spectra of wet, moderately wet, and dry soil surfaces, respectively. Blue dots on the soil line indicate soil spectra without canopy. The gray dashed lines indicate the lines between the spectra for pure soil and a fully covered canopy.

study then introduces models of an inhomogeneous system comprising the vegetation canopy and soil surface, describe precise derivations and approximation cases and provide numerical experiments using a radiative transfer model. Finally, I discuss the results by focusing on the accuracy of the derived and approximated soil isoline equations.

3.2 Background

This section and Figure 3.2 briefly summarize the 4 steps used to derive the soil isoline equation. The first step was the transformation of an original red and near infrared (NIR) reflectance subspace into a new subspace. This transformation consisted of rotation by the angle θ, defined as the slope of a soil line. The purpose of the transformation was to prevent singularities that could otherwise occur during the next step. The second step involved determination of the polynomial coefficients p_i of the i-th order term for each soil isoline in the transformed subspace. The relationship between the red and NIR reflectances was represented along a soil isoline using a polynomial in the new subspace. The number of coefficient sets was equal to the number of soil isolines. The third step involved the transformation of this relationship back into the original subspace to obtain a parametric representation of the soil isoline equation. The soil isolines were represented by power series of a common parameter. The final step involved the approximation of the soil isoline equations as relationships between the red and NIR reflectances of the original space by truncating the order of the common parameter. The approximated form of the soil isoline equation varied with the truncation order for each band. Hence, the accuracy of the derived isoline depended on the truncation orders of the two bands.

3.3 Parametric Representation of the Soil Isoline Equations For a Partially Vegetated Pixel

This section introduces the steps used to derive soil isoline equations that include a parameter to indicate the FVC, defined by ω. Please note that $(1 - \omega)$ represents the proportion of bare soil within a target pixel. Therefore, the parameter 'FVC' is tightly related to the soil parameter. In this context, it is quite natural to employ FVC in the soil isoline formulations. Although the derivation described here is similar to the one introduced in Chapter 2 for the case of full canopy coverage, care will be required to maintain consistency across the derived expressions and to clarify the differences between the fully covered and partially covered cases.

3.3.1 A Linear Mixture Model of the Top-of-Canopy Reflectance Spectra of Partially Vegetated Pixels

The starting point for the derivation was the assumption of a linear mixture model in which the top-of-canopy (TOC) spectrum was represented by a linear mixture of pure spectra known as endmember spectra[116]. Although the assumption of a

STEP-1: Transformation⋯Subsection 2.1

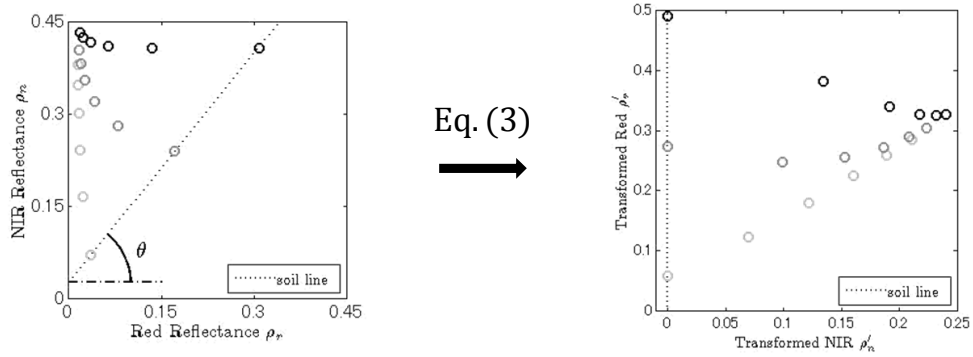

STEP-2: Determination of $p_i(R_s)$ ⋯ Subsection 2.2

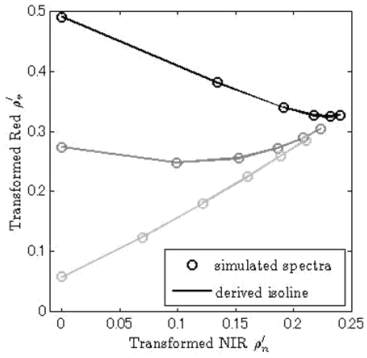

Soil Isoline Equation
in Transformed Red-NIR Space

$$\rho'_r = \sum_{i=0}^{\infty} p_i(R_s)\rho'^i_n \cdots \text{Eq. (14)}$$

STEP-3: Transformation ⋯Subsection 2.3

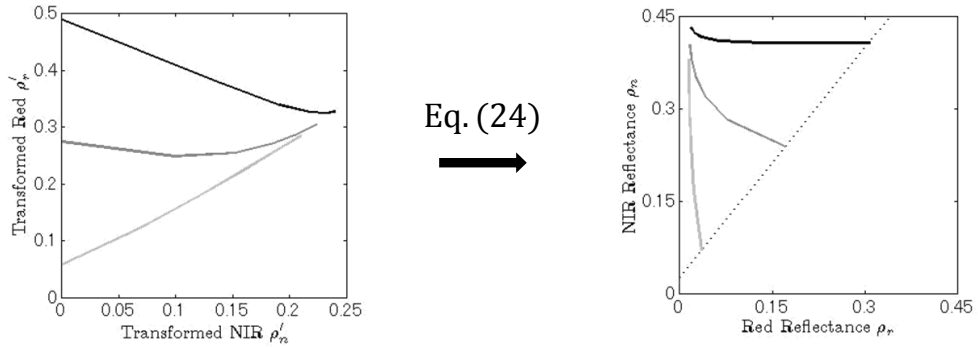

STEP-4: Approximation of Eq. (24) by truncation order (m_r, m_n) ⋯Section 3

	Case-1	Case-2	Case-3	Case-4	Case-5
m_r	1	1	N	2	N_r
m_n	1	N	1	2	N_n

Figure 3.2: Steps used to derive the soil isoline equations in the red and near-infrared (NIR) reflectance subspaces introduced in the previous chapter.

linear mixture was idealistic, it became a reasonably good estimate as the size of the target pixel increased. Thus, this assumption restricted the applicable range of this study to images acquired by satellites with moderate ($15 - 30$ m) to low spatial resolution. This study applied the two endmember linear mixture model (LMM) in the red and NIR reflectance subspaces, denoted by the subscripts 'r' and 'n', respectively. The subscripts 'v' and 's' denote vegetation and soil, respectively. The TOC spectrum, $\boldsymbol{\rho} = (\rho_r, \rho_n)$, was defined as the weighted sum of the vegetated and non-vegetated spectra, defined by $\boldsymbol{\rho}_v = (\rho_{vr}, \rho_{vn})$ and $\boldsymbol{\rho}_s = (\rho_{sr}, \rho_{sn})$, respectively. The TOC reflectance may then be expressed as

$$\boldsymbol{\rho} = \omega\boldsymbol{\rho}_v + (1 - \omega)\boldsymbol{\rho}_s. \tag{3.1}$$

This study also assumed that the soil layer underneath the canopy was homogeneous over the entire target pixel. These assumptions enabled us to represent the well-known relationship between the red (R_{sr}) and NIR (R_{sn}) reflectances of the soil surface using a single soil line[93, 117, 118],

$$R_{sn} = s_0 + s_1 R_{sr}, \tag{3.2}$$

where s_0 and s_1 represent the offset and slope of the soil line, respectively. In this study I explicitly differentiated the soil reflectance (R_{sr}, R_{sn}) as an input parameter from the output reflectance spectrum (ρ_{sr}, ρ_{sn}) of the soil line model.

The next step involved applying an affine transformation to the TOC reflectance spectrum. This transformation was needed to avoid singular points in the numerical treatment of the soil isolines across a broader range of LAI. In this study, the affine transformation of a vector $\boldsymbol{\rho}$ into $\boldsymbol{\rho}'$ was represented by the function φ, defined as

$$\varphi(\boldsymbol{\rho}) = T(-\theta)(\boldsymbol{\rho} - \boldsymbol{\tau}), \tag{3.3}$$

where the angle θ, matrix T and vector $\boldsymbol{\tau}$ are further defined by

$$\theta = \arctan(s_1), \tag{3.4}$$

$$T(-\theta) = \begin{bmatrix} \cos(\theta) & -\sin(\theta) \\ \sin(\theta) & \cos(\theta) \end{bmatrix}, \tag{3.5}$$

$$\boldsymbol{\tau} = (0, s_0). \tag{3.6}$$

Note that the parameter θ represents the angle between the X-axis and the soil line. Using these definitions, the transformed reflectance spectra of $\boldsymbol{\rho}$, $\boldsymbol{\rho}_v$, and $\boldsymbol{\rho}_s$ could be

written as

$$\boldsymbol{\rho}' = T(-\theta)(\boldsymbol{\rho} - \boldsymbol{\tau}), \tag{3.7}$$

$$\boldsymbol{\rho}'_v = T(-\theta)(\boldsymbol{\rho}_v - \boldsymbol{\tau}), \tag{3.8}$$

$$\boldsymbol{\rho}'_s = T(-\theta)(\boldsymbol{\rho}_s - \boldsymbol{\tau}). \tag{3.9}$$

Based on the linearity of the function φ, the following relation holds:

$$\boldsymbol{\rho}' = \omega\boldsymbol{\rho}'_v + (1-\omega)\boldsymbol{\rho}'_s. \tag{3.10}$$

The soil reflectance spectra became simple after the transformation because the transformed soil line was projected along the new red axis,

$$\boldsymbol{\rho}'_s = (\rho'_{sr}, 0), \tag{3.11}$$

where ρ'_{sr} is the offset of the transformed soil isoline equation in the new subspace,

$$\rho'_{sr} = \sqrt{\rho_{sr}^2 + (\rho_{sn} - s_0)^2} = \cos(\theta)\rho_{sr} + \sin(\theta)(\rho_{sn} - s_0). \tag{3.12}$$

The TOC reflectance spectrum after the transformation could be written explicitly as

$$\begin{bmatrix} \rho'_r \\ \rho'_n \end{bmatrix} = \omega \begin{bmatrix} \rho'_{vr} \\ \rho'_{vn} \end{bmatrix} + (1-\omega) \begin{bmatrix} \rho'_{sr} \\ 0 \end{bmatrix}. \tag{3.13}$$

Equation (3.13) suggested that the FVC parameter, ω, could be incorporated into the soil isoline equations describing the full canopy coverage with several modifications. Considering that the full canopy coverage is a special case of the partial canopy coverage, in which $\omega = 1$, the above analogy could be understood intuitively, and this work proceeded with the derivation steps according to this analogy.

3.3.2 Soil Isoline Equations in the Transformed Subspace

R_s represents a single input parameter along the soil line. R_s could be either R_{sr}, R_{sn}, or a ratio of wet and dry soil spectra. In either case, only a single parameter was needed to represent the model input. Therefore, I used R_s in the remainder of this Chapter. The previous work in Chapter 2 proposed using a polynomial fit as a function of the red soil reflectance R_s as a representative of the soil brightness. By defining p_i as a coefficient of the i-th order term, ρ'_{vr} could be expressed as a

polynomial of ρ'_{vn}, such as

$$\rho'_{vr} = \sum_{i=0}^{\infty} p_i(R_s)\rho'^i_{vn}. \tag{3.14}$$

The next step was to eliminate ρ'_{vr} and ρ'_{vn} from Eqs. (3.13) and (3.14). The result is an expression for the relationship between ρ'_r and ρ'_n,

$$\begin{aligned} \rho'_r &= \omega \sum_{i=0}^{\infty} p_i(R_s) \left(\frac{1}{\omega}\rho'_n\right)^i + (1-\omega)\rho'_{sr} && (3.15) \\ &= \xi + \sum_{i=1}^{\infty} \omega^{1-i} p_i(R_s)\rho'^i_n, && (3.16) \end{aligned}$$

where ξ represents the offset of the soil isolines, defined by

$$\xi = \omega p_0(R_s) + (1-\omega)\rho'_{sr}. \tag{3.17}$$

Note that $p_0(R_s)$ represents the offset of the soil isolines for the case of full canopy coverage in the transformed subspace. Because ρ'_{sr} itself indicates the intersection between the transformed soil line and the transformed soil isolines, this offset was identical to ρ'_{sr},

$$\rho'_{sr} = p_0(R_s). \tag{3.18}$$

Therefore, the offset of the soil isolines, ξ, was simply the offset for the case of a full canopy coverage,

$$\xi = p_0(R_s). \tag{3.19}$$

3.3.3 Parametric Representation of the Soil Isoline Equations for a Partially Covered Canopy

In the previous subsection, I derived the soil isoline equation in the transformed subspace. Next, I transformed the soil isoline equation back into the original red and NIR reflectance spaces. This process was performed by applying the inverse of the φ transformation,

$$\begin{aligned} \boldsymbol{\rho} &= \varphi^{-1}(\boldsymbol{\rho}') && (3.20) \\ &= T(\theta)\boldsymbol{\rho}' + \boldsymbol{\tau}. && (3.21) \end{aligned}$$

Although Eq. (3.21) included ρ'_r and ρ'_n as components of $\boldsymbol{\rho}'$ independently, ρ'_r can be written as ρ'_n from Eq. (3.16). Therefore, Eq. (3.21) could be written explicitly as a function of ρ'_n. Based on the relationship of Eq. (3.16) and Eq. (3.19), the parametric form of the soil isoline equation (Eq. (3.21)) became

$$\begin{bmatrix} \rho_r \\ \rho_n \end{bmatrix} = \begin{bmatrix} \cos(\theta) \\ \sin(\theta) \end{bmatrix} \rho'_r + \begin{bmatrix} -\sin(\theta) \\ \cos(\theta) \end{bmatrix} \rho'_n + \begin{bmatrix} 0 \\ s_0 \end{bmatrix} \tag{3.22}$$

$$= \begin{bmatrix} \cos(\theta) \\ \sin(\theta) \end{bmatrix} \left(p_0(R_s) + \sum_{i=1}^{\infty} \omega^{1-i} p_i(R_s) \rho'^i_n \right) + \begin{bmatrix} -\sin(\theta) \\ \cos(\theta) \end{bmatrix} \rho'_n + \begin{bmatrix} 0 \\ s_0 \end{bmatrix}. \tag{3.23}$$

For the sake of simplicity, this work further introduced the following notation to describe the soil isoline equation,

$$\begin{bmatrix} \rho_r \\ \rho_n \end{bmatrix} = \begin{bmatrix} \boldsymbol{a}' \\ \boldsymbol{b}' \end{bmatrix} \boldsymbol{\rho}'_n, \tag{3.24}$$

where $\boldsymbol{\rho}'_n$ is a vector composed of the series ρ'_n, and $\boldsymbol{a}'$ and $\boldsymbol{b}'$ are vectors in a series of coefficients used to describe the polynomials of ρ'_n, defined by

$$\boldsymbol{\rho}'_n = [1 \;\; \rho'_n \;\; \rho'^2_n \cdots]^{\mathrm{t}}, \tag{3.25}$$

$$\boldsymbol{a}' = [a'_0(R_s,\omega) \;\; a'_1(R_s,\omega) \;\; a'_2(R_s,\omega) \cdots], \tag{3.26}$$

$$\boldsymbol{b}' = [b'_0(R_s,\omega) \;\; b'_1(R_s,\omega) \;\; b'_2(R_s,\omega) \cdots], \tag{3.27}$$

where the coefficients $a'_i(R_s,\omega)$ and $b'_i(R_s,\omega)$ are defined using the Kronecker delta δ_{ij},

$$a'_i(R_s,\omega) = \delta_{i0}(\cos(\theta)p_0(R_s)) + (1-\delta_{i0})(-\sin(\theta)\delta_{i1} + \cos(\theta)\omega^{1-i}p_i(R_s)), \tag{3.28}$$

$$b'_i(R_s,\omega) = \delta_{i0}(\sin(\theta)p_0(R_s) + s_0) + (1-\delta_{i0})(\cos(\theta)\delta_{i1} + \sin(\theta)\omega^{1-i}p_i(R_s)). \tag{3.29}$$

Note that the zeroth-order terms of the polynomials describing each reflectance are equal to the spectra of the soil underneath the vegetation canopy $\boldsymbol{\rho}_s$,

$$\boldsymbol{\rho}_s = \begin{bmatrix} \cos(\theta)p_0(R_s) \\ \sin(\theta)p_0(R_s) + s_0 \end{bmatrix}. \tag{3.30}$$

Thus, all isolines approximated by any order will contain the true soil spectra and

will agree exactly with the soil spectra, regardless of the approximation order, for the zero vegetation case.

3.4 Approximations of the Soil Isoline Equation

This section introduces several approximate forms of the soil isoline equations based on the introduction of various truncation terms in Eq. (3.24). Let's define the integers m_r and m_n as the polynomial orders employed in the red and NIR reflectances, respectively. The truncation terms could be explicitly differentiated by expressing Eq. (3.24) in the following form:

$$\rho_r = \sum_{i=0}^{m_r} a'_i(R_s, \omega)\rho'^i_n + \cos(\theta)O(\rho'^{\,m_r+1}_n), \tag{3.31}$$

$$\rho_n = \sum_{i=0}^{m_n} b'_i(R_s, \omega)\rho'^i_n + \sin(\theta)O(\rho'^{\,m_n+1}_n), \tag{3.32}$$

where the function O represents the contributions of the higher-order terms.

The soil isoline equation could be approximated by choosing a pair of integers for m_r and m_n. Larger values would provide greater accuracy in the approximated soil isoline. The drawback, however, of choosing larger values for m_r and m_n is the increased difficulty associated with solving these equations for ρ'_n to derive analytical formulations of the soil isoline.

In Chapter 2, I introduced a series of derivations to approximate the soil isolines by assuming full canopy coverage. In these derivations, the value of the FVC parameter ω did not appear explicitly in the study; nevertheless, it was considered as a special case in which the FVC was fixed to unity. Under these conditions, the following derivations are consistent with those described in Chapter 2. This point will be explored carefully below during the derivation steps.

The analogy described above was used to guide the derivations first by simply enumerating the differences between the isolines of the fully covered case and of the partially covered case. I first clarified the differences between the coefficients defined in the previous study, $a_i(R_s)$ and $b_i(R_s)$, and the coefficients defined in this study $a'_i(R_s, \omega)$ and $b'_i(R_s, \omega)$. The major difference between the two cases (fully covered case and partially covered case) could be summarized in terms of the ratio of the coefficients a'_i and b'_i to their counterparts a_i and b_i, respectively, as follows:

$$\frac{a'_i(R_s, \omega)}{a_i(R_s)} = \frac{b'_i(R_s, \omega)}{b_i(R_s)} = \begin{cases} 1 & (i = 0, 1) \\ \omega^{1-i} & (i < 1). \end{cases} \tag{3.33}$$

Because the differences only arose in the second- and higher-order terms, the approximated soil isoline equation could be modified under full canopy coverage conditions according to the following correction rules:

$$a_i(R_s) \rightarrow \begin{cases} a_i(R_s) & (i = 0, 1) \\ \omega^{1-i} a_i(R_s) & (i = 2, 3, \cdots) \end{cases} \tag{3.34}$$

$$b_i(R_s) \rightarrow \begin{cases} b_i(R_s) & (i = 0, 1) \\ \omega^{1-i} b_i(R_s) & (i = 2, 3, \cdots). \end{cases} \tag{3.35}$$

3.4.1 Case-1 $(m_r, m_n) = (1, 1)$: First-order Approximation of the Soil Isoline Equation

The first case to which the soil isoline approximation was applied comprised a model of the reflectance spectra in which only on the zeroth- and first-order terms were used to describe the red and NIR reflectances. This rule, summarized as (3.34) and (3.35), held that all coefficients (a_0, a_1, b_0, and b_1) described in the previous studies remained unchanged. Therefore, the first-order approximated soil isoline equation was identical to the previously derived result,

$$\rho_n = \left(b_0 - \frac{a_0}{a_1} b_1 \right) + \frac{b_1}{a_1} \rho_r. \tag{3.36}$$

Note that the approximated isoline did not include the parameter ω, indicating that this approximation was not suitable for conditions of partial canopy coverage. This parameter could be thought of as enhancing the nonlinearity of the soil isolines.

3.4.2 Case-2 $(m_r, m_n) = (1, N)$: Asymmetric First-order-in-Red Approximation

In this case, higher-order terms ($m_n \geq 2$) were included in the NIR reflectance. Therefore, the influence of the FVC appeared in the NIR. The influence of these terms was explicitly differentiated by introducing a logical function $\Delta_\alpha(\omega)$ in place of the integer α, defined by

$$\Delta_\alpha(\omega) = \delta_{\alpha 0} + (1 - \delta_{\alpha 0}) \omega^{1-\alpha}. \tag{3.37}$$

This newly defined function was used to derive the soil isoline equation for a partial canopy coverage by applying the correction rules (3.34) and (3.35) to the results

introduced in Chapter 2. We then obtained an approximated isoline,

$$\rho_n = \sum_{i=0}^{N} G_i \rho_r^i, \tag{3.38}$$

where the coefficient G_i was defined by

$$G_i = \sum_{\alpha=i}^{N} {}_\alpha C_i (-a_0)^{\alpha-i} \frac{b_\alpha}{a_1^\alpha} \Delta_\alpha(\omega). \tag{3.39}$$

3.4.3 Case-3 $(m_r, m_n) = (N, 1)$: Asymmetric First-order-in-NIR Approximation

This approximation case involved the same orders of approximation as Case-2, except that the bands assigned to the first- and N-th-order approximations were reversed: The red reflectance was approximated by a higher-order polynomial ($m_r = N$). The reciprocity resulting from the alternate band assignment yielded an expression for the approximated isoline,

$$\rho_r = \sum_{i=0}^{N} H_i \rho_n^i, \tag{3.40}$$

where H_i represents the coefficient of the i-th-order term describing the NIR reflectance, defined by

$$H_i = \sum_{\alpha=i}^{N} {}_\alpha C_i (-b_0)^{\alpha-i} \frac{a_\alpha}{b_1^\alpha} \Delta_\alpha(\omega). \tag{3.41}$$

3.4.4 Case-4 $(m_r, m_n) = (2, 2)$: Second-order Approximation

The second-order soil isoline included the FVC parameter ω in both bands because the second-order terms were influenced by the FVC. Application of the correction rule to the previously derived expression yielded the following result:

$$\rho_n = b_0 - \frac{a_0 b_2}{a_2} + \frac{b_2}{a_2}\rho_r + \frac{\omega}{2a_2^2}(a_1 b_2 - a_2 b_1)(a_1 + I(R_s, \omega, \rho_r)), \tag{3.42}$$

where the function $I(R_s, \omega, \rho_r)$ was defined by

$$I(R_s, \omega, \rho_r) = \sqrt{a_1^2 - \frac{4a_2}{\omega}(a_0 - \rho_r)}. \tag{3.43}$$

Note that only the last term depended on the parameter ω. Special caution is needed in evaluating the above expression numerically because the denominator in $I(R_s, \omega, \rho_r)$ contains ω, which can be equal to zero. As ω approached zero, the reflectance spectrum on the isoline converged to the soil reflectance spectrum $\boldsymbol{\rho}_s$. Care is needed only in the context of numerical algorithmic treatments of this approximated form. This form of approximation is useful in a variety of applications, in addition to its utility in future studies.

3.4.5 Case-5 $(m_r, m_n) = (N_r, N_n)$: Higher-order Approximations

The last case comprises higher-order approximations in both the red and NIR bands. As described in a previous study, a rigorous solution to this approximation is impossible because the given equation cannot be solved for ρ_n analytically. This work circumvented this difficulty by including a higher-order term in the zeroth order expression. In this way, I explicitly represented the higher-order contribution to the approximated formulation, as described in Chapter 2. As a result, the derivation was similar to the derivation introduced in Subsection 3.4.2, and the final approximation form became

$$\rho_n = \sum_{i=0}^{N_n} G'_i \rho_r^i, \tag{3.44}$$

where G'_i is a coefficient (similar to G) that includes the index-like parameter ρ'_n in the red reflectance, up to the i-th-order term,

$$G'_i = \sum_{\alpha=i}^{N_n} {}_\alpha C_i (-a'_0)^{\alpha-i} \frac{b_\alpha}{a_1^\alpha} \Delta_\alpha(\omega), \tag{3.45}$$

and

$$a'_0 = a_0 + \sum_{i=2}^{N_r} \omega^{1-i} a_i \rho_n'^i. \tag{3.46}$$

Note that the value of a'_0 in Eq. (3.45) includes the parameter ρ'_n (in addition to the soil reflectance R_s), meaning that G'_i also depends on both R_s and the biophysical parameter (LAI, in this study). This dependency distinguished this approximation case from the one introduced in subsection 3.4.2.

The expression for Eq. (3.45) could not immediately be used in numerical investigations because a'_0 depended on ρ_n itself, which could not be computed from

Eq. (3.45). Nevertheless, the availability of this formulation is beneficial to certain applications for which a good estimate of ρ_n is available. One such application is the inter-calibration of multiple sensors. For example, the spectral vegetation indices measured from two or more different sensors may be used simultaneously in a study, provided that the sensors are inter-calibrated. In such applications, the value of ρ_n for one sensor provides a good estimate of the other sensor's corresponding band.

The soil isoline equation used in the higher-order case could be useful in practice to achieve inter-sensor calibration involving hyperspectral sensors. In such an application, the band reflectance (as from a destination sensor) would be available, regardless of the band configuration of the multispectral sensor; hence, relatively low-order terms would be required. Without losing practicality, better accuracy would be expected from the use of a higher-order approximation of the soil isoline equation.

3.5 Numerical Methods

The validity of each derived soil isoline equation was evaluated using a series of numerical experiments involving a coupled leaf–canopy radiative transfer model, PROSAIL[96, 97, 99]. To allow for a comparison between the current evaluation results and a previous study results (obtained from the fully covered case), the experimental conditions were summarized in Table 3.1.

Special caution is needed in treatment of the FVC value ω in this study. The meaning of ω is an aerial proportion of a target region that can be represented by the PROSAIL model. When the LAI is less than unity, the true FVC value becomes less than unity within the homogeneous canopy region simulated by PROSAIL. Therefore, the actual FVC value over the entire region becomes smaller than ω when the LAI value is less than unity. By use of this definition, we maintain consistency with the derivation and numerical results of the derived soil isolines in the case of a fully covered canopy.

Three PROSAIL parameters were varied during the experiments: the LAI, soil mixture ratio between the wet and dry soil spectra included in PROSAIL, which basically determined the soil brightness, and the FVC. PROSAIL was used to simulate the TOC spectra of the vegetated portion of the target area, and these spectra were then linearly mixed with the soil reflectance spectra to model the TOC spectra of the partial canopy coverage. This study assumed a spherically uniform value for LAD, and the 10 and 30 degree angles were set as the view-zenith and illumination angles, respectively. The nominal parameter sets used to describe the leaf chemical content reported in reference[119] were applied in the current experiments. These simulation

steps are summarized in Fig. 3.3.

The reflectance spectra collected from the vegetated area could be obtained as an output from PROSAIL. The wavelengths of the output reflectance fell in the range 400–2500 nm. This spectrum depended only on LAI, the soil brightness, and FVC in this study. Next, the reflectances of the red and NIR bands were simulated at 660 nm and 850 nm, respectively, based on the band center wavelength of the GOSAT-CAI (Greenhouse Gases Observing Satellite-Cloud and Aerosol Imager). The pure reflectance from a bare soil surface (a representative non-vegetated surface) was also simulated based on a linear sum of two standard soil spectra included in PROSAIL. An LAI of 0–4 at 0.8 intervals was set. Note that the approximated coefficients p_i depended somewhat on the maximum value of the LAI. In practical applications involving actual satellite images, these coefficient should be optimized using a training data set with known biophysical parameters and soil properties.

Table 3.1: Input parameters of PROSAIL assumed in this study.

Illumination and viewing condition	
Solar zenith angle	30 degrees
View zenith angle	10 degrees
Relative azimuthal angle	0 degrees
Canopy properties	
Hot spot parameter	0.01
Leaf area index	0-to-4 (1/2 intervals)
Pixel heterogeneous property	
Fractional vegetation cover	0-to-1 (1/10 intervals)
Leaf chemical and structure properties	
Brown pigment content	0.0
Carotenoid content	8 $\mu\mathrm{g}\cdot\mathrm{cm}^{-1}$
Chlorophyll content	40 $\mu\mathrm{g}\cdot\mathrm{cm}^{-1}$
Dry matter content	0.009 $\mu\mathrm{g}\cdot\mathrm{cm}^{-1}$
Leaf angle distribution	spherical†
Leaf equivalent water	0.01 cm
Leaf structure parameter	1.5
Soil properties	
Wet soil reflectances at 660&850 nm	0.038&0.071
Dry soil reflectances at 660&850 nm	0.315&0.408
Soil mixture ratio (SMR)‡	0-to-1 (1/6 intervals)

†In PROSAIL, spherical LAD is modeled setting $(\mathrm{LIDF}_a, \mathrm{LIDF}_b) = (-0.35, -0.15)$ where LIDF represents leaf inclination distribution function

‡ SMR is used to simulate various soil spectra, such as $\boldsymbol{\rho}_s = \mathrm{SMR}\boldsymbol{\rho}_{s,\mathrm{wet}} + (1 - \mathrm{SMR})\boldsymbol{\rho}_{s,\mathrm{dry}}$.

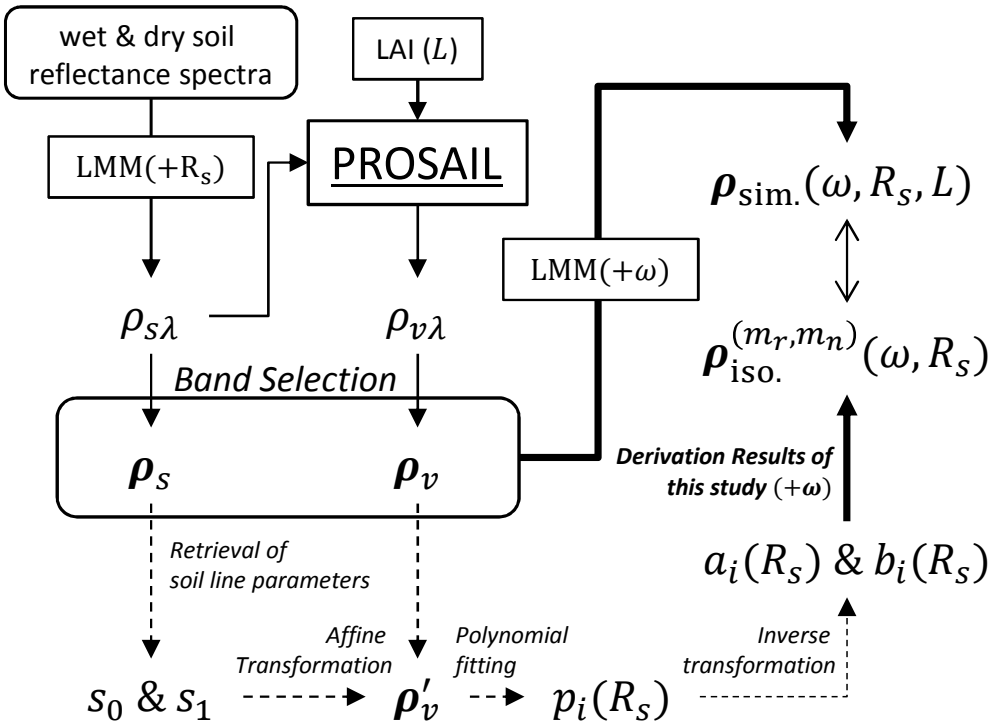

Figure 3.3: Flowchart describing the numerical procedure applied in the present experiments.

A relationship between LAI and FVC was not assumed during the simulation. Thus, both LAI and FVC were mutually independent in this study. The FVC ω (varied from 0.0 to 1.0) was defined as the ratio of an output from PROSAIL to the bare soil spectrum. The spectra obtained from the two-band LMM depended on the soil brightness, LAI, and FVC. These simulated TOC reflectance spectra were considered to be the true spectra in this study.

Most of the variables used in the approximated isolines were set equal to the corresponding values introduced in Chapter 2 (of a fully covered case). Therefore, the steps of preparing the variables used in the isoline formulations were almost the same as those applied in the case of full canopy coverage. In the case of full canopy coverage, the variables used in the soil isoline could be determined by following four steps: (1) retrieving the soil line parameters (slope and offset) from the reflectance spectra of the bare soil surface, (2) applying an affine transformation to the numerically simulated reflectance spectra, (3) fitting the transformed spectra along the soil isoline to a polynomial to obtain the fitting coefficients (p_i), (4) applying the inverse transformation back to the original red–NIR reflectance subspace to obtain the coefficients of the soil isoline equations (a_i, b_i).

The variables in the soil isoline equation for the case of partial canopy coverage were then computed by combining the parameter ω with the variables prepared according to the above four steps. The validity of the expressions derived in the previous section was tested by evaluating nine approximate cases defined by different pairs of m_r and m_n, representing the order of the terms used for the red and NIR bands, respectively. This study assumed values of 1–3 for both m_r and m_n, which resulted in nine combinations. Table 3.2 lists the expressions used to approximate the soil isolines in this study.

3.6 Results and Discussion

Figure 3.4 shows plots of the soil isolines simulated numerically by PROSAIL and the those approximated using the expressions derived for fully covered and partially covered canopy cases. The marks denote the true reflectance spectra along each soil isoline, whereas the lines represent the soil isolines approximated by the derived expressions. The isolines were obtained by assuming three different soil brightness values for two approximation cases defined by two pairs of m_r and m_n. The figure indicated that the approximated soil isolines were close to the true isolines, even for the case of partial canopy coverage. At the same time, the choice of m_r and m_n influenced the accuracy of the isolines (the difference between the marks and lines). These results qualitatively suggested the validity of the derived expression. We next conducted a quantitative evaluation of the soil isolines.

The accuracy of each of the nine soil isoline approximation cases was defined as the difference between the the simulated spectra (considered to be the true spectra in this study) and the approximated isolines. Figure 3.4 shows the isolines and simulated spectra obtained for an FVC value of 0.5 or 1.0 at three soil brightness levels for (left) $m_r = 1$ and $m_n = 2$ and (right) $m_r = 2$ and $m_n = 1$. As shown in Fig. 3.4, the accuracy of the isoline depended on the choice of the integer pair for m_r and m_n. This trend should be clarified quantitatively. The error $\varepsilon^{(m_r,m_n)}$ was defined as the norm of the vector spanned by the simulated spectra $\boldsymbol{\rho}_{\text{sim.}}$ and the derived isolines

Table 3.2: Summary of the approximated soil isoline equations used in the numerical experiments.

# of truncated order	$m_r = 1$	$m_r = 2$	$m_r > 2$
$m_n = 1$	Eq. (3.36) in 3.1	Eq. (3.40) in 3.3	Eq. (3.40) in 3.3
$m_n = 2$	Eq. (3.38) in 3.2	Eq. (3.42) in 3.4	Eq. (3.44) in 3.5
$m_n > 2$	Eq. (3.38) in 3.2	Eq. (3.44) in 3.5	Eq. (3.44) in 3.5

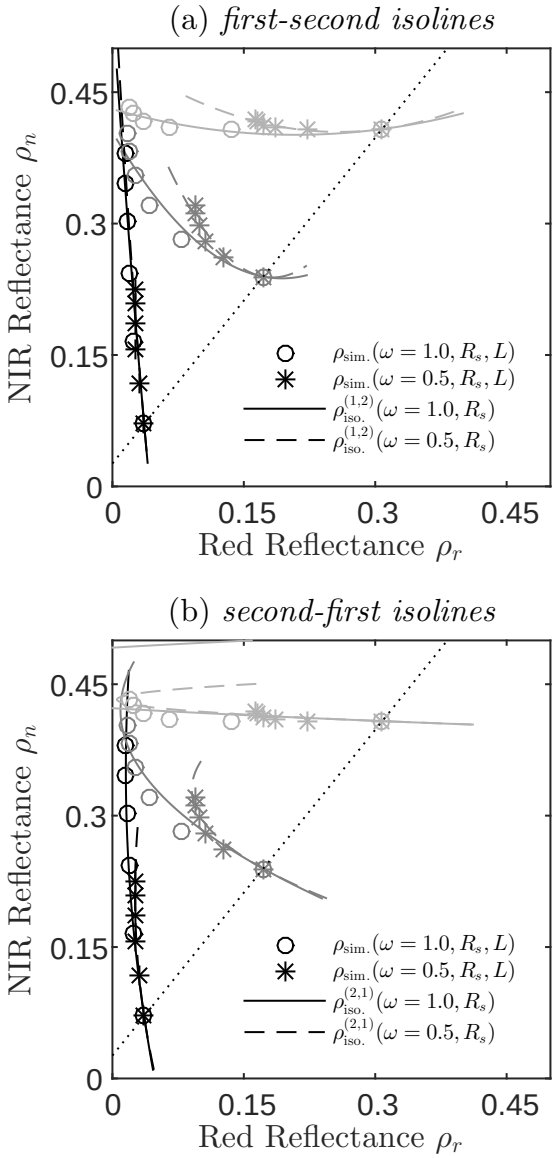

Figure 3.4: Comparisons between the approximated soil isoline equations and the 'true' reflectance spectra simulated by PROSAIL. (a) The isolines approximated based on the truncation orders $m_r = 1$ and $m_n = 2$, and (b) the isolines approximated based on the truncation orders $m_r = 2$ and $m_n = 1$. The solid lines denote the case of FVC=1.0 (fully covered case), and the dashed lines denote the case of FVC=0.5 (partially covered case). The isolines for three types of soils with different brightness values (wet, intermediate, and dry) are shown in each case.

$\boldsymbol{\rho}_{\text{iso.}}$ characterized by m_r and m_n. As a result, $\varepsilon^{(m_r,m_n)}$ may be expressed as a function of FVC ω, the soil brightness R_s, and LAI may be denoted L, as

$$\varepsilon^{(m_r,m_n)}(\omega, R_s, L) = \min||\boldsymbol{\rho}_{\text{sim.}}(\omega, R_s, L) - \boldsymbol{\rho}_{\text{iso.}}^{(m_r,m_n)}(\omega, R_s)||_2. \tag{3.47}$$

Figure 3.5 shows plots of the distance profiles of the approximated isolines and the true spectra. The distances were plotted as a function of LAI and soil brightness (soil reflectance of the red band), and the value of FVC was assumed to be 0.5 for all plots. The order of the error was clarified by presenting the plots on a logarithmic scale. The nine plots were arranged from top to bottom (row-wise) for different choices of $m_n = 1 - 3$. The plots were arranged from left to right (column-wise) for the values of $m_r = 1 - 3$ as well. The figure shows that the distance became shorter (hence, the error became smaller) as the choice of both m_r and m_n increased. These results indicated that the approximate soil isolines were better for the cases involving higher-order truncations, indicating the validity of the derivation.

Figure 3.6 shows plots of the average differences between each isoline as a function of the FVC and soil brightness, for the nine cases. The figures clearly indicated that the errors remained mostly stable, meaning that the order of the error generally depended on the order of the truncation. Moreover, the approximated isoline derived in this study nicely followed the variations in FVC.

The overall trend in the error was confirmed by plotting the trends in the error and the standard deviation (STD). Figure 3.7 shows the averaged error and the STD for each isoline for all cases. The overall trend in the relationship indicated that the STD decreased as the error decreased. Considering the effects of the FVC, the error of the smaller FVC resulted in a smaller STD. These results implied that the maximum error and STD tended to occur at the highest FVC value.

The overall averaged error and STD values for each case are summarized in Table 3.3. Three different LAD values (spherical, planophile and erectophile) were compared to elucidate the influence of these values on the error and STD. The results revealed that both the error and its STD were reduced along with the higher-order terms in the approximated soil isolines. These results confirmed the validity of the derived expressions.

The results of this study, based on a comparison of the results of the previous study, which assumed a fully covered canopy, indicated that the accuracy of the soil isoline equation improved as the vegetation coverage became smaller than unity. The contribution of the canopy layer became smaller as the FVC value becomes larger, giving rise to this effect. This study implicitly assumed that the soil line used in this

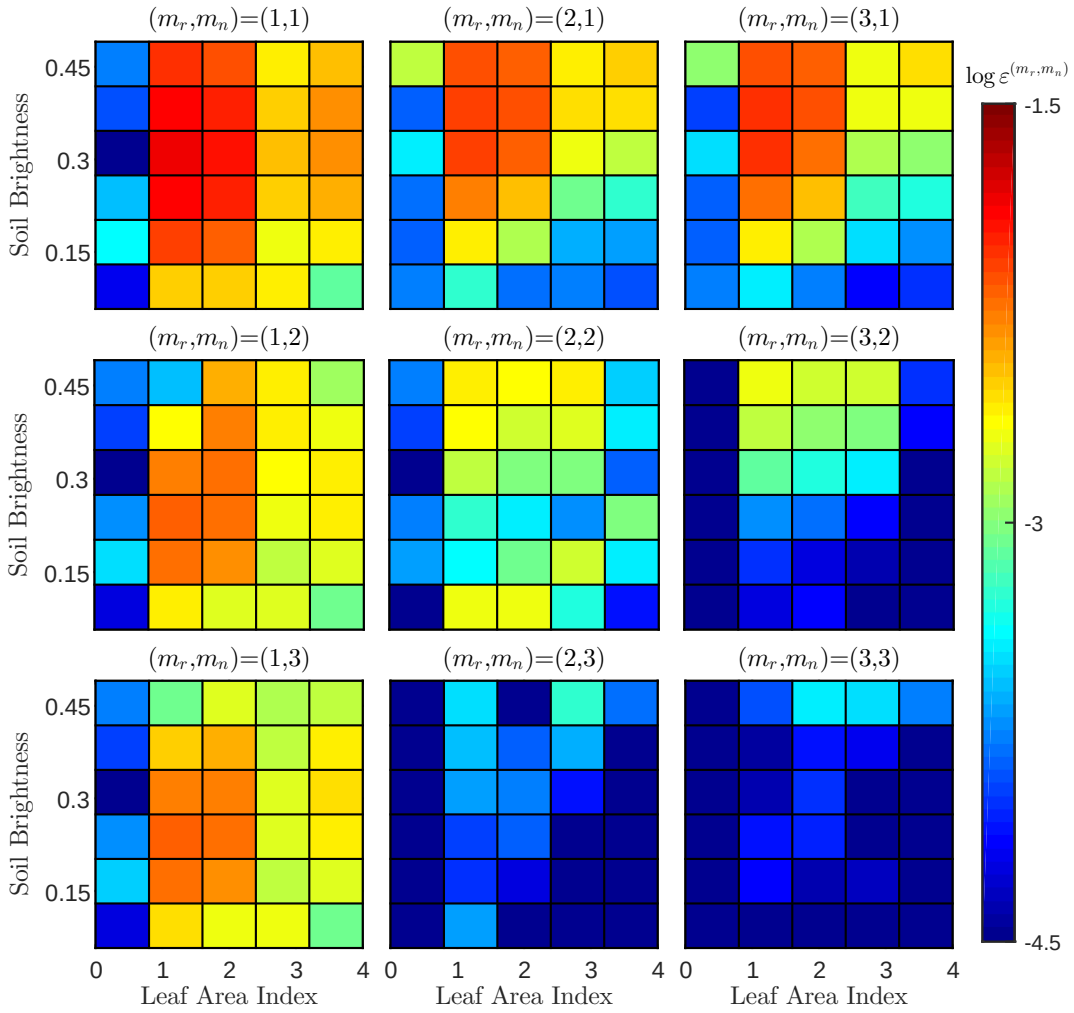

Figure 3.5: Errors associated with the approximated soil isolines for nine combinations of the truncation order. The errors are plotted as a function of LAI and soil brightness (soil reflectance of the red band.) The FVC parameter was fixed to 0.5 during the simulations.

study included no errors. In reality, a soil line always includes a certain degree of uncertainty when the slope and offset are determined numerically. The derived soil isoline equations are, therefore, limited. The derivation assumed a certain model for the soil reflectance spectrum, and errors in the soil model would be expected to propagate into the soil isoline equations. The effects of the soil model uncertainties should be investigated thoroughly in a future study. At the same time, accommodation of a better soil spectral model should also be explored.

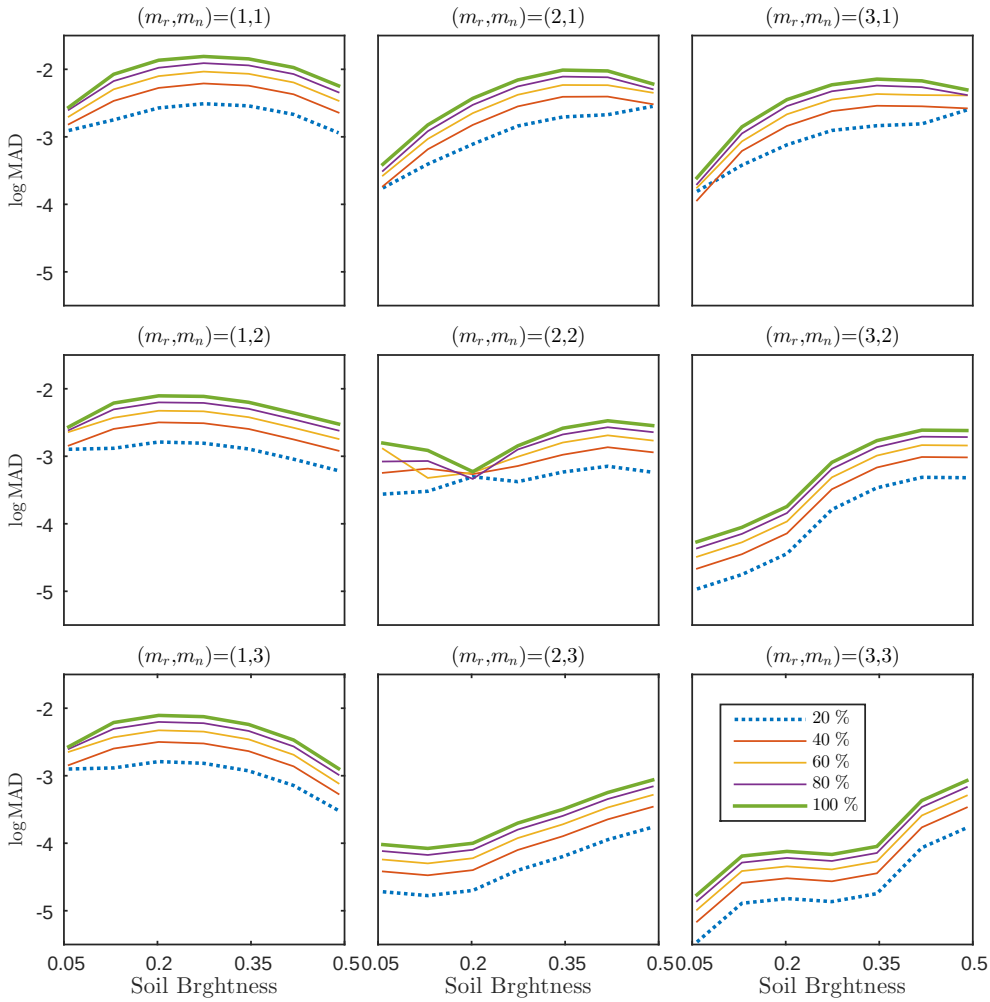

Figure 3.6: Plots of the mean absolute differences (MAD) between each soil isoline as a function of the FVC and soil brightness, for nine combinations of the truncation order.

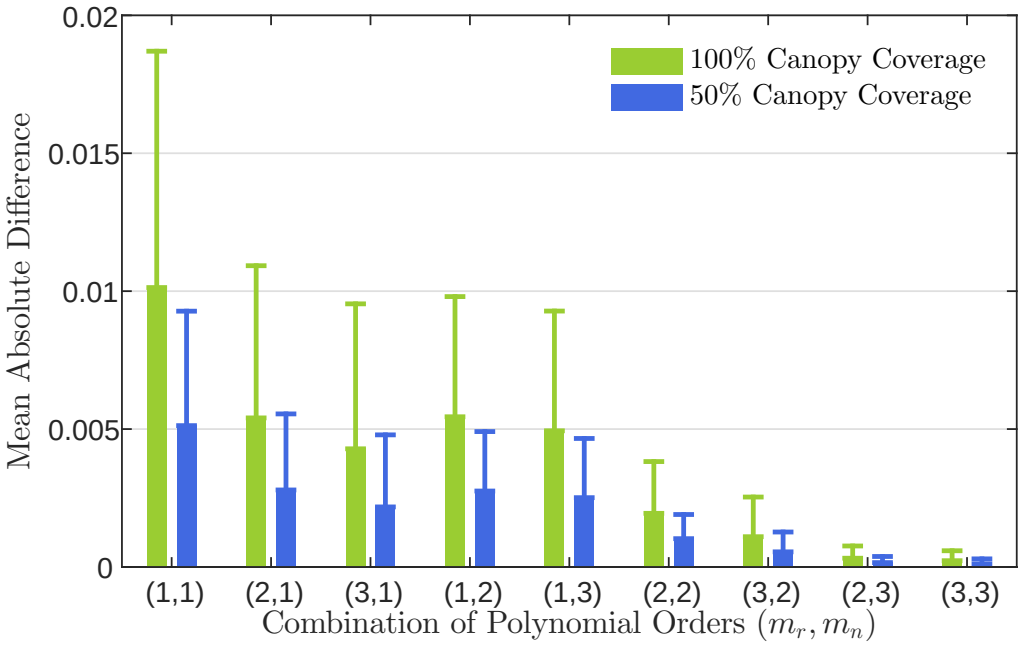

Figure 3.7: Overall score of (bar) MAD and (line) a STD for each soil isoline equation derived with the combination of polynomial orders (m_r, m_n). The bars and lines in green color indicate the scores for 100% canopy coverage, whereas those in blue color indicate 50% canopy coverage.

Table 3.3: Mean error of the approximated soil isoline equations for the three cases of LAD; (a) Spherical, (b) Planophile and (c) Erectophile.

(a) Spherical

(m_r, m_n)	(1,1)	(2,1)	(3,1)	(1,2)	(1,3)
Mean	5.6E-03	3.1E-03	2.5E-03	3.1E-03	2.8E-03
Std. Dev.	6.0E-03	3.7E-03	3.5E-03	3.1E-03	3.0E-03
(m_r, m_n)	(2,2)	(3,2)	(2,3)	(3,3)	
Mean	1.1E-03	6.0E-04	1.7E-04	1.3E-04	
Std. Dev.	1.2E-03	9.5E-04	2.9E-04	2.3E-04	

(b) Planophile

(m_r, m_n)	(1,1)	(2,1)	(3,1)	(1,2)	(1,3)
Mean	5.7E-03	3.1E-03	2.5E-03	3.1E-03	2.8E-03
Std. Dev.	3.8E-03	3.7E-03	3.5E-03	3.1E-03	3.1E-03
(m_r, m_n)	(2,2)	(3,2)	(2,3)	(3,3)	
Mean	1.4E-03	6.1E-04	1.8E-04	1.2E-04	
Std. Dev.	1.4E-03	9.6E-04	3.0E-04	2.3E-04	

(c) Erectophile

(m_r, m_n)	(1,1)	(2,1)	(3,1)	(1,2)	(1,3)
Mean	3.1E-03	2.5E-03	2.4E-03	1.5E-03	1.3E-03
Std. Dev.	3.5E-03	2.7E-03	2.6E-03	1.6E-03	1.6E-03
(m_r, m_n)	(2,2)	(3,2)	(2,3)	(3,3)	
Mean	6.6E-04	4.5E-04	1.0E-04	8.4E-05	
Std. Dev.	6.7E-04	5.8E-04	1.5E-04	1.2E-04	

3.7 Concluding Remarks

This study extends the previously derived soil isoline equations in the red–NIR subspace for the case of full canopy coverage. The parameter FVC was considered by employing the two-endmember LMM. Because the model used the FVC parameter explicitly in its formulation, we were able to derive the parametric form of the soil isoline equations using the FVC. The derivations proceeded by carefully noting the differences between the fully covered case and the partially covered case in the definitions of the isoline coefficients. I found that the FVC parameter contributed to the coefficients of the second- and higher-order terms for both the red and NIR bands, indicating that the FVC parameter only influenced the higher-order terms.

These findings influenced the derivation of the four approximated cases defined over a range of truncation orders in the red and NIR reflectances. The validity of the derived expression was investigated by conducting a series of numerical experiments using PROSAIL. The numerical results revealed that the errors in the approximated isolines were reduced as the truncation order increased. These results clearly indicated that the isoline equations could be improved by accounting for the FVC parameter explicitly. Further validation efforts are needed to demonstrate the utility of this isoline model in analyzing satellite imagery. Such efforts will be considered in future work.

CHAPTER IV

The Relationship Between Ratio-based Two-band Spectral Vegetation Indices Measured at Multiple Sensors on a Parametric Representation of the Soil Isoline Equations

4.1 Introduction

Environmental studies often require data records spanning several decades of time intervals to validate a research hypothesis. Because the life span of an Earth observation satellite is generally about five years, long-term data records usually comprise multiple datasets acquired using several Earth observation satellites. Therefore, inter-sensor calibrations among the past, current, and future satellite sensors play an important role[16] in determining the quality of such data.

Limiting our discussion to an investigation of the relationships between the VI values of different sensors, one difficulty in this investigation involves the selection (and often identification) of a model that provides a set of reflectance spectra under any desirable conditions. In any investigation based on a numerical model, this selection depends simply on the parameter range covered by a model. On the other hand, the availability of analytical and convenient models is very limited. One possibility is to use the analytical relationship between two reflectances of different wavelengths, known as the isoline equations[29, 81–83]. The 'soil isoline equation' introduced in Chapter 2 is one such choice.

Soil isolines introduce several advantages into investigations of the VI relationships. One advantage to this approach is that it can clarify the influences of the pure soil reflectance spectrum on the inter-sensor VI relationship. Because the soil isoline is a set of reflectance spectra obtained from canopies with a constant soil content, any relationships along a soil isoline can be purely attributed to a specific soil spec-

trum. Another advantage is that the use of the isoline enables the derivation of the relationship between two VI values obtained from different sensors. Two VIs may be related directly by eliminating the reflectance variables from a system of equations. One such example has been introduced elsewhere[103]. Soil isolines are good candidate measures for examining sensor-to-sensor variability. The advantages of the soil isoline equations may provide a new perspective on the inter-sensor calibration of VIs to which this study contributes.

The purpose of this study is to clarify the influences of the soil reflectance spectrum on the biases that exist when two sensors capture the same target spectra at different wavelengths. To this end, I set three objectives: First, I derived a relationship between two VI values measured from different sensors based on the recently introduced soil isoline equations. Second, I validated the derived results using a radiative transfer model to describe the coupling between the vegetation canopy and leaf reflectance. The third objective was to identify the dependencies of the derived relationships on the soil reflectance spectra obtained using both analytical and numerical approaches.

The use of the soil isoline for the inter-calibration of VI data has been examined briefly in pilot studies[109, 120, 121], which indicated that the soil isoline equation may provide good insights into the inter-sensor spectral differences. This study attempts to further advance the derivation and numerical validation studies. The theoretical background will be explained in section 4.2. Next, we introduce the derivation steps conceptually without using any numerical models in section 4.3. Some practical considerations are provided in section 4.4. The results of numerical experiments are presented in sections 4.5, 4.6 and 4.7. Finally, the discussion and conclusions summarize the findings in sections 4.8 and 4.9, respectively.

4.2 Background

4.2.1 Soil Isoline Equation in the Red-NIR Reflectance Subspace

A soil isoline is defined as a set of reflectance spectra, primarily in the red and near-infra red (NIR) reflectance subspaces, obtained by assuming fixed soil surface conditions beneath a vegetation canopy. Such isolines may be simulated using a radiative transfer model of the vegetation canopy, e.g., PROSAIL[96, 97, 99]. The conditions assumed during the simulation comprise a fixed soil spectrum that creates a set of spectra considered to be an isoline. Soil isoline equations comprise a system of equations that describe the relationship between the red and NIR reflectances, along with a soil isoline[107, 119]. A formal derivation of the soil isoline has been described in Chapter 2. Below, I simply summarize the derived isoline equation.

The isoline derivation requires a soil line[93], which is a well-established concept. A soil line is essentially a zero-vegetation isoline and is often represented using a linear form of the relationship between the red (R_{sr}) and NIR reflectances (R_{sn}) of the soil surface,

$$R_{sn} = s_0 + s_1 R_{sr}, \tag{4.1}$$

where s_1 and s_0 are the slope and offset, respectively.

Following the derivation steps described in Chapter 2, the form of the soil isoline that includes a common parameter ρ'_n becomes

$$\rho_r = f_r(\rho'_n) = \sum_{i=0}^{\infty} \alpha_i \rho'^i_n, \tag{4.2}$$

$$\rho_n = f_n(\rho'_n) = \sum_{i=0}^{\infty} \beta_i \rho'^i_n, \tag{4.3}$$

where

$$\alpha_i = \cos(\theta) p_i - \sin(\theta)\delta_{1i}, \tag{4.4}$$

$$\beta_i = \sin(\theta) p_i + \cos(\theta)\delta_{1i} + s_0\delta_{0i}, \tag{4.5}$$

with the Kronecker delta δ and the following definition of the angle corresponding to the slope of the soil line s_1,

$$\theta = \arctan(s_1). \tag{4.6}$$

Note that the coefficients p_i were obtained from a series of numerical simulations carried out using canopy radiative transfer models. The p_i values depended only on the soil surface reflectance. Because the red and NIR reflectances of the soil surface assumed during the derivation and numerical simulation could be described by the soil line represented in Eq. (4.1), the only parameters that characterized the p_i values were R_{sr} or R_{sn} in this study.

The derivation of the inter-sensor VI relationships introduced in this study depended on the parameter ρ'_n. Although ρ'_n is simply a common parameter in the soil isoline equations, Eqs. (4.2) and (4.3), it actually derives its meaning in the derivation of the soil isoline equations, as clearly explained in Chapter 2. The definition of ρ'_n is equivalent to the difference VI (DVI) [30] or, more rigorously, to the weighted DVI (WDVI), fully accounting for the soil line slope and offset[122].

4.2.2 A General Form of the VI Model

A general form of the VI equation was employed in this study to cover a variety of ratio-based two-band VI models. I employed a form expressed as the ratio of two linear sums of the red and NIR bands with a constant term. This form could be expressed by

$$v = F(\boldsymbol{P}, \boldsymbol{\rho}) = P_0 \frac{P_1\rho_r + P_2\rho_n + P_3}{P_4\rho_r + P_5\rho_n + P_6}, \tag{4.7}$$

where v represents a VI value, and a vector $\boldsymbol{P}$ is composed of a set of coefficients P_0 through P_6. The coefficients P_i were determined by the specific choice of VI, such as the NDVI; hence, these values characterized the performances of the VIs. The derivation of the inter-sensor VI relationships was introduced based on this general form. Although this form could not cover all two-band VIs, some of the ratio-based two-band VIs could be represented by choosing the coefficients P_i. Several examples of well-known VIs are summarized in Table 4.1.

Table 4.1: The seven coefficients provide a generalized form of the ratio-based two-band VIs.

v	P_0	P_1	P_2	P_3	P_4	P_5	P_6
NDVI	1	−1	1	0	1	1	0
SAVI	1.5	−1	1	0	1	1	0.5
EVI2	1.5	−1	1	0	2.4	1	1

4.3 Derivation Steps for Obtaining the Inter-sensor VI Relationships

This section symbolically describes the derivation steps applied to obtain the inter-sensor VI relationships based on the soil isoline equations. The derivation involved the non-unique choice of variables and relationships and the consideration of several terms in the derivations of individual cases. A variety of choices during the derivation can decrease the clarity of the model. These choices may be avoided by implementing the symbolic form introduced in this section.

This study assumed that the sensor differences were attributed only to the wavelengths during the derivation and numerical simulations. My intention was to eliminate the influences of the spatial resolution, the viewing and illumination geometries and so on, from the influences of the sampling wavelength.

The first step of the derivation involved the elimination of one of the two reflectances. This step assumed that an inter-sensor VI relationship could be obtained from each soil isoline. In other words, I attempted to characterize the relationship along a soil isoline. This approach enabled us to use the relationship between the red and NIR reflectances expressed by Eqs. (4.2) and (4.3). This first step is explained in the following subsection.

4.3.1 Relationship Between the Vegetation Indices and ρ'_n

In this subsection, I derived the VI along with a single soil isoline as a function of the common parameter ρ'_n. This derivation could be performed simply by substituting the soil isoline equations, Eqs. (4.2) and (4.3), into the red and NIR reflectances of the general form of the VI model equation, Eq. (4.7). As a result, Eq. (4.7) became

$$v = F_v(\boldsymbol{P}, \rho'_n) = P_0 \frac{P_1 f_r(\rho'_n) + P_2 f_n(\rho'_n) + P_3}{P_4 f_r(\rho'_n) + P_5 f_n(\rho'_n) + P_6}. \tag{4.8}$$

4.3.2 Symbolic Form of the Inter-sensor VI Relationship

In this subsection, I explicitly differentiated two sensors, denoted sensor-A and sensor-B. The VI model equation, Eq. (4.8), was applied to two sensors, indicated by the subscripts a and b throughout this chapter. Two definitions of the VI model equations were used here:

$$v_a = F_{va}(\rho'_{na}), \tag{4.9}$$

$$v_b = F_{vb}(\rho'_{nb}), \tag{4.10}$$

where the vector $\boldsymbol{P}$ is omitted for brevity.

The goal of this study was to directly relate v_a and v_b, defined by Eqs. (4.9) and (4.10). To this end, we required one condition in addition to Eqs. (4.9) and (4.10). From a physical point of view, the required relationship related the variables of the two sensors. The choice of condition was the relationship between the index-like parameters of sensor-A (ρ'_{na}) and sensor-B (ρ'_{nb}), represented by

$$\rho'_{nb} = f_{ab}(\rho'_{na}). \tag{4.11}$$

Since the WDVI-like parameter (ρ'_n) was used to bridge two-sensor's output, the following derivation targeted the ratio-based two-band VI.

In summary, three relationships, Eqs. (4.9), (4.10), and (4.11), were the key to the derivation of the relationship between v_a and v_b.

Equation (4.9) was solved for v_a symbolically,

$$\rho'_{na} \quad = \quad F_{va}^{-1}(v_a). \tag{4.12}$$

The relationship between v_a and v_b was given by

$$v_b = F_{vb} \circ f_{ab} \circ F_{va}^{-1}(v_a), \tag{4.13}$$

where the circle '$\circ$' represents composition of functions. Equation (4.13) describes the relationship between v_a and v_b, which is one objective of this study. This form may be further modified to relate v_b to the spectrum of the original sensor $\boldsymbol{\rho_a}$ by inserting Eq. (4.7) into Eq. (4.13),

$$v_b = F_{vb} \circ f_{ab} \circ F_{va}^{-1} \circ F(\boldsymbol{\rho_a}). \tag{4.14}$$

Note that Eq. (4.14) directly related the reflectance spectrum of the original sensor ($\boldsymbol{\rho_a}$) to a VI value of the destination sensor (v_b), which enabled us to understand the derivation steps. These derivation steps are summarized in the flowchart shown in Fig. 4.1.

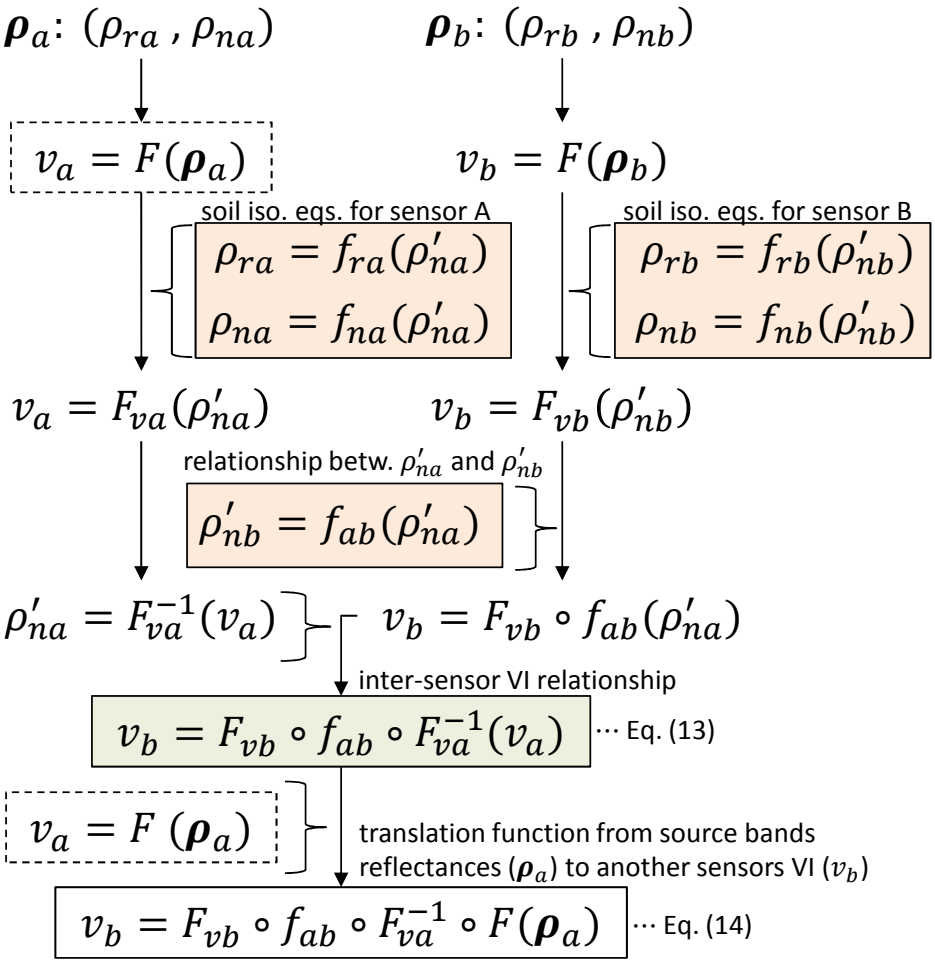

Figure 4.1: Flowchart describing the derivation steps used to obtain the inter-sensor VI relationships based on the soil isoline equations.

4.4 Practical Considerations for the Inter-sensor VI Relationship

The derivation explained symbolically in the previous section involves the inversion of one of the functions, F_{va}. Thus, the analytical approach is restricted by the choice of function in practical applications. Specifically, although F_{va} could be approximated using a geometric series, the order of the polynomial was limited to a small number. Practical considerations were addressed to ensure model accuracy while limiting the order of the polynomial to relatively low values, preferably, to first-order polynomials. This section addresses several points that should be treated carefully for practical applications.

4.4.1 Treatment of Higher-order Terms

Equation (4.8) involves a rational function of two polynomials of the parameter ρ'_n. The explicit form of Eq. (4.8) is

$$v = P_0 \frac{\sum_{i=0}^{\infty} A_i \rho_n'^i}{\sum_{i=0}^{\infty} B_i \rho_n'^i}, \tag{4.15}$$

where

$$A_i = P_1\alpha_i + P_2\beta_i + P_3\delta_{0i}, \tag{4.16}$$

$$B_i = P_4\alpha_i + P_5\beta_i + P_6\delta_{0i}. \tag{4.17}$$

The derivation proceeded while retaining the contributions of the higher-order terms by including the second- and higher-order terms in the zeroth-order term, thereby enabling the inversion process at the same time,

$$v = F_v(\rho'_n) = P_0 \frac{A'_0 + A_1\rho'_n}{B'_0 + B_1\rho'_n}, \tag{4.18}$$

where

$$A'_0 = A_0 + \sum_{i=2}^{\infty} A_i \rho_n'^i, \tag{4.19}$$

$$B'_0 = B_0 + \sum_{i=2}^{\infty} B_i \rho_n'^i. \tag{4.20}$$

Note that the second- and higher-order terms included in the zeroth-order term could be computed numerically for the original sensor (sensor-A) from the physical definition of the index-like parameter ρ'_n, which is clearly discussed in Chapter 2,

$$\rho'_n = -\sin(\theta)\rho_r + \cos(\theta)(\rho_n - s_0). \tag{4.21}$$

Furthermore, the value of ρ'_n obtained from the destination sensor, ρ'_{nb}, could be estimated from the known variable ρ'_{na} based on the relationship between ρ'_{na} and ρ'_{nb}, as represented by the function f_{ab} of Eq. (4.11).

Equation (4.18) is applicable to both sensor-A and sensor-B; however, the coefficients represented by the As and Bs were unique to each sensor because both coefficients were actually functions of the coefficients p_i and, hence, the values of α_i and β_i in the soil isoline equations, Eqs. (4.2) and (4.3). Therefore, Eq. (4.18) should be distinct from the equation obtained from the other sensors, as achieved using the subscripts a and b for sensor-A and sensor-B, respectively. We now have

$$v_a = F_{va}(\rho'_{na}) = P_0 \frac{A'_{0a} + A_{1a}\rho'_{na}}{B'_{0a} + B_{1a}\rho'_{na}}, \tag{4.22}$$

$$v_b = F_{vb}(\rho'_{nb}) = P_0 \frac{A'_{0b} + A_{1b}\rho'_{nb}}{B'_{0b} + B_{1b}\rho'_{nb}}. \tag{4.23}$$

The inverse of F_{va} may be simply defined by solving Eq. (4.22) for ρ'_{na},

$$\rho'_{na} = F_{va}^{-1}(v_a) = \frac{-B'_{0a}v_a + P_0 A'_{0a}}{B_{1a}v_a - P_0 A_{1a}}. \tag{4.24}$$

This function will be used later in this section. Note that the coefficients A'_{0a} and B'_{0a} are not really constants. They depend on the index-like parameter ρ'_{na} and, thus, vary with the reflectance spectrum of sensor-A. Also note that the reflectance of sensor-A is available prior to the translation process since it is defined as the original sensor. Thus, this inversion process does not deteriorate the measurement accuracy by computing ρ'_{na} from $\boldsymbol{\rho_a}$ for each pixel to adjust the coefficients A'_{0a} and B'_{0a} during the numerical algorithm.

4.4.2 Inter-sensor Relationship Between the Index-like Parameters

The next focus of this work is the relationship between ρ'_{na} and ρ'_{nb}, represented by the function f_{ab}. In this study, the relationship was approximated by a polynomial,

$$\rho'_{nb} = f_{ab}(\rho'_{na}) = \sum_{i=0}^{\infty} u_i \rho'^i_{na}. \tag{4.25}$$

Recall that the relationship between the red and NIR reflectance spectra measured by a specific sensor may be approximated by a soil isoline equation for a soil spectrum that remains constant throughout the numerical simulations. The coefficients of Eq. (4.25) depend on the soil spectrum, because ρ'_n is defined along with a soil isoline whose coefficients show variation with the changes of soil spectrum. This analogy suggests that the accuracy of Eq. (4.25) may be improved by expressing the coefficients as functions of the soil spectrum. Given the practicalities of the numerical treatment, the derivation was carried out by approximating a linear relationship,

$$\rho'_{nb} \approx u_0 + u_1 \rho'_{na}. \tag{4.26}$$

This point must be investigated thoroughly in a separate study.

4.4.3 Approximation of Eq. (4.23)

Equation (4.23) includes the higher-order terms of ρ'_{nb}, which is a common parameter that describes the destination sensor (sensor-B),

$$A'_{0b} = A_{0b} + \sum_{i=2}^{\infty} A_{ib} \rho'^i_{nb}, \tag{4.27}$$

$$B'_{0b} = B_{0b} + \sum_{i=2}^{\infty} B_{ib} \rho'^i_{nb}. \tag{4.28}$$

Note that the parameter ρ'_{nb} depends on the reflectance of the destination sensor. Thus, it cannot be estimated directly from the known reflectance spectrum (of the original sensor, $\boldsymbol{\rho_a}$); however, as explained briefly above, ρ'_{nb} may be estimated from the function f_{ab}. As a result, Eqs. (4.27) and (4.28) become

$$\hat{A}'_{0b} = A_{0b} + \sum_{i=2}^{\infty} A_{ib} [f_{ab}(\rho'_{na})]^i, \tag{4.29}$$

$$\hat{B}'_{0b} = B_{0b} + \sum_{i=2}^{\infty} B_{ib} [f_{ab}(\rho'_{na})]^i. \tag{4.30}$$

The function f_{ab} was approximated using Equation (4.26) to yield

$$\hat{A}'_{0b} = A_{0b} + \sum_{i=2}^{\infty} G_{ib}\rho'^{i}_{na}, \tag{4.31}$$

$$\hat{B}'_{0b} = B_{0b} + \sum_{i=2}^{\infty} H_{ib}\rho'^{i}_{na}, \tag{4.32}$$

where

$$G_{ib} = u_1^i \sum_{k=i}^{\infty} {}_kC_i u_0^{k-i} A_{kb}, \tag{4.33}$$

$$H_{ib} = u_1^i \sum_{k=i}^{\infty} {}_kC_i u_0^{k-i} B_{kb}. \tag{4.34}$$

As a result, Eq. (4.23) becomes

$$v_b = F'_{vb}(\rho'_{nb}) = P_0 \frac{\hat{A}'_{0b} + A_{1b}\rho'_{nb}}{\hat{B}'_{0b} + B_{1b}\rho'_{nb}}. \tag{4.35}$$

Equation (4.26) was applied to the first-order terms of both the denominator and the numerator on the right-hand side of Eq. (4.35) to yield

$$v_b = F'_{vb} \circ f_{ab}(\rho'_{na}), \tag{4.36}$$

$$= P_0 \frac{X + A_{1b}u_1\rho'_{na}}{Y + B_{1b}u_1\rho'_{na}}, \tag{4.37}$$

where

$$X = \hat{A}'_{0b} + A_{1b}u_0, \tag{4.38}$$

$$Y = \hat{B}'_{0b} + B_{1b}u_0. \tag{4.39}$$

4.4.4 Inter-sensor VI Relationship

Equations (4.37) and (4.24), along with v_a and v_b, may be related by

$$v_b = F'_{vb} \circ f_{ab} \circ F^{-1}_{va}(v_a), \tag{4.40}$$

$$= P_0 \frac{c_1 v_a - P_0 c_0}{d_1 v_a - P_0 d_0}, \tag{4.41}$$

where

$$
\begin{aligned}
c_1 &= B_{1a}X - u_1 B'_{0a} A_{1b}, && (4.42)\\
c_0 &= A_{1a}X - u_1 A'_{0a} A_{1b}, && (4.43)\\
d_1 &= B_{1a}Y - u_1 B'_{0a} B_{1b}, && (4.44)\\
d_0 &= A_{1a}Y - u_1 A'_{0a} B_{1b}. && (4.45)
\end{aligned}
$$

Equation (4.41) shows that a linear relationship between the index-like parameters does not guarantee a linear relationship between the two VIs whose model equation is defined as a rational function.

The variables defined by Eqs. (4.42) through (4.45) may be re-written using ρ'_{na} explicitly according to

$$
\begin{aligned}
c_1 &= \psi(\boldsymbol{A}_b, \boldsymbol{B}_a) + \psi'(\boldsymbol{A}_b, \boldsymbol{B}_a, \rho'_{na}), && (4.46)\\
c_0 &= \psi(\boldsymbol{A}_b, \boldsymbol{A}_a) + \psi'(\boldsymbol{A}_b, \boldsymbol{A}_a, \rho'_{na}), && (4.47)\\
d_1 &= \psi(\boldsymbol{B}_b, \boldsymbol{B}_a) + \psi'(\boldsymbol{B}_b, \boldsymbol{B}_a, \rho'_{na}), && (4.48)\\
d_0 &= \psi(\boldsymbol{B}_b, \boldsymbol{A}_a) + \psi'(\boldsymbol{B}_b, \boldsymbol{A}_a, \rho'_{na}), && (4.49)
\end{aligned}
$$

where

$$
\begin{aligned}
\boldsymbol{A}_s &= (A_{0s}, A_{1s}, A_{2s}, \cdots), && (4.50)\\
\boldsymbol{B}_s &= (B_{0s}, B_{1s}, B_{2s}, \cdots), && (4.51)\\
\psi(\boldsymbol{\mu}, \boldsymbol{\nu}) &= \nu_1(\mu_0 + u_0\mu_1) - u_1\nu_0\mu_1, && (4.52)\\
\psi'(\boldsymbol{\mu}, \boldsymbol{\nu}, \rho'_{na}) &= \sum_{i=2}^{\infty} \left[u_1^i \nu_1 \left(\sum_{k=i}^{\infty} {}_kC_i u_0^{k-i} \mu_k \right) - u_1 \nu_i \mu_1 \right] \rho'^i_{na}. && (4.53)
\end{aligned}
$$

The end of this section treats a special approximation case, in which all of the second- and higher-order terms are truncated at ρ'_n in the soil isoline equations, Eqs. (4.2) and (4.3). In such a case, the index-like parameter ρ'_{na} is no longer included in the coefficients of the inter-sensor VI relationship Eq. (4.41). In such a dramatic scenario, Eq. (4.41) may be reduced to the following form

$$
\hat{v}_b = P_0 \frac{\psi(\boldsymbol{A}_b, \boldsymbol{B}_a) v_a - P_0 \psi(\boldsymbol{A}_b, \boldsymbol{A}_a)}{\psi(\boldsymbol{B}_b, \boldsymbol{B}_a) v_a - P_0 \psi(\boldsymbol{B}_b, \boldsymbol{A}_a)}, \tag{4.54}
$$

where all four coefficients expressed by a function ψ are fully independent of ρ'_{na}.

4.5 Results of the Numerical Simulation and Discussion

This section demonstrates the validity of the relationships derived and introduced in this study. All uncertainties associated with the spectral acquisition were eliminated by applying the framework to a data set calculated numerically using radiative transfer (RT) models of the vegetation canopy and leaf layers. The validity of the derived relationships was then investigated by comparing the VI values of the two sensors to the VI values translated from the other sensor. The translation from the VI value of one sensor to the value of the other sensor was performed by applying the relationship derived using the coefficients computed from the coefficients of the soil isolines. The following subsections describe the numerical simulation conditions (parameter settings) and obtained results.

4.5.1 Numerical Simulations of the Inter-VI Relationships

A combined leaf and canopy RT model, PROSAIL, was employed to simulate the top-of-the-canopy (TOC) reflectance spectra under a variety of conditions. The numerically obtained TOC reflectance spectra were then used to simulate the band reflectances of four hypothetical sensors by selecting different pairs of wavelengths as the red and NIR bands (shown below). One of the four sensors was assigned as the 'original' sensor (sensor-A), the VI values of which were translated into the values of the other three sensors (sensor-B), denoted as the 'destination' sensors during the derivation.

The numerical simulations were conducted by selecting three different parameters to characterize the VI differences. The first parameter was the leaf area index (LAI), a representative biophysical parameter. The value of the LAI varied from 0 to 4.0 at 0.5 intervals. The second parameter was the soil reflectance spectrum, which can significantly disrupt the VI values. The soil reflectance spectra were obtained by linearly combining the wet and dry soil spectra calculated in the PROSAIL model. The third parameter was the wavelength, which introduced differences in the band reflectances measured by the different sensors; thereby producing differences in the VI values as well. The other parameters in the leaf model PROSPECT and the canopy model SAIL were held constant during the experiments.

The parameters that characterized the leaf chemical content in the PROSPECT model were fixed at the standard (average) values. The leaf angle distribution, an input of the SAIL model, was fixed at a spherical distribution. Under these assumptions, the LAI was the only parameter of biophysical properties in this study.

The band center wavelengths of the four hypothetical sensors were set to values

equal to the band center wavelengths of the GOSAT-CAI, LANDSAT8-OLI, Suomi NPP-VIIRS, and TERRA-MODIS. The wavelength pairs of the red ρ_r and NIR bands ρ_n of the four hypothetical sensors were (ρ_r, ρ_n)=(674, 870), for sensor-A, (655, 865) for sensor-B1, (672, 865) for sensor-B2, and (645, 869) for sensor-B3 in [nm]. Figure 4.2 shows the reflectance spectra and soil isolines retrieved from sensor-A in the red and NIR reflectance space. The figure shows good agreement among the retrieved soil isolines, which will be used to translate the VI values. The detailed steps used to obtain the soil isoline retrievals are described in Chapter 3.

The translation of the VI values from one sensor to another sensor was performed by regarding the CAI-like sensor (sensor-A) as the original sensor, and the other three sensors (sensor-B1, B2, and B3) were the destination sensors. I considered three translation cases from sensor-A (original) to sensors-B1, -B2, and -B3 (destinations). I labeled these three pairs of sensors as translation Case-1, Case-2, and Case-3, respectively. Again, the translation process involved translating a set of reflectance spectra (of the two bands) from sensor-A (CAI-like sensor); the VI values were then translated into sensor-B1 (case1), sensor-B2 (Case-2), and sensor-B3 (Case-3). The VI translation was performed in all cases simply by using the derived VI relationships. The validity of the derived relationship was then evaluated based on a comparison between the simulated VIs obtained from sensor-B and the translated VIs obtained from sensor-A.

4.5.2 Dependence of the Coefficients ψ on the Soil Reflectance

The first step in the numerical experiments involved clarifying that the coefficients of the derived expressions depended on the variations in the soil reflectance spectra $\boldsymbol{R}_s$. Recall that the inter-sensor VI relationships, as described by Eq. (4.41), were derived for a constant soil type due to the use of the soil isoline equation. The relationship, therefore, varied as the soil reflectance spectrum changed. This characteristic of the system is fundamental to this study.

The numerical experiments were conducted by first obtaining the coefficients of Eq. (4.41) from the coefficients of the soil isolines. The algorithms and procedures applied to the numerical retrievals of the soil isolines have been described in Chapter 3. The results of the first-order polynomial approximation of the NDVI provided a representative approximation scenario in the numerical experiments. This subsection investigated the variations in the four coefficients of Eq. (4.54) for $P_0 = 1$, based on the definitions of the NDVI. Figure 4.3 shows the plots of the four coefficients in Eq. (4.54) for Case-1 (translation from the VI of sensor-A (CAI-like sensor) to sensor-B1 (OLI-like sensor)), to represent the three sensor combinations. Note that the X-axis

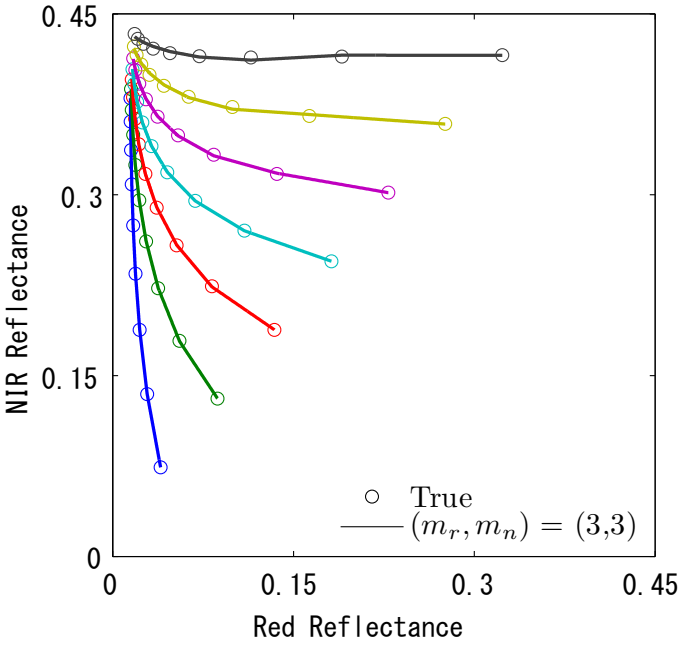

Figure 4.2: Plots of the soil isolines (lines) represented by Eqs. (4.2) and (4.3), and numerically simulated reflectance spectra (circles) in the red and NIR reflectance space. The soil isoline was truncated at the third-order term. The reflectance spectra obtained at a constant soil brightness were denoted by the same color.

in the figure is the soil reflectance of the red band for sensor-A. (The NIR reflectance of the soil spectrum was computed from the red reflectance using the assumed soil line, Eq. (4.1)).

As shown in the figure, all four coefficients varied linearly with the soil red reflectance. These results indicated that the inter-sensor VI relationship depended on the soil reflectance beneath the canopy layer, a representative parameter of the land surface conditions. The implication of these results are serious (and important): The regression coefficients determined without accounting for the variations in the soil spectrum could suffer from the variations in the soil spectrum in a simple polynomial model of the inter-sensor VI relationship.

4.5.3 Accuracy and Applicability of the Derived Translation Function

The validity of the derived relationships were evaluated by comparing the VI values of the two sensors before and after the translation. The VI value translated from sensor-A to sensor-B was denoted by $\hat{v}_b$ which was computed according to Eq.

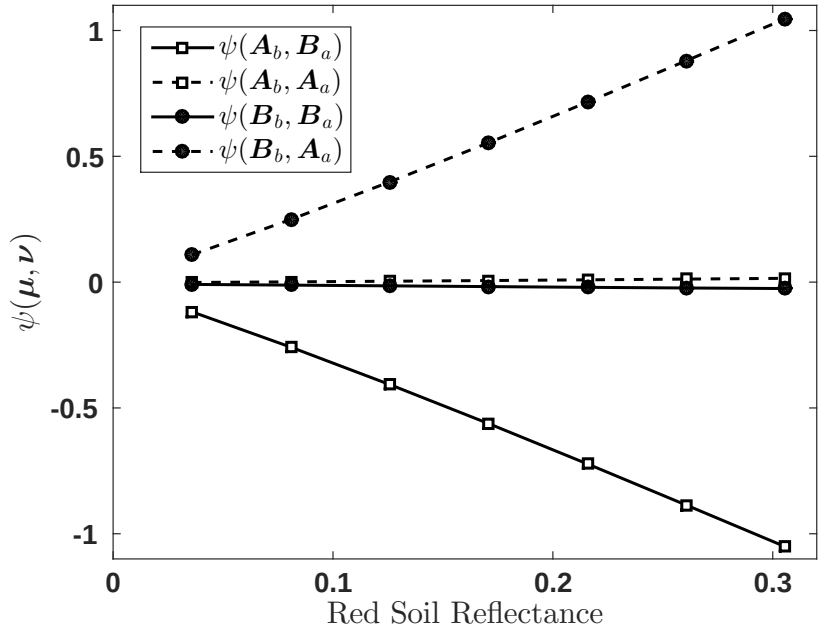

Figure 4.3: Plots of the four coefficients represented by ψ in Eq. (4.54) for NDVI under Case-1 conditions (translation from sensor-A to sensor-B1).

(4.41). The aim of this section is to validate the derived expressions by confirming the accuracy improvement of v_b after the translation from v_a (hence $\hat{v}_b$). The comparison between $(v_a - v_b)$ and $(\hat{v}_b - v_b)$ was facilitated by representing the differences as ε and $\hat{\varepsilon}$, respectively, such as

$$\varepsilon = v_a - v_b, \tag{4.55}$$

$$\hat{\varepsilon} = \hat{v}_b - v_b, \tag{4.56}$$

where v_a is the VI value of the CAI-like sensor-A, and v_b represents the VI value obtained from the destination sensors, namely, OLI-like sensor-B1, VIIRS-like sensor-B2, or MODIS-like sensor-B3. The values of ε and $\hat{\varepsilon}$ were positive if the VI values measured using the original sensor (v_a) and the values obtained from the translated VI values ($\hat{v_b}$) exceeded v_b. The latter case also indicated that translation by Eq. (4.41) overestimated the value of the destination sensor.

Figure 4.4 shows plots of ε and $\hat{\varepsilon}$ for NDVI as a function of an LAI characterized by one of two different soil spectra (wet or dry conditions). The calculated values of ε and $\hat{\varepsilon}$ are indicated by the dotted and solid lines, respectively. In the figure, ε and $\hat{\varepsilon}$ are labeled by the legends 'before' and 'after,' respectively. The differences

between the soil reflectance spectra of the wet and dry soils are represented by the filled circle and the empty square, respectively. The upper three plots correspond to Case-1 (CAI vs. OLI) and retain terms up to the first-, second-, or third-order terms of a polynomial in the soil isoline equations. The middle and bottom rows of the figure show the results obtained from Case-2 (CAI vs. VIIRS) and Case-3 (CAI vs. MODIS), respectively.

This figure clearly shows that the translation error $\hat{\varepsilon}$ (solid line) was smaller than the original differences ε (dotted line) across nearly the entire LAI range in all cases. This fact clearly validates the expression derived in this study.

Overall, the original difference ε was larger for the bare soil (LAI=0) in this simulation. Although the differences decreased significantly after applying the translation $\hat{\varepsilon}$, the translation error in this LAI range (LAI was nearly zero) was relatively larger than the values measured in the middle to higher LAI ranges. These results indicated that the relationship derived in this study should be improved along the soil line (base line). Additionally, special treatment may be needed to reduce the translation errors at low-vegetation pixels.

A comparison of the results obtained from using polynomials of different orders in the soil isoline approximations revealed that the first-order approximation translation results (the plots shown in the left column) were almost as good as the second-order results (the middle column) and the third-order results (the right column). These properties were somewhat surprising; we had expected that the use of higher-order polynomials would improve the model accuracy. The lack of improvement most likely resulted the fact that the relationship between ρ'_{na} and ρ'_{nb} was approximated by a first-order polynomial. Two factors influenced the accuracy of the translation results. First, the order of the polynomials (truncation) used for the soil isoline equation, and second, the approximation of the relationship between the index-like parameters (ρ'_{na}) of sensor-A and that of sensor-B (ρ'_{nb}). In Chapter 3, we confirmed that the accuracy of the soil isoline equation increased as the polynomial order increased. The polynomial order of the soil isoline may not determine the accuracy under the conditions applied in the present case.

The use of a higher-order polynomial to describe the relationship between ρ'_{na} and ρ'_{nb} is expected to improve the translation accuracy; however, this step is impractical. The analytical form of a relationship described by a second-order polynomial would be more complicated than the current form, which undermines the practical utility of an analytical expression. This point requires further investigation in a separate study.

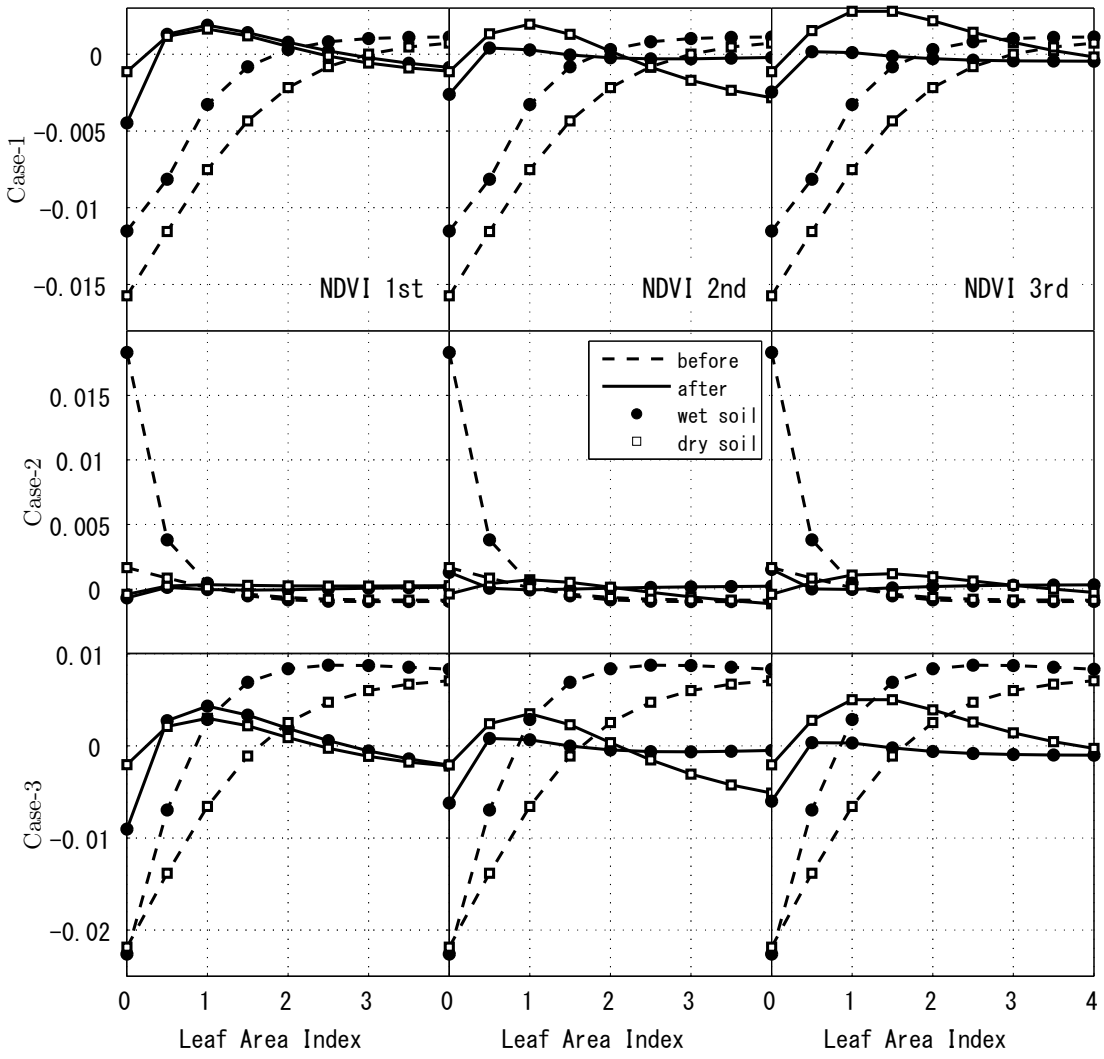

Figure 4.4: Plots of differences before (ε) and after translation ($\hat{\varepsilon}$) for the NDVI as a function of the LAI. The dotted lines represent the variables defined by Eq. (4.55), and the solid lines represent the variables defined by Eq. (4.56). Filled circles and empty squares denote the cases of the wet and dry soils, respectively. The results obtained from different orders of the truncation terms are organized in columns. From left to right, the columns present the results of the first-, second-, and third-order approximations. The results for the cases of three sensor pairs are presented across the rows.

The trends in the other VI models were investigated by creating similar plots for the SAVI and EVI2, as shown in Fig. 4.5. The trends were similar to those obtained using the NDVI, as observed in the SAVI soil isolines approximated using a first-order polynomial (left column) or a third-order polynomial (middle column). The right column plots the results obtained from the use of the EVI2 approximated using third-order soil isolines. Table 4.2 summarizes the mean absolute differences in the VI values ($|\hat{\varepsilon}|$) over the entire range of the LAI and soil brightness (from wet to dry conditions) normalized by the original difference ($|\varepsilon|$). Table 4.3 also summarizes the maximum differences of their absolute values normalized by the original difference. These results reveal that the original differences (ε) decreased significantly after the translation ($\hat{\varepsilon}$), thereby validating the derived expressions.

Finally, I examined land cover dependence on the derived inter-sensor VI relationships. Figure 4.6 shows the plots of MAD under various combinations of Chlorophyll content (from 20 to 60 μg/cm^2) and leaf angle distribution (Spherical, Planophile, Erectophile, and Uniform). The results indicate that the accuracy of the derived expressions varies with the biophysical parameters. It thus implies some extent of land cover dependence. Further comprehensive investigations will be needed to completely understand the land cover dependence on the derived relationships.

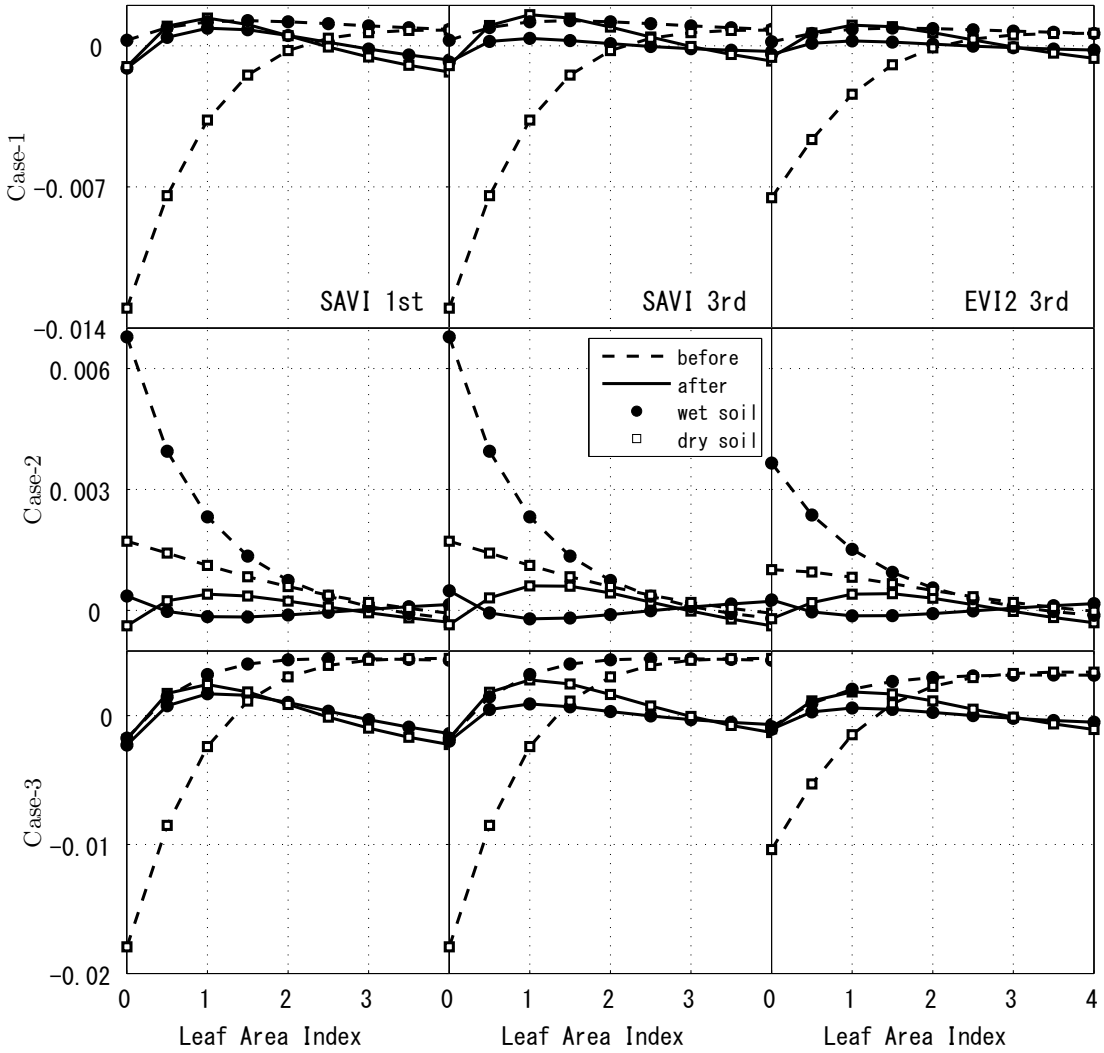

Figure 4.5: The plots presented in Figure 4.4 were calculated for the VIs: SAVI and EVI2. The left column presents the results of the SAVI calculated using a first-order term. The center and right columns present results of the SAVI and EVI2, respectively, calculated up to the third-order term. The influence of the truncation order for the SAVI was assessed by comparing the left and the center columns. The differences between the SAVI and EVI cases were assessed by comparing the center and right columns.

Table 4.2: Normalized mean absolute differences in the derived translation functions (in percent).

VI		Orders of soil isolines		
NDVI		1	2	3
	Case-1	25.6	28.0	24.6
	Case-2	11.7	18.9	19.0
	Case-3	25.8	26.7	23.6
SAVI		1	2	3
	Case-1	46.0	30.7	26.5
	Case-2	14.7	15.0	13.9
	Case-3	35.2	26.1	22.8
EVI2		1	2	3
	Case-1	50.0	33.2	28.2
	Case-2	15.6	15.9	14.5
	Case-3	35.9	26.5	22.9

Table 4.3: Normalized maximum absolute differences in the derived translation functions (in percent).

VI		Orders of soil isolines		
NDVI		1	2	3
	Case-1	28.4	19.7	17.8
	Case-2	5.1	7.0	8.2
	Case-3	40.0	27.5	26.6
SAVI		1	2	3
	Case-1	12.7	12.3	11.8
	Case-2	5.9	9.6	8.9
	Case-3	15.5	15.6	15.4
EVI2		1	2	3
	Case-1	16.8	16.1	13.5
	Case-2	7.7	13.5	11.3
	Case-3	20.0	20.3	17.6

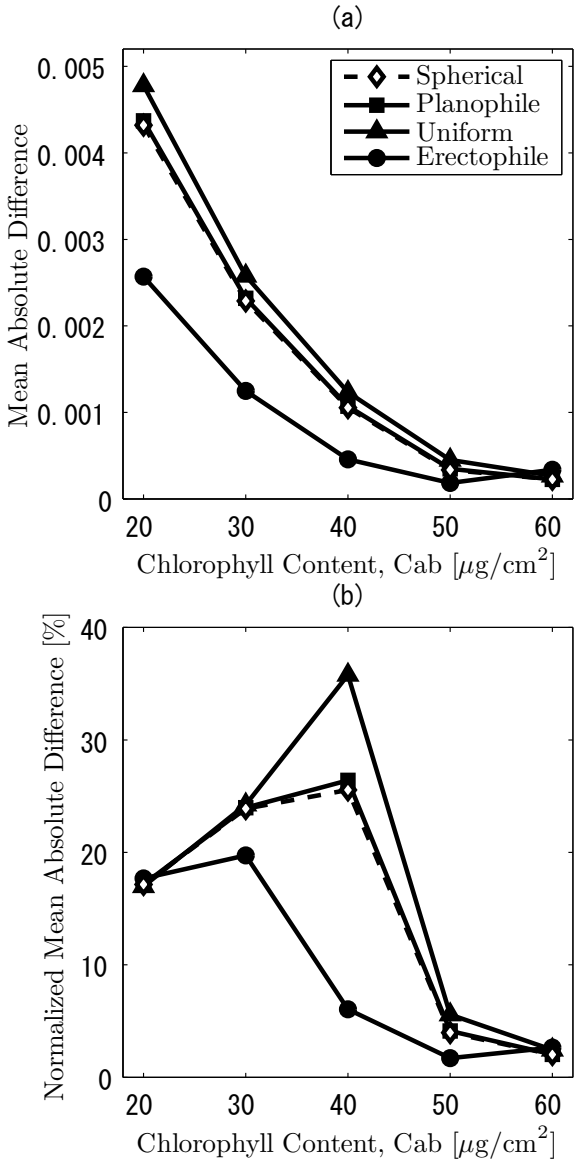

Figure 4.6: Plots of (a) the mean absolute difference (MAD) and (b) the MAD normalized by the original difference in percent by the translation function based on the first-order isoline equations Eq. (4.54) for NDVI under Case-1 conditions (translation from sensor-A to sensor-B1) as a function of chlorophyll content $C_{\rm ab}$. The dashed line with diamond marks represents (a) the MAD or (b) the normalized MAD under spherical leaf angle distribution (LAD), while solid lines with square, triangle and circle are those under planophile, uniform and erectophile LAD, respectively.

4.6 Numerical Evaluation of the Translation Accuracy

In the previous section, which described a study relating to spectral issues, the work demonstrated the potential for reducing biases caused from differences in the spectral bands of two sensors based on the derived VI-to-VI relationship. Although the translation by the inter-VI relationship significantly reduced bias, one question arose: Is the magnitude of the residual bias after bias reduction satisfactory for the intercalibration of actual satellite data? This study must identify theoretical limitations on the magnitude of the bias reduction before applying this technique to the intercalibration of actual observation records. This study attempted to address this concern by conducting both analytical and numerical simulations. Specifically, I derived the magnitude of bias errors analytically based on the senor-specific signal-to-nose ratio (SNR) reported in sensor specifications. I compared the predicted bias errors to the difference between the VI values of the two sensors after translation to minimize biases using the proposed technique.

4.6.1 Experimental Conditions

A well-known numerical model PROSAIL[99] was employed to simulate top-of-canopy reflectance spectra in which the values of the LAI and soil brightness model inputs varied. The center wavelength positions of the SRFs for the three sensors (GOSAT-CAI, Terra-MODIS, and Landsat8-OLI) were used to model the VIs from distinct sensors. In this study, CAI was defined as a sensor (sensor-a) used for observation (original sensor), whereas the other two were defined as the target sensor (sensor-b) to which the value of NDVI from sensor-a was adjusted. In other words, v_a from CAI was translated to $\hat{v}_b$ using Eq. 4.40. I then evaluated the translation error in terms of the mean absolute difference (MAD) of the VI difference ε and the mean absolute error (MAE) of the error after translation $\hat{\varepsilon}$ for wet and dry soils. The MAD and MAE in the case of the NDVI are summarized in Table 4.4. The table reveals that the MAE was smaller than MAD by a factor of three or four.

4.6.2 NDVI Uncertainty Propagated by the SNR

Finally, the MAE values were compared to the errors propagated from the SNR of the reflectance defined by $\frac{\sigma_v}{\rho_n}$ and $\frac{\sigma_v}{\rho_r}$. In the case of NDVI (Eq. (4.7)), the propagated error could be represented by

$$\sigma_v^2 = \left(\frac{\partial v}{\partial \rho_n}\right)^2 \sigma_n^2 + \left(\frac{\partial v}{\partial \rho_r}\right)^2 \sigma_r^2. \tag{4.57}$$

After some arrangements, the final form of Eq. (4.57) became

$$\sigma_v^2 = \frac{\mathrm{SNR}_n^{-2} + \mathrm{SNR}_r^{-2}}{2}(1 - v^2)^2, \tag{4.58}$$

where SNR_n and SNR_r are the signal-to-noise ratios of the NIR and red band of the destination sensors, respectively. Furthermore, I defined $\overline{\mathrm{SNR}}$ to simplify the propagated error,

$$\sigma_v = \frac{1 - v^2}{\overline{\mathrm{SNR}}}, \tag{4.59}$$

where

$$\overline{\mathrm{SNR}} = \left(\frac{\mathrm{SNR}_n^{-2} + \mathrm{SNR}_r^{-2}}{2}\right)^{-\frac{1}{2}}. \tag{4.60}$$

The SNRs of the OLI and MODIS sensors for the red ($\mathrm{SNR_r}$) and NIR ($\mathrm{SNR_n}$) bands, and their normalized SNR ($\overline{\mathrm{SNR}}$) are shown in Table 4.5.

4.6.3 Translation Error vs. SNR-based Uncertainty

Figure 4.7 shows a comparison between the MAE and σ_v for the two cases. The figure presents the OLI and MODIS results in red and blue colors, respectively. Dashed lines in the figure correspond to the intersection (v_{intrsect}) between the MAE and

Table 4.4: Mean absolute difference (MAD) of the NDVI difference ($v_b - v_a$) and mean absolute error (MAE) of the translation error ($v_b - \hat{v}_b$) for two soil types under wet and dry conditions.

sensor-a	sensor-b	soil	MAD	MAE
CAI	OLI	wet	3.1E-03	1.3E-03
		dry	4.8E-03	9.3E-04
CAI	MODIS	wet	9.1E-03	2.9E-03
		dry	7.8E-03	1.7E-03

Table 4.5: Signal-to-noise ratios (SNRs) of the instruments in sensor-b for the red (SNR_r) and NIR (SNR_n) bands, and normalized SNR ($\overline{\mathrm{SNR}}$).

sensor-b	SNR_r	SNR_n	$\overline{\mathrm{SNR}}$
OLI	340	460	386.67
MODIS	128	201	152.69

SNR-based uncertainties derived from Eq. (4.59) under the condition $\sigma_v = \mathrm{MAE}$, as

$$v_{\mathrm{intrsect}} = \sqrt{1 - \mathrm{MAE} \cdot \overline{\mathrm{SNR}}}. \tag{4.61}$$

Minimum and maximum values of v_{intrsect} are also shown in Fig. 4.7 The results showed that the translation error (reduced bias by the technique) was lower than the propagated error across most of the VI range, except at higher NDVI values (>0.7); however, the NDVI values between 0.7 and 0.8 displayed nearly equal uncertainties.

4.6.4 Remarks

This study compared the analytically derived error propagated from the sensor-specific SNR with a reduced bias using the proposing isoline-based intercalibration technique. Numerical simulation results confirmed that the VI intercalibration technique reduced the biases in the NDVI to the level of the VI errors propagated from the random errors specified by the reported SNR. The results indicate that this technique could reduce the magnitude of VI differences down to the level of the unavoidable random errors propagated from the sensor-specific SNR. Further studies are needed to confirm this analysis by applying the technique to actual satellite imageries.

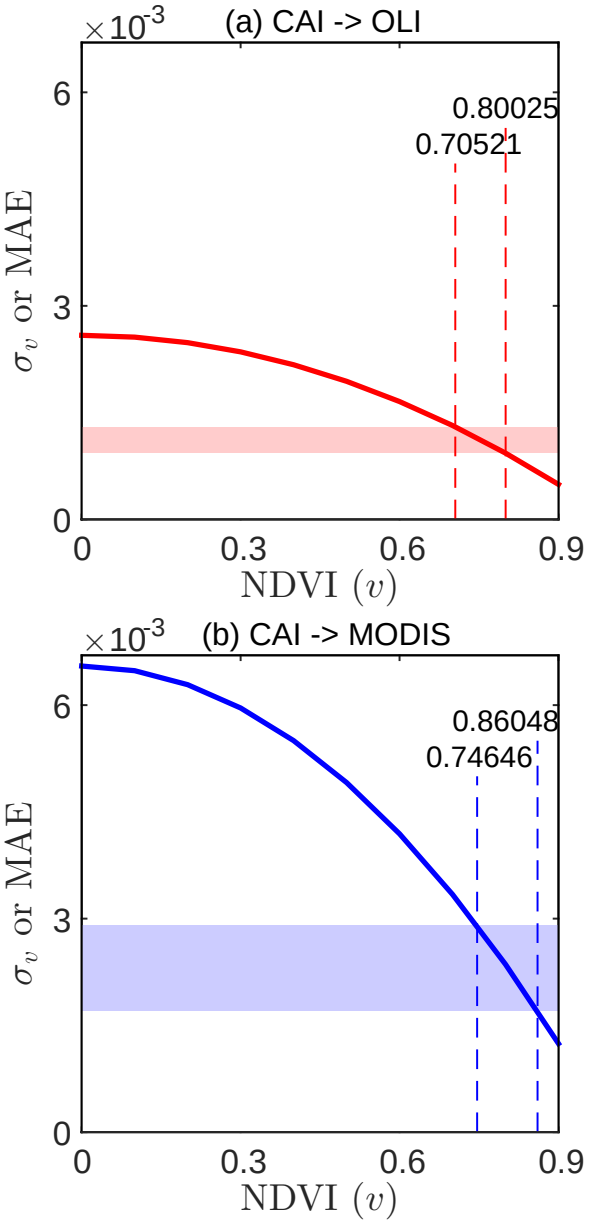

Figure 4.7: Plots of the error propagated from the signal-to-noise ratio (solid lines) and MAE (color area) for translation error $\hat{\varepsilon}$. The results obtained from the OLI and MODIS cases are represented by red and blue colors, respectively. The MAE ranges were reported in Table. 4.4. Dashed lines correspond to the intersection v_{intrsect}.

4.7 Investigation of Sources in Translation Errors

The present study assumed that the intersensor relationship between ρ'_{na} and ρ'_{nb} could be expressed as a first-order equation. This limitation revealed the derivation of the inter-VI relationship as a rational function with consideration for the soil brightness variations underneath the vegetation canopy; however, numerical experiment conducted using the PROSAIL model suggested that the accuracy of the intrasensor relationship, encompassed by the soil isoline equations in the red–NIR space, did not depend on the derived VI translation.

4.7.1 Translation Algorithm Using Three Mappings

The numerical results in Chapter 3 confirmed that the accuracy of the soil isoline equation increased as the polynomial order increased. Therefore, 'non-linearity' is expected to affect the VI translation accuracy. Here, I describe the effect of the order of the inter-ρ'_n relationship on the goodness of the VI translation. Translation was conducted simply using three mappings:

1. $F_{va}^{-1} : v_a \rightarrow \hat{\rho}'_{na}$
2. $f_{ab} : \hat{\rho}'_{na} \rightarrow \hat{\rho}'_{nb}$
3. $F_{vb} : \hat{\rho}'_{nb} \rightarrow \hat{v}_b$.

This algorithm is identical to the translation by their composite functions ($F_{vb} \circ f_{ab} \circ F_{va}^{-1} : v_a \rightarrow \hat{v}_b$).

4.7.2 Inversion of Soil Brightness

Recall that the approximated soil isoline equations include an extent error that is propagated to affect the accuracy of the inter-VI relationship; however, the approximated soil isoline equations estimated soil brightness levels that differed from the true soil brightness levels due to a lack of expressions for the isoline equations. This observation begs the question: Are the coefficients in the inter-VI relationship describing the true soil brightness R_s determined by the estimated soil brightness $\hat{R}_s$, and do these coefficients enhance translation accuracy?

Soil brightness is derived by solving the inverse problem of the isoline equations. The soil isoline could be searched using $\hat{R}_s$, corresponding to the simulated spectral points in the rotated subspace, and a simple optimization method that minimized a

cost function in a rotated reflectance subspace:

$$\hat{R}_s = \underset{R_s}{\operatorname{argmin}} |\rho'_r - \hat{\rho}'_r(R_s)|, \tag{4.62}$$

where $\hat{\rho}'_n(R_s)$ is the red reflectance predicted by a soil isoline equation in a rotated subspace (Eq. 2.11 with N-th order truncation),

$$\hat{\rho}'_r(R_s) = \sum_{i=0}^{N} p_i(R_s)\rho'^i_n, \tag{4.63}$$

where N is the order of the soil isoline equations.

Note that the order of soil isoline equations contributes two mappings, namely F^{-1}_{va} and F_{vb}. Whereas orders of inter-relationship between ρ'_a and ρ'_b contributed to the mapping f_{ab},

$$\hat{\rho}'_{nb}(R_s) = \sum_{j=0}^{M} u_i(R_s)\rho'^j_{na}, \tag{4.64}$$

where M is the order of the inter-sensor relationship for the translation function of v_a.

4.7.3 Results

Three mapping translation algorithms were used to investigate translation errors in CAI vs. MODIS (Case-1) using the PROSAIL simulator. A regression approach, which did not include soil brightness effects, was also applied.

$$\hat{v}^{\mathrm{reg}}_b = \sum_{j=0}^{M} u^{\mathrm{reg}}_j v^j_a \tag{4.65}$$

Here, $\hat{v}^{\mathrm{reg}}_b$ is the VI value estimated for sensor B using a regression method with coefficients u^{reg}, determined by the correspondence between the VI values for sensors-a and -b.

Figure 4.8 plots the overall (top) MAD and (bottom) STD for the translation errors. The results are shown as bar plots grouped by the regression and N-th soil isoline equations ($N = 1, 2, \cdots, 5$). The orderings of the intersensor relationships M ($N = 1, 2, \cdots, 6$) from left to right are set in each group. The bar without a face color indicates the true soil brightness results, whereas the gray bar indicates the estimated soil brightness results. Note that the colored bars agreed perfectly with

the un-colored bars using the regression method because the method did not consider soil brightness effects.

The MAD and STD values gradually decreased as the order of the intersensor relationship in ρ'_n increased, indicating that the accuracy of the soil isoline-based translation depended on ρ'_n. Interestingly, the second- and third-order soil isoline-based translations displayed enhanced accuracy in terms of the estimated soil brightness. These findings are important for implementing soil isoline-based translation algorithms.

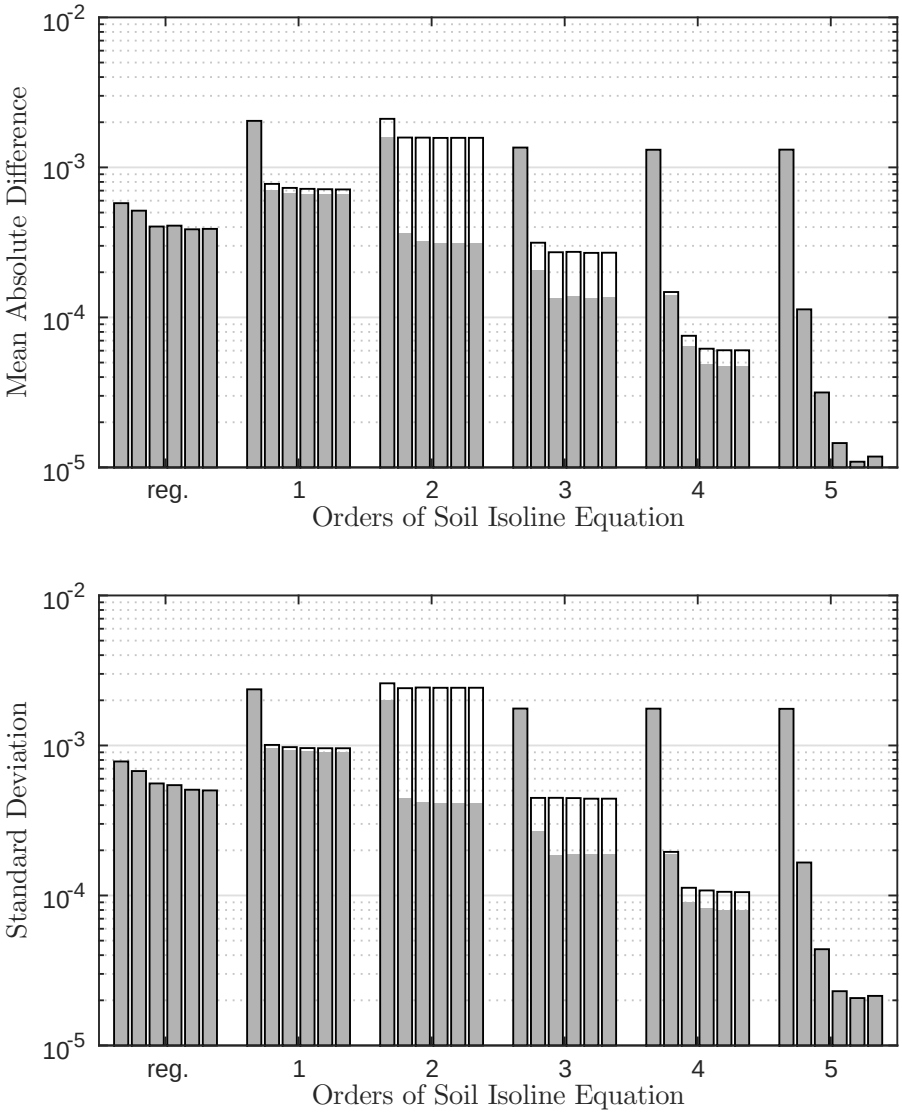

Figure 4.8: Overall (top) MAD and (bottom) STD values for the translation errors. The results are shown as bar plots grouped by regression and the N-th soil isoline equations ($N = 1, 2, \cdots, 5$). The order of the intersensor relationship M ($N = 1, 2, \cdots, 6$) is indicated from left to right in each group. The uncolored bars corresponded to the true soil brightness results, whereas the gray bars indicated the estimated soil brightness results.

4.8 Discussion

This study revealed that the inter-sensor VI relationship varied with the soil reflectance spectrum beneath the canopy layer. The mechanism by which this relationship varied could be inferred from the fact that the four coefficients of the inter-sensor VI relationship could all be expressed as functions of the soil reflectance spectrum. This analytical result revealed the following important facts: (1) a model of the inter-sensor VI relationship that does not address soil surface classification may retrieve a relationship that suffers from soil surface spectrum variations within a target regions; (2) the retrieved inter-sensor VI relationship across a region characterized by a specific soil spectrum cannot be directly applicable to other regions characterized by a different soil spectrum; (3) soil spectrum estimates must be made prior to inter-sensor calibration if the calibration relies on formulations similar to the expressions derived in this study.

An alternative approach to performing an inter-sensor calibration could rely on cross-calibrating similar bands, one by one, measured in two distinct sensors. This approach is by far the simplest, although it has several disadvantages. First, the number of bands that must be cross-calibrated is equal to the number of bands required by the algorithm employed. This approach can unfortunately be difficult for large numbers of bands. The cross-sensor band-to-band relationships can vary with the land surface conditions, depending on the canopy and soil spectrum. These dependencies present the major obstacles to this type of cross-calibration. Recall that inter-sensor calibration procedures are not equivalent to absolute calibration procedures due to differences in the band configurations (band center and width characterized by the spectral response functions). By contrast, the approach introduced in this study requires only the relationships between ρ'_{na} and ρ'_{nb}, instead of requiring all of the relationships among similar bands measured in the two sensors. The simpler approach described here is advantageous if a product algorithm requires a large number of bands.

One drawback to the present approach is that the accuracy of the derived relationship could depend on the accuracy of the model of the relationship between ρ'_{na} and ρ'_{nb}. This relationship is expressed by a polynomial in ρ'_{na}, and it is subsequently necessary to solve for ρ'_{nb}. In this study, this relationship was modeled using a first-order polynomial to minimize complexity during the derivation. The use of higher-order polynomials or more suitable functional forms could improve the accuracy of the inter-sensor VI relationship; however, such steps would require additional approximations at some point during the derivation. From a practical perspective, the accompanying

loss in model simplicity reduced the practicality of the model. Therefore, there is a trade-off between the practicality and the accuracy in modeling a relationship between ρ'_{na} and ρ'_{nb}. The choice of relationship must be optimized for ρ'_n, which would require a significant effort beyond the scope of the present discussion. This matter is worth investigating in a separate study.

This study focused on the influence of soil spectrum as a source of data variation. The derived VI relationships could also be influenced by biophysical parameters. This issue should be investigated thoroughly in a future study.

4.9 Conclusions

This study introduced an analytical technique for relating the VIs measured by two sensors. The relationship was derived using the soil isoline equation, which consisted of a set of reflectance spectra obtained under a constant soil spectrum. First, the relationship between the VIs measured by two sensors was explained conceptually. The conceptual relationship was applied to several realistic cases by truncating the order of the polynomials used to describe the soil isoline equations. Finally, the derived relationships were numerically examined using common radiative transfer models. The results validated the derived expressions and the applicability of the truncations. The derived VI relationships and the numerical results also indicated an important fact, that the inter-sensor relationship among the measured VIs could be influenced by the soil reflectance spectrum. Although this implication could be obtained from numerical simulations, the derivations introduced in this study confirmed this fact analytically.

Further studies are needed to improve the accuracy of the cross-calibration step based on the derived relationships. Such efforts should be devoted mainly to improving the accuracy of the relationships between ρ'_{na} and ρ'_{nb}. Such improvements may also be made by noting the trade-off between accuracy improvements and the practical utility of the derived VI relationship form. This investigation is left to future studies.

CHAPTER V

Conclusions

Differences among the wavelength band specifications for distinct sensors introduce systematic differences into the values of the spectral vegetation indices (VIs). These relative errors must be minimized algorithmically after data acquisition based on the relationships among the measurements. This study introduced a technique for deriving the relationship between VIs obtained from two sensors. The derivation proceeded using a parametric form of the soil isoline equations, which relate the reflectances measured at two different wavelengths.

This study derived a parametric form of the soil isoline equation, in which an index was used as a common parameter in Chapter 2. Note that the soil isoline equations assumed regularized spatial conditions of full canopy coverage. Numerical difficulties associated with singularities in the original subspace were overcame by rotating the red and NIR axes through an angle equal to the soil line slope. Although the derived form included an index-like parameter ρ'_n, a polynomial of arbitrary order could be used to represent the soil isoline equation. The derived parametric form suffered from the drawback that the soil isoline equation implicitly (rather than explicitly) described the relationship between the red and NIR reflectances.

The proposed isoline equations were compared with those derived using a theoretical framework for validation purposes. The findings from a comparison between the proposed and theoretically derived results could be summarized as follows: 1) The soil isoline equation with a polynomial fit was functionally equivalent to the isoline derived from a radiative transfer model. 2) The previously derived isoline was more numerically stable and, hence, more suitable than the isoline derived from an RT model.

Chapter 3 extended this study of the soil isoline equations in the red–NIR subspace by deriving an isoline expression under conditions of full canopy coverage. The parameter FVC was considered by employing the two-endmember LMM. Because

the model used the FVC parameter explicitly in its formulation, we were able to derive the parametric form of the soil isoline equations using the FVC. The derivations proceeded carefully by noting the differences between the fully covered case and the partially covered case in the definitions of the isoline coefficients. I found that the FVC parameter contributed to the coefficients of the second- and higher-order terms for both the red and NIR bands, indicating that the FVC parameter only influenced the higher-order terms.

These findings influenced the derivation of the five approximated cases defined over a range of truncation orders in the red and NIR reflectances. The validity of the derived expression was investigated by conducting a series of numerical experiments using PROSAIL. The numerical results revealed that the errors in the approximated isolines decreased as the truncation order increased. These results clearly indicated that the isoline equations could be improved by accounting for the FVC parameter explicitly.

This study introduced an analytical technique for relating the VIs measured by two sensors in Chapter 4. The relationship was derived using the soil isoline equation, which consisted of a set of reflectance spectra obtained under a constant soil spectrum. First, the relationship between the VIs measured by two sensors was explained conceptually. The conceptual relationship was applied to several realistic cases by truncating the order of the polynomials used to describe the soil isoline equations. Finally, the derived relationships were numerically examined using the radiative transfer models. The results validated the derived expressions and the applicability of the truncations. The derived VI relationships and the numerical results also indicated an important fact, that the inter-sensor relationships among the measured VIs could be influenced by the soil reflectance spectrum. Although this result could be obtained from the numerical simulations, the derivations introduced in this study confirmed this fact analytically.

Finally, I concluded that the soil isoline concept provided an effective tool for analyzing the wavelength effect in VIs. Two types of soil isolines must be further investigated to improve our understanding of the inter-VI relationship results, namely: (1) soil isoline equations in red-NIR space, and (2) inter-ρ'_n relationships (the equation specific to a pair of sensors). Further efforts must be examined to demonstrate the utility of these isoline models in analyzing satellite imagery and improving the accuracy of the cross-calibration step, although such improvements may also be made by noting the trade-off between accuracy improvements and the practical utility of the derived VI relationship form.

APPENDICES

APPENDIX A

Analysis of the Soil Isolines in the Wavelength Range 400-2500nm

A.1 Soil Isolines in the Wavelength Range 400-2500nm

Section 2.7 validated the soil isoline results derived from the red and NIR reflectance subspace through a comparison with the expression obtained using additive methods. A displacement analysis was used to investigate the limitations on the proposed derivation for reflectance subspaces other than the red and NIR wavelength pair. Note that if the proposed rotation steps were effective in avoiding singularities in cases other than the red-NIR case, soil isolines across a broad range of spectral domains could simultaneously be derived using a single algorithm.

Assume that the soil isolines/trajectories in a reflectance subspace are constructed from measurements at two different wavelengths ($\lambda_1, \lambda_2 \in [400-2500nm]$) corresponding to the soil brightness and leaf area index (LAI). Regardless of the wavelength pair, all soil isolines move from a baseline, called the soil line. The soil line equation describes the relationship between the soil reflectances,

$$R_{s\lambda_2} = a(\lambda_1, \lambda_2) R_{s\lambda_1} + b(\lambda_1, \lambda_2), \tag{A.1}$$

where $a(\lambda_1, \lambda_2)$ and $b(\lambda_1, \lambda_2)$ are the slope and offset of the soil line in a subspace constructed from two reflectances at λ_1 and λ_2, and $R_{s\lambda}$ is the soil reflectance spectrum at a wavelength λ, respectively.

The top-of canopy reflectance (TOC) vector $\boldsymbol{\rho}$ in the λ_1-λ_2 subspace is defined as

$$\boldsymbol{\rho} = (\rho_{\lambda_1}, \rho_{\lambda_2})^t, \tag{A.2}$$

where $\rho_{s\lambda}$ is the TOC reflectance spectrum at a wavelength of λ. The methods proposed in this study used an affine transformation of the reflectance subspace along the soil line,

$$\begin{aligned} \boldsymbol{\rho}' &= (\rho'_{\lambda_1}, \rho'_{\lambda_2})^t && \text{(A.3)} \\ &= T(\theta)(\boldsymbol{\rho} - \boldsymbol{\mu}), && \text{(A.4)} \end{aligned}$$

where $\boldsymbol{\rho}$ is the reflectance vector after the transformation, $T(\theta)$ is a rotation matrix through the angle corresponding to the soil line slope, and $\boldsymbol{\mu}$ is a vector corresponding to the soil line offset. θ and $\boldsymbol{\mu}$ are defined as

$$\begin{aligned} \theta &= \arctan(a(\lambda_1, \lambda_2)), && \text{(A.5)} \\ \boldsymbol{\mu} &= (0, b(\lambda_1, \lambda_2))^t. && \text{(A.6)} \end{aligned}$$

A.2 Displacement Vectors of the Soil Isolines

A displacement vector analysis of the soil isolines improved our understanding of the behavior of the soil isolines over a wide range of spectral domains, from 400 to 2500 nm. Here, the PROSAIL of numerical models was used to simulate the TOC reflectance spectra. The reflectance spectra in this numerical study were expressed as functions of the soil brightness and the LAI. The other input parameters were fixed as described in Chapter 3. Six LAI levels were prepared from five sets, from 0.5 to 3.7 in 0.8 intervals and assuming zero LAI (no canopy case). The soil brightness level was determined by the psoil index, which was set to 0, 0.5 or 1.0.

Three steps were used to obtain the displacement vectors for the soil isolines in the numerical experiments.

1. Choose reflectance spectrum $\boldsymbol{\rho}$ in the subspace between $\lambda_1 = x$ and $\lambda_2 = y$ in the 400−2500[nm] range, and in 50 nm intervals.

2. Retrieve the soil line coefficients (slope and offset) and transform $\boldsymbol{\rho}$ into $\boldsymbol{\rho}'$ using Eq. (A.4).

3. Calculate the displacement vectors δ' as follows,

$$\boldsymbol{\delta}'(\text{psoil}(i), \text{LAI}(j)) = \boldsymbol{\rho}'(\text{psoil}(i), \text{LAI}(j+1)) - \boldsymbol{\rho}'(\text{psoil}(i), \text{LAI}(j)), \qquad \text{(A.7)}$$

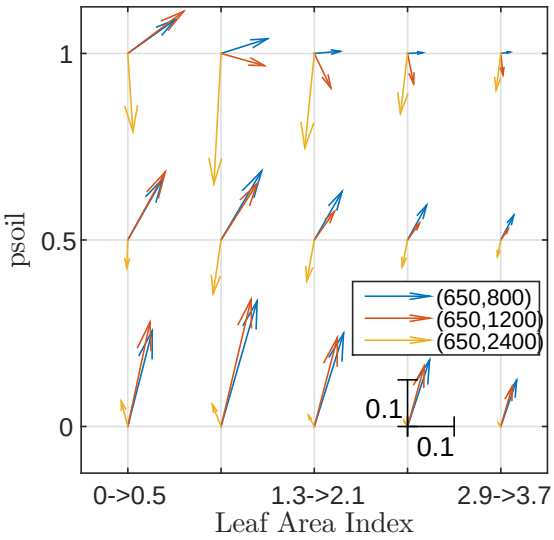

Figure A.1: Illustration of the displacement vectors δ' of the soil isolines for each psoil and LAI. The Y-axis of the vector field corresponds to the soil line slope.

where psoil(i) and LAI(j) are the psoil and LAI corresponding to the i- and j-th levels, respectively.

Figure A.1 presents the displacement vectors δ' of the soil isolines in three types of subspace for each psoil and LAI level. The Y-axis of the vector field corresponds to the soil line slope. In other words, the parallel direction is shown for the case of a vector directed along the Y-axis. Here, the X-axis is orthogonal to the soil line.

The blue and red colors in the figure indicate distinct directions in increments of the LAI level. The yellow directions at psoil = 1.0 are, regardless of the LAI value, accounted for by the Y-axis element.

A.3 Results

The angle of the displacement vectors is a key factor for understanding the trends in the soil isolines of various subspaces. Note that the trend in the direction along the soil line (Y-axis in Fig. A.1) produced singularities. The overall displacement vector (between zero LAI and 3.7 LAI) permitted detection of the conditions suspected of producing a singularity, as in the yellow case shown in Fig. A.1. The overall displacement vectors $\mathbf{\Delta}' = (\Delta x, \Delta y)$ were calculated simply by adding each element of the LAI. Note that this experiment included three soil brightness levels in the psoil (psoil = $(0, 0.5, 1)$). Furthermore, the angles corresponding to the three soil brightness

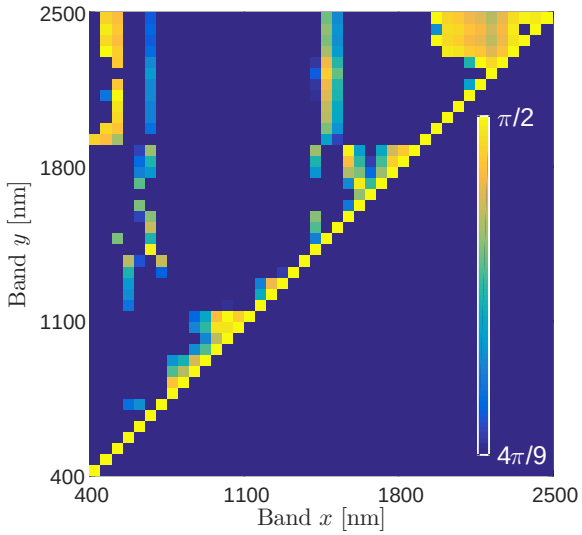

Figure A.2: Color plots of the maximum angle $\Theta_{\text{disp.}}(\lambda_1 = x, \lambda_2 = y)$ between the displacement vectors Δ and the soil line, in radians.

levels at each soil isoline, $\theta_{\text{disp.}}(\text{psoil})$ were obtained using the overall displacement vectors.

$$\theta_{\text{disp.}}(\text{psoil}) = \arctan\left(\frac{\Delta y}{\Delta x}\right) \tag{A.8}$$

The closer the angle was to 90 degrees, the more parallel the soil isoline were in the soil line, which promoted singularity formation. This investigation examined the conditions that contributed to singularity formation; therefore, the maximum angle value was adopted.

$$\Theta_{\text{disp.}}(\lambda_1, \lambda_2) = \max \theta_{\text{disp.}}(\text{psoil}) \tag{A.9}$$

The maximum angle of the displacement vectors $\Theta_{\text{disp.}}(\lambda_1, \lambda_2)$ at each wavelength pair $(\lambda_1 = x, \lambda_2 = y)$ is shown in Fig. A.2. The figure is colored from $4\pi/9$ to $\pi/2$. The spectral domains in yellow indicate the conditions suspected of yielding singularities as a result of transformation to the reflectance subspace.

Caution is needed to derive the soil isoline equations at some wavelengths. Further numerical experiments must be explored for better understanding of the conditions that contribute to the measured spectral responses. The SRFs effect must also be considered for any analysis of actual multispectral data.

BIBLIOGRAPHY

BIBLIOGRAPHY

[1] R. K. Pachauri, M. Allen, V. Barros, J. Broome, W. Cramer, R. Christ, J. Church, L. Clarke, Q. Dahe, P. Dasgupta *et al.*, "Climate Change 2014: Synthesis Report. Contribution of Working Groups I, II and III to the Fifth Assessment Report of the Intergovernmental Panel on Climate Change," 2014.

[2] C. B. Field, V. R. Barros, K. Mach, and M. Mastrandrea, *Climate change 2014: impacts, adaptation, and vulnerability*. Cambridge University Press Cambridge, New York, NY, 2014, vol. 1.

[3] L. Miles and V. Kapos, "Reducing greenhouse gas emissions from deforestation and forest degradation: Global land-use implications," *Science*, vol. 320, no. 5882, pp. 1454–1455, 2008.

[4] M. A. Wulder, J. C. White, S. N. Goward, J. G. Masek, J. R. Irons, M. Herold, W. B. Cohen, T. R. Loveland, and C. E. Woodcock, "Landsat continuity: Issues and opportunities for land cover monitoring," *Remote Sens. Environ.*, vol. 112, no. 3, pp. 955–969, 2008.

[5] R. E. Kennedy, Z. Yang, and W. B. Cohen, "Detecting trends in forest disturbance and recovery using yearly Landsat time series: 1. LandTrendr - Temporal segmentation algorithms," *Remote Sens. Environ.*, vol. 114, no. 12, pp. 2897–2910, 2010.

[6] G. Gutman and A. Ignatov, "The derivation of the green vegetation fraction from NOAA/AVHRR data for use in numerical weather prediction models," *Int. J. Remote Sens.*, vol. 19, no. 8, pp. 1533–1543, 1998.

[7] X. Xiao, Z. Shen, and X. Qin, "Assessing the potential of VEGETATION sensor data for mapping snow and ice cover: a Normalized Difference Snow and Ice Index," *Int. J. Remote Sens.*, vol. 22, no. 13, pp. 2479–2487, 2001.

[8] J. Sobrino, M. Gómez, J. Jiménez-Muñoz, and A. Olioso, "Application of a simple algorithm to estimate daily evapotranspiration from NOAA–AVHRR images for the Iberian Peninsula," *Remote Sens. Environ.*, vol. 110, no. 2, pp. 139–148, 2007.

[9] C. O. Justice, E. Vermote, J. R. Townshend, R. Defries, D. P. Roy, D. K. Hall, V. V. Salomonson, J. L. Privette, G. Riggs, A. Strahler *et al.*, "The Moderate Resolution Imaging Spectroradiometer (MODIS): Land remote sensing for

global change research," *IEEE Trans. Geosci. Remote Sens.*, vol. 36, no. 4, pp. 1228–1249, 1998.

[10] L. Giglio, J. Randerson, G. Van der Werf, P. Kasibhatla, G. Collatz, D. Morton, and R. DeFries, "Assessing variability and long-term trends in burned area by merging multiple satellite fire products," *Biogeosciences*, vol. 7, no. 3, 2010.

[11] P. D. Kessler, B. D. Killough, S. Gowda, B. R. Williams, G. Chander, and M. Qu, "CEOS visualization environment (COVE) tool for intercalibration of satellite instruments," *IEEE Trans. Geosci. Remote Sens.*, vol. 51, no. 3, pp. 1081–1087, 2013.

[12] C. Atzberger, M. Wess, M. Doneus, and G. Verhoeven, "ARCTIS - A MATLAB® toolbox for archaeological imaging spectroscopy," *Remote Sens.*, vol. 6, no. 9, pp. 8617–8638, 2014.

[13] S. P. Neeck, T. J. Magner, and G. E. Paules, "NASA's small satellite missions for Earth observation," *Acta Astronautica*, vol. 56, no. 1, pp. 187–192, 2005.

[14] A. K. Whitcraft, I. Becker-Reshef, B. D. Killough, and C. O. Justice, "Meeting earth observation requirements for global agricultural monitoring: An evaluation of the revisit capabilities of current and planned moderate resolution optical earth observing missions," *Remote Sens.*, vol. 7, no. 2, pp. 1482–1503, 2015.

[15] A. S. Belward and J. O. Skøien, "Who launched what, when and why; trends in global land-cover observation capacity from civilian earth observation satellites," *ISPRS Journal of Photogrammetry and Remote Sensing*, vol. 103, pp. 115–128, 2015.

[16] G. Chander, T. J. Hewison, N. Fox, X. Wu, X. Xiong, and W. J. Blackwell, "Overview of intercalibration of satellite instruments," *IEEE Trans. Geosci. Remote Sens.*, pp. 1056–1080, 2013.

[17] G. Asrar *et al.*, *Theory and applications of optical remote sensing.* John Wiley & Sons, 1989.

[18] M. O. Smith, P. E. Johnson, and J. B. Adams, "Quantitative determination of mineral types and abundances from reflectance spectra using principal components analysis," *Journal of Geophysical Research: Solid Earth*, vol. 90, no. S02, 1985.

[19] G. P. Asner, "Biophysical and biochemical sources of variability in canopy reflectance," *Remote Sens. Environ.*, vol. 64, no. 3, pp. 234–253, 1998.

[20] R. J. Kauth and G. Thomas, "The tasselled cap–a graphic description of the spectral-temporal development of agricultural crops as seen by Landsat," in *LARS Symposia*, 1976, p. 159.

[21] Y. M. Govaerts, M. M. Verstraete, B. Pinty, and N. Gobron, "Designing optimal spectral indices: A feasibility and proof of concept study," *Int. J. Remote Sens.*, vol. 20, no. 9, pp. 1853–1873, 1999.

[22] J.-P. Gastellu-Etchegorry, V. Demarez, V. Pinel, and F. Zagolski, "Modeling radiative transfer in heterogeneous 3-D vegetation canopies," *Remote Sens. Environ.*, vol. 58, no. 2, pp. 131–156, 1996.

[23] E. F. Vermote, D. Tanré, J.-L. Deuze, M. Herman, and J.-J. Morcette, "Second simulation of the satellite signal in the solar spectrum, 6S: An overview," *IEEE Trans. Geosci. Remote Sens.*, vol. 35, no. 3, pp. 675–686, 1997.

[24] H. Kobayashi and H. Iwabuchi, "A coupled 1-D atmosphere and 3-D canopy radiative transfer model for canopy reflectance, light environment, and photosynthesis simulation in a heterogeneous landscape," *Remote Sens. Environ.*, vol. 112, no. 1, pp. 173–185, 2008.

[25] C. F. Jordan, "Derivation of leaf-area index from quality of light on the forest floor," *Ecology*, pp. 663–666, 1969.

[26] J. Rouse, R. Haas, J. Schell, and D. Deering, "Third ERTS symposium," *NASA SP-351*, vol. 1, pp. 309–317, 1973.

[27] A. J. Richardson and C. Weigand, "Distinguishing vegetation from soil background information," *Photogramm. Eng. Remote Sens.*, vol. 43, no. 12, 1977.

[28] J. Clevers, "The derivation of a simplified reflectance model for the estimation of leaf area index," *Remote Sens. Environ.*, vol. 25, no. 1, pp. 53–69, 1988.

[29] A. R. Huete, "A soil-adjusted vegetation index (SAVI)," *Remote Sens. Environ.*, vol. 25, no. 3, pp. 295–309, 1988.

[30] A. J. Richardson and J. H. Everitt, "Using spectral vegetation indices to estimate rangeland productivity," *Geocarto International*, vol. 7, no. 1, pp. 63–69, 1992.

[31] J. Qi, A. Chehbouni, A. Huete, Y. Kerr, and S. Sorooshian, "A modified soil adjusted vegetation index," *Remote Sens. Environ.*, vol. 48, no. 2, pp. 119–126, 1994.

[32] G. Rondeaux, M. Steven, and F. Baret, "Optimization of soil-adjusted vegetation indices," *Remote Sens. Environ.*, vol. 55, no. 2, pp. 95–107, 1996.

[33] M. Gilabert, J. González-Piqueras, F. Garcıa-Haro, and J. Meliá, "A generalized soil-adjusted vegetation index," *Remote Sens. Environ.*, vol. 82, no. 2, pp. 303–310, 2002.

[34] A. Huete, K. Didan, T. Miura, E. P. Rodriguez, X. Gao, and L. G. Ferreira, "Overview of the radiometric and biophysical performance of the MODIS vegetation indices," *Remote Sens. Environ.*, vol. 83, no. 1, pp. 195–213, 2002.

[35] Z. Jiang, A. R. Huete, K. Didan, and T. Miura, "Development of a two-band enhanced vegetation index without a blue band," *Remote Sens. Environ.*, vol. 112, no. 10, pp. 3833–3845, 2008.

[36] A. R. Huete, K. F. Huemmrich, T. Miura, X. Xiao, K. Didan, W. van Leeuwen, F. Hall, and C. J. Tucker, "Vegetation index greenness global data set," *NASA ESDR/CDR*, 2006.

[37] R. B. Myneni and F. G. Hall, "The interpretation of spectral vegetation indexes," *IEEE Trans. Geosci. Remote Sens.*, vol. 33, no. 2, pp. 481–486, 1995.

[38] Z. Jiang, A. R. Huete, J. Chen, Y. Chen, J. Li, G. Yan, and X. Zhang, "Analysis of NDVI and scaled difference vegetation index retrievals of vegetation fraction," *Remote Sens. Environ.*, vol. 101, no. 3, pp. 366–378, 2006.

[39] G. Asrar, M. Fuchs, E. Kanemasu, and J. Hatfield, "Estimating absorbed photosynthetic radiation and leaf area index from spectral reflectance in wheat," *Agronomy Journal*, vol. 76, no. 2, pp. 300–306, 1984.

[40] H. Yoshioka, T. Miura, J. A. Demattê, K. Batchily, and A. R. Huete, "Derivation of soil line influence on two-band vegetation indices and vegetation isolines," *Remote Sens.*, vol. 1, no. 4, pp. 842–857, 2009.

[41] Y. J. Kaufman and D. Tanre, "Atmospherically resistant vegetation index (ARVI) for EOS-MODIS," *IEEE Trans. Geosci. Remote Sens.*, vol. 30, no. 2, pp. 261–270, 1992.

[42] A. Karnieli, Y. J. Kaufman, L. Remer, and A. Wald, "AFRI - Aerosol free vegetation index," *Remote Sens. Environ.*, vol. 77, no. 1, pp. 10–21, 2001.

[43] H. Kobayashi and D. G. Dye, "Atmospheric conditions for monitoring the long-term vegetation dynamics in the amazon using normalized difference vegetation index," *Remote Sens. Environ.*, vol. 97, no. 4, pp. 519–525, 2005.

[44] L. Montandon and E. Small, "The impact of soil reflectance on the quantification of the green vegetation fraction from NDVI," *Remote Sens. Environ.*, vol. 112, no. 4, pp. 1835–1845, 2008.

[45] K. Obata and H. Yoshioka, "Inter-algorithm relationships for the estimation of the fraction of vegetation cover based on a two endmember linear mixture model with the vi constraint," *Remote Sens.*, vol. 2, no. 7, pp. 1680–1701, 2010.

[46] C. S. Potter, J. T. Randerson, C. B. Field, P. A. Matson, P. M. Vitousek, H. A. Mooney, and S. A. Klooster, "Terrestrial ecosystem production: A process

model based on global satellite and surface data," *Global Biogeochem. Cycles*, vol. 7, no. 4, pp. 811–841, 1993.

[47] A. P. Trishchenko, J. Cihlar, and Z. Li, "Effects of spectral response function on surface reflectance and NDVI measured with moderate resolution satellite sensors," *Remote Sens. Environ.*, vol. 81, no. 1, pp. 1–18, 2002.

[48] K. Thorne, B. Markharn, P. S. Barker, and S. Biggar, "Radiometric calibration of Landsat," *Photogramm. Eng. Remote Sens.*, vol. 63, no. 7, pp. 853–858, 1997.

[49] G. Chander, N. Mishra, D. L. Helder, D. B. Aaron, A. Angal, T. Choi, X. Xiong, and D. R. Doelling, "Applications of spectral band adjustment factors (SBAF) for cross-calibration," *IEEE Trans. Geosci. Remote Sens.*, vol. 51, no. 3, pp. 1267–1281, 2013.

[50] T. Miura, A. Huete, and H. Yoshioka, "An empirical investigation of cross-sensor relationships of NDVI and red/near-infrared reflectance using EO-1 Hyperion data," *Remote Sens. Environ.*, vol. 100, no. 2, pp. 223–236, 2006.

[51] P. Teillet, J. Barker, B. Markham, R. Irish, G. Fedosejevs, and J. Storey, "Radiometric cross-calibration of the Landsat-7 ETM+ and Landsat-5 TM sensors based on tandem data sets," *Remote Sens. Environ.*, vol. 78, no. 1, pp. 39–54, 2001.

[52] P. Teillet, G. Fedosejevs, K. Thome, and J. L. Barker, "Impacts of spectral band difference effects on radiometric cross-calibration between satellite sensors in the solar-reflective spectral domain," *Remote Sens. Environ.*, vol. 110, no. 3, pp. 393–409, 2007.

[53] A. Gonsamo and J. M. Chen, "Spectral response function comparability among 21 satellite sensors for vegetation monitoring," *IEEE Trans. Geosci. Remote Sens.*, vol. 51, no. 3, pp. 1319–1335, 2013.

[54] J. C. Price, "Combining multispectral data of differing spatial resolution," *IEEE Trans. Geosci. Remote Sens.*, vol. 37, no. 3, pp. 1199–1203, 1999.

[55] E. Tarnavsky, S. Garrigues, and M. E. Brown, "Multiscale geostatistical analysis of AVHRR, SPOT-VGT, and MODIS global NDVI products," *Remote Sens. Environ.*, vol. 112, no. 2, pp. 535–549, 2008.

[56] K. Obata and A. R. Huete, "Scaling effects on area-averaged fraction of vegetation cover derived using a linear mixture model with two-band spectral vegetation index constraints," *J. App. Remote Sens.*, vol. 8, no. 1, pp. 083 629–083 629, 2014.

[57] R. Fensholt, I. Sandholt, S. Stisen, and C. Tucker, "Analysing NDVI for the African continent using the geostationary meteosat second generation SEVIRI sensor," *Remote Sens. Environ.*, vol. 101, no. 2, pp. 212–229, 2006.

[58] A. Pocewicz, L. A. Vierling, L. B. Lentile, and R. Smith, "View angle effects on relationships between MISR vegetation indices and leaf area index in a recently burned ponderosa pine forest," *Remote Sens. Environ.*, vol. 107, no. 1, pp. 322–333, 2007.

[59] K. J. Thome, D. L. Helder, D. Aaron, and J. D. Dewald, "Landsat-5 TM and Landsat-7 ETM+ absolute radiometric calibration using the reflectance-based method," *IEEE Trans. Geosci. Remote Sens.*, vol. 42, no. 12, pp. 2777–2785, 2004.

[60] T. Miura, A. R. Huete, H. Yoshioka, and B. N. Holben, "An error and sensitivity analysis of atmospheric resistant vegetation indices derived from dark target-based atmospheric correction," *Remote Sens. Environ.*, vol. 78, no. 3, pp. 284–298, 2001.

[61] E. P. Crist and R. C. Cicone, "A physically-based transformation of thematic mapper data—the TM tasseled cap," *IEEE Trans. Geosci. Remote Sens.*, no. 3, pp. 256–263, 1984.

[62] M. E. Brown, D. J. Lary, A. Vrieling, D. Stathakis, and H. Mussa, "Neural networks as a tool for constructing continuous NDVI time series from AVHRR and MODIS," *Int. J. Remote Sens.*, vol. 29, no. 24, pp. 7141–7158, 2008.

[63] A. A. Gitelson and Y. J. Kaufman, "MODIS NDVI optimization to fit the AVHRR data series–spectral considerations," *Remote Sens. Environ.*, vol. 66, no. 3, pp. 343–350, 1998.

[64] J. Hill and D. Aifadopoulou, "Comparative analysis of Landsat-5 TM and SPOT HRV-1 data for use in multiple sensor approaches," *Remote Sens. Environ.*, vol. 34, no. 1, pp. 55–70, 1990.

[65] K. J. Thome, S. F. Biggar, and W. Wisniewski, "Cross comparison of EO-1 sensors and other earth resources sensors to Landsat-7 ETM+ using railroad valley playa," *IEEE Trans. Geosci. Remote Sens.*, vol. 41, no. 6, pp. 1180–1188, 2003.

[66] T. Miura, H. Yoshioka, K. Fujiwara, and H. Yamamoto, "Inter-comparison of ASTER and MODIS surface reflectance and vegetation index products for synergistic applications to natural resource monitoring," *Sensors*, vol. 8, no. 4, pp. 2480–2499, 2008.

[67] J. Cihlar, R. Latifovic, J. Chen, A. Trishchenko, Y. Du, G. Fedosejevs, and B. Guindon, "Systematic corrections of AVHRR image composites for temporal studies," *Remote Sens. Environ.*, vol. 89, no. 2, pp. 217–233, 2004.

[68] C. Atzberger, A. Klisch, M. Mattiuzzi, and F. Vuolo, "Phenological metrics derived over the european continent from NDVI3G data and MODIS time series," *Remote Sens.*, vol. 6, no. 1, pp. 257–284, 2013.

[69] A. P. Trishchenko, "Effects of spectral response function on surface reflectance and NDVI measured with moderate resolution satellite sensors: Extension to AVHRR NOAA-17, 18 and METOP-A," *Remote Sens. Environ.*, vol. 113, no. 2, pp. 335–341, 2009.

[70] M. D. Steven, T. J. Malthus, F. Baret, H. Xu, and M. J. Chopping, "Intercalibration of vegetation indices from different sensor systems," *Remote Sens. Environ.*, vol. 88, no. 4, pp. 412–422, 2003.

[71] C. J. Tucker, J. E. Pinzon, M. E. Brown, D. A. Slayback, E. W. Pak, R. Mahoney, E. F. Vermote, and N. El Saleous, "An extended AVHRR 8-km NDVI dataset compatible with MODIS and SPOT vegetation NDVI data," *Int. J. Remote Sens.*, vol. 26, no. 20, pp. 4485–4498, 2005.

[72] K. Günther and S. Maier, "AVHRR compatible vegetation index derived from MERIS data," *Int. J. Remote Sens.*, vol. 28, no. 3-4, pp. 693–708, 2007.

[73] E. Swinnen and F. Veroustraete, "Extending the SPOT-VEGETATION NDVI time series (1998–2006) back in time with NOAA-AVHRR data (1985–1998) for southern Africa," *IEEE Trans. Geosci. Remote Sens.*, vol. 46, no. 2, pp. 558–572, 2008.

[74] Y. Kim, T. Miura, Z. Jiang, and A. R. Huete, "Spectral compatibility of vegetation indices across sensors: band decomposition analysis with Hyperion data," *J. App. Remote Sens.*, vol. 4, no. 1, pp. 043 520–043 520, 2010.

[75] T. Miura, J. P. Turner, and A. R. Huete, "Spectral compatibility of the NDVI across VIIRS, MODIS, and AVHRR: An analysis of atmospheric effects using EO-1 Hyperion," *IEEE Trans. Geosci. Remote Sens.*, vol. 51, no. 3, pp. 1349–1359, 2013.

[76] C. J. Tucker, "Red and photographic infrared linear combinations for monitoring vegetation," *Remote Sens. Environ.*, vol. 8, no. 2, pp. 127–150, 1979.

[77] K. Gallo and C. Daughtry, "Differences in vegetation indices for simulated Landsat-5 MSS and TM, NOAA-9 AVHRR, and SPOT-1 sensor systems," *Remote Sens. Environ.*, vol. 23, no. 3, pp. 439–452, 1987.

[78] W. J. van Leeuwen, B. J. Orr, S. E. Marsh, and S. M. Herrmann, "Multi-sensor NDVI data continuity: Uncertainties and implications for vegetation monitoring applications," *Remote Sens. Environ.*, vol. 100, no. 1, pp. 67–81, 2006.

[79] H. E. Beck, T. R. McVicar, A. I. van Dijk, J. Schellekens, R. A. de Jeu, and L. A. Bruijnzeel, "Global evaluation of four AVHRR–NDVI data sets: Intercomparison and assessment against Landsat imagery," *Remote Sens. Environ.*, vol. 115, no. 10, pp. 2547–2563, 2011.

[80] A. Tong and Y. He, "Comparative analysis of SPOT, Landsat, MODIS, and AVHRR normalized difference vegetation index data on the estimation of leaf area index in a mixed grassland ecosystem," *J. App. Remote Sens.*, vol. 7, no. 1, pp. 073 599–073 599, 2013.

[81] M. M. Verstraete and B. Pinty, "Designing optimal spectral indexes for remote sensing applications," *IEEE Trans. Geosci. Remote Sens.*, vol. 34, no. 5, pp. 1254–1265, 1996.

[82] H. Yoshioka, A. R. Huete, and T. Miura, "Derivation of vegetation isoline equations in red-NIR reflectance space," *IEEE Trans. Geosci. Remote Sens.*, vol. 38, no. 2, pp. 838–848, 2000.

[83] A. Kallel, S. Le Hégarat-Mascle, C. Ottlé, and L. Hubert-Moy, "Determination of vegetation cover fraction by inversion of a four-parameter model based on isoline parametrization," *Remote Sens. Environ.*, vol. 111, no. 4, pp. 553–566, 2007.

[84] H. Yoshioka, T. Miura, and A. R. Huete, "An isoline-based translation technique of spectral vegetation index using EO-1 Hyperion data," *IEEE Trans. Geosci. Remote Sens.*, vol. 41, no. 6, pp. 1363–1372, 2003.

[85] K. Obata, T. Miura, H. Yoshioka, and A. R. Huete, "Derivation of a MODIS-compatible enhanced vegetation index from visible infrared imaging radiometer suite spectral reflectances using vegetation isoline equations," *J. App. Remote Sens.*, vol. 7, no. 1, pp. 073 467–073 467, 2013.

[86] N. V. Shabanov, L. Zhou, Y. Knyazikhin, R. B. Myneni, and C. J. Tucker, "Analysis of interannual changes in northern vegetation activity observed in AVHRR data from 1981 to 1994," *IEEE Trans. Geosci. Remote Sens.*, vol. 40, no. 1, pp. 115–130, 2002.

[87] C. Atzberger and K. Richter, "Spatially constrained inversion of radiative transfer models for improved LAI mapping from future Sentinel-2 imagery," *Remote Sens. Environ.*, vol. 120, pp. 208–218, 2012.

[88] F. Baret and G. Guyot, "Potentials and limits of vegetation indices for lai and apar assessment," *Remote Sens. Environ.*, vol. 35, no. 2, pp. 161–173, 1991.

[89] J. C. Price and W. C. Bausch, "Leaf area index estimation from visible and near-infrared reflectance data," *Remote Sens. Environ.*, vol. 52, no. 1, pp. 55–65, 1995.

[90] M. M. Verstraete, B. Pinty, and R. B. Myneni, "Potential and limitations of information extraction on the terrestrial biosphere from satellite remote sensing," *Remote Sens. Environ.*, vol. 58, no. 2, pp. 201–214, 1996.

[91] A. Huete and R. Jackson, "Suitability of spectral indices for evaluating vegetation characteristics on arid rangelands," *Remote Sens. Environ.*, vol. 23, no. 2, pp. 213IN1–232IN8, 1987.

[92] F. Baret, G. Guyot, and D. Major, "TSAVI: a vegetation index which minimizes soil brightness effects on LAI and APAR estimation," in *Geoscience and Remote Sensing Symposium, 1989. IGARSS'89. 12th Canadian Symposium on Remote Sensing., 1989 International*, vol. 3. IEEE, 1989, pp. 1355–1358.

[93] F. Baret, S. Jacquemoud, and J. Hanocq, "The soil line concept in remote sensing," *Remote Sensing Reviews*, vol. 7, no. 1, pp. 65–82, 1993.

[94] H. Yoshioka, T. Miura, A. Huete, and B. Ganapol, "Analysis of vegetation isolines in red-NIR reflectance space," *Remote Sens. Environ.*, vol. 74, no. 2, pp. 313–326, 2000.

[95] Z. Jiang, J. Li, J. Qi, and A. R. Huete, "Interpretation of the modified soil-adjusted vegetation index isolines in red-NIR reflectance space," *J. App. Remote Sens.*, vol. 1, no. 1, pp. 013 503–013 503, 2007.

[96] W. Verhoef, "Light scattering by leaf layers with application to canopy reflectance modeling: the SAIL model," *Remote Sens. Environ.*, vol. 16, no. 2, pp. 125–141, 1984.

[97] S. Jacquemoud and F. Baret, "PROSPECT: A model of leaf optical properties spectra," *Remote Sens. Environ.*, vol. 34, no. 2, pp. 75–91, 1990.

[98] S. Jacquemoud, F. Baret, B. Andrieu, F. Danson, and K. Jaggard, "Extraction of vegetation biophysical parameters by inversion of the PROSPECT+ SAIL models on sugar beet canopy reflectance data. Application to TM and AVIRIS sensors," *Remote Sens. Environ.*, vol. 52, no. 3, pp. 163–172, 1995.

[99] S. Jacquemoud, W. Verhoef, F. Baret, C. Bacour, P. J. Zarco-Tejada, G. P. Asner, C. François, and S. L. Ustin, "PROSPECT+ SAIL models: A review of use for vegetation characterization," *Remote Sens. Environ.*, vol. 113, pp. S56–S66, 2009.

[100] R. D. Jackson and A. R. Huete, "Interpreting vegetation indices," *Prev. Vet. Med.*, vol. 11, pp. 185–200, 1991.

[101] A. Huete, R. Jackson, and D. Post, "Spectral response of a plant canopy with different soil backgrounds," *Remote Sens. Environ.*, vol. 17, no. 1, pp. 37–53, 1985.

[102] H. Yoshioka, H. Yamamoto, and T. Miura, "Use of an isoline-based inversion technique to retrieve a leaf area index for inter-sensor calibration of spectral vegetation index," in *Geoscience and Remote Sensing Symposium, 2002. IGARSS'02. 2002 IEEE International*, vol. 3. IEEE, 2002, pp. 1639–1641.

[103] H. Yoshioka, T. Miura, and K. Obata, "Derivation of relationships between spectral vegetation indices from multiple sensors based on vegetation isolines," *Remote Sens.*, vol. 4, no. 3, pp. 583–597, 2012.

[104] F. Liu, Q. Qin, C. Chen, H. Feng, N. Zhang, and L. Chai, "Designing an improved soil moisture index in the near-infrared and shortwave plane," in *Geoscience and Remote Sensing Symposium (IGARSS), 2011 IEEE International*. IEEE, 2011, pp. 3074–3077.

[105] N. V. Shabanov, D. Huang, W. Yang, B. Tan, Y. Knyazikhin, R. B. Myneni, D. E. Ahl, S. T. Gower, A. R. Huete, L. E. O. Aragão *et al.*, "Analysis and optimization of the MODIS leaf area index algorithm retrievals over broadleaf forests," *IEEE Trans. Geosci. Remote Sens.*, vol. 43, no. 8, pp. 1855–1865, 2005.

[106] C. Atzberger, K. Richter, F. Vuolo, R. Darvishzadeh, and M. Schlerf, "Why confining to vegetation indices? Exploiting the potential of improved spectral observations using radiative transfer models," in *SPIE Remote Sensing*. SPIE, 2011, pp. 81 740Q–81 740Q.

[107] H. Yoshioka and K. Obata, "Soil isoline equation in red-NIR reflectance space for cross calibration of NDVI between sensors," in *Geoscience and Remote Sensing Symposium (IGARSS), 2011 IEEE International*. IEEE, 2011, pp. 3082–3085.

[108] K. Taniguchi, Y. Ikuta, K. Obata, M. Matsuoka, and H. Yoshioka, "Parametric representation of soil isoline equation and its accuracy estimation in red-NIR reflectance space," in *SPIE Asia-Pacific Remote Sensing*. SPIE, 2012, pp. 85 241J–85 241J.

[109] K. Taniguchi, K. Obata, M. Matsuoka, and H. Yoshioka, "Translation accuracy based on inter-sensor VI relationship with higher-order soil isoline equation," in *ISRS*. ISRS, 2013, pp. 87–90.

[110] C. Atzberger and K. Richter, "Geostatistical regularization of inverse models for the retrieval of vegetation biophysical variables," in *SPIE Europe Remote Sensing*. SPIE, 2009, pp. 74 781O–74 781O.

[111] K. D. Cooper and J. A. Smith, "A monte carlo reflectance model for soil surfaces with three-dimensional structure," *IEEE Trans. Geosci. Remote Sens.*, no. 5, pp. 668–673, 1985.

[112] M. F. Jasinski and P. S. Eagleson, "The structure of red-infrared scattergrams of semivegetated landscapes," *IEEE Trans. Geosci. Remote Sens.*, vol. 27, no. 4, pp. 441–451, 1989.

[113] ——, "Estimation of subpixel vegetation cover using red-infrared scattergrams," *IEEE Trans. Geosci. Remote Sens.*, vol. 28, no. 2, pp. 253–267, 1990.

[114] T. N. Carlson, R. R. Gillies, and T. J. Schmugge, "An interpretation of methodologies for indirect measurement of soil water content," *Agricultural and forest meteorology*, vol. 77, no. 3, pp. 191–205, 1995.

[115] T. N. Carlson and D. A. Ripley, "On the relation between NDVI, fractional vegetation cover, and leaf area index," *Remote Sens. Environ.*, vol. 62, no. 3, pp. 241–252, 1997.

[116] K. Obata and H. Yoshioka, "Comparison of the noise robustness of FVC retrieval algorithms based on linear mixture models," *Remote Sens.*, vol. 3, no. 7, pp. 1344–1364, 2011.

[117] S. Jacquemoud, F. Baret, and J. Hanocq, "Modeling spectral and bidirectional soil reflectance," *Remote Sens. Environ.*, vol. 41, no. 2, pp. 123–132, 1992.

[118] J. C. Price, "On the information content of soil reflectance spectra," *Remote Sens. Environ.*, vol. 33, no. 2, pp. 113–121, 1990.

[119] K. Taniguchi, K. Obata, and H. Yoshioka, "Derivation and approximation of soil isoline equations in the red–near-infrared reflectance subspace," *J. App. Remote Sens.*, vol. 8, no. 1, pp. 083 621–083 621, 2014.

[120] ——, "Investigation of inter-sensor NDVI relationships based on analytical representation of soil isolines," in *Geoscience and Remote Sensing Symposium (IGARSS), 2012 IEEE International*. IEEE, 2012, pp. 4891–4894.

[121] K. Taniguchi, K. Obata, M. Matsuoka, and H. Yoshioka, "Inter-sensor relationship of two-band spectral vegetation index based on soil isoline equation: derivation and numerical validation," in *SPIE Optical Engineering+ Applications*. SPIE, 2013, pp. 88 690D–88 690D.

[122] J. Clevers, "Application of a weighted infrared-red vegetation index for estimating leaf area index by correcting for soil moisture," *Remote Sens. Environ.*, vol. 29, no. 1, pp. 25–37, 1989.

LIST OF PUBLICATIONS

Journals

1. K. Taniguchi, K. Obata and H. Yoshioka. "Derivation and approximation of soil isoline equations in the red-near-infrared reflectance subspace," *Journal of Applied Remote Sensing*, 8(1), 083621, June 2014. (Chapter 2)

2. K. Taniguchi, K. Obata and H. Yoshioka. "Soil isoline equations in the red-NIR reflectance subspace describe a heterogeneous canopy," *Journal of Applied Remote Sensing*, 10(1), 016013, Februrary 2016. (Chapter 3)

Proceedings(Peer reviewed)

1. K. Taniguchi, K. Obata, and H. Yoshioka. "Evaluation of bias reduction in cross-calibration of NDVI based on soil isoline equations: Comparison with error estimated from signal-to-noise ratio," *Geoscience and Remote Sensing Symposium 2015 IEEE International*, Milan, Italy, July 2015. (Chapter 4)

2. K. Taniguchi, K. Obata, M. Matsuoka and H. Yoshioka. "Inter-sensor relationship of two-band spectral vegetation index based on soil isoline equation: derivation and numerical validation," *SPIE Optics+Photonics2013*, 6 pages, San Diego, USA, August 2013. (Chapter 4)

3. K. Taniguchi, K. Obata, M. Matsuoka and H. Yoshioka. "Validity of soil isoline equation for a system of canopy and soil layers," *Geoscience and Remote Sensing Symposium 2013 IEEE International*, pp.2613-2616, Melbourne, Australia, July 2013. (Chapter 2)

4. K. Taniguchi, K. Obata, M. Matsuoka and H. Yoshioka. "Translation accuracy based on inter-sensor VI relationship with higher-order soil isoline equation," *International Symposium on Remote Sensing 2013*, pp. 87-90, Chiba, Japan, May 2013. (Chapter 4)

5. K. Taniguchi, Y. Ikuta, K. Obata, M. Matsuoka and H. Yoshioka. "Parametric representation of soil isoline equation and its accuracy estimation in red-NIR reflectance space," *Asia-Pacific Remote Sensing 2012 SPIE*, 6 pages, Kyoto, Japan, October-November 2012. (Chapter 2)

6. K. Taniguchi, K. Obata and H.Yoshioka. "Investigation of inter-sensor NDVI relationships based on analytical representation of soil isolines," *Geoscience and Remote Sensing Symposium 2012 IEEE International*, pp.4891-4894, Munich, Germany, July 2012. (Chapter 4)

Proceedings(Non-peer reviewed)

1. K. Taniguchi, K. Obata and H. Yoshioka. "Derivation of inter-sensor NDVI relationships based on soil isoline equations," *Proc. in G Space Expo Student Forum2012*, Kanagawa, Japan, June 2012.

2. K. Taniguchi, H. Yoshioka and K. Obata. "Intercalibration technique based on soil isolines for satellite constellation system: Potential in bias reduction," *40-th SICE Remote Sensing Symposium*, pp. 11-12, Tokyo, Japan, March 2015 (in Japanese with English abstract).

Awards

1. IEEE GRSS Japan Chapter Young Researcher Award (2015.03.02)

2. The 2014 Best Paper Award of Interdisciplinary Applications in *Journal of Applied Remote Sensing* (2015.08.24)